Low Noise Supercontinuum Lasers for Optical Coherence Tomography Systems

Engelsholm, Rasmus Dybbro

Publication date:
2018

Document Version
Publisher's PDF, also known as Version of record

DTU Fotonik
Department of Photonics Engineering

Low Noise Supercontinuum Lasers for Optical Coherence Tomography Systems

Rasmus Dybbro Engelsholm

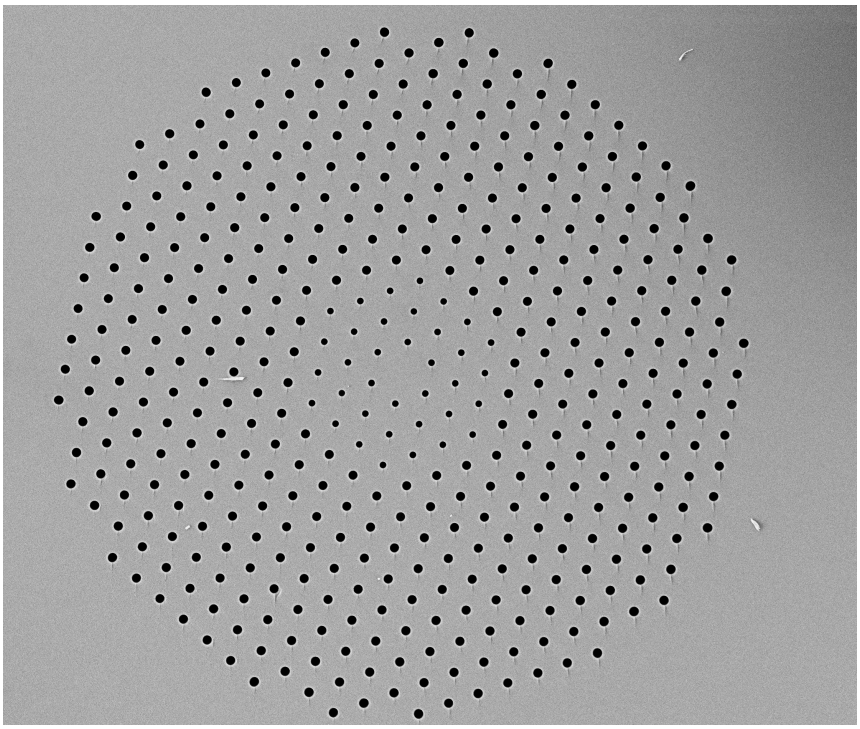

Supervisor: Ole Bang
Co-Supervisor: Christos Markos

Department of Photonics Engineering
Technical University of Denmark

31 October 2018

Abstract

Supercontinuum sources have wide ranging applications due to their exceptional brightness, spatial coherence and broad spectral coverage. Within the field of spectral domain optical coherence tomography they are especially interesting, as their spectral broadness enable imaging with sub-micrometer resolution. This can in turn be used for skin and eye disease diagnostics as well as non destructive quality testing of a large range of products. However, the high relative noise of supercontinuum sources decreases image quality in terms of higher background noise and lower contrast, compared to other, less broad, sources. A part of this thesis deals with ways to quantify the noise in relation to optical coherence tomography across measurement methods.

A section of this thesis is the step by step derivation of the generalized nonlinear Schrödinger equation, including tapering, multiple modes and mode profile dispersion. A numerical scheme for solving the equation was then implemented and tested. The numerical model was used to understand how undertapering can reduce supercontinuum relative intensity noise near the spectral edges. The model was also used to investigate low noise supercontinuum generation in all normal dispersion fibers. Both Raman scattering and polarization modulation instability was shown to deteriorate the noise properties. An optimized flat and close to dispersion photonic crystal fiber design was proposed, and steps were taken to reduce confinement loss. The fiber was subsequently investigated with pumping at 1064 nm through an initial step of soliton fission. While it was found to be an improvement upon current commercial sources, the noise was due to interference fringes not as low as expected.

Resumé

Supercontinuum kilder har bred anvendelse på grund af deres ekseptionelle lysstyrke, rummelig kohærens og brede spektrale dækning. Inden for feltet spektral optisk kohærens tomografi er de specielt interessante da deres spektrale bredde muliggør billeder med under en mikrometers opløsning. Disse billeder kan bruges inden for diagnostik af hud- og øjensygdomme, såvel som ikke destruktive undersøgelser af en lang række produkter. Desværre har superkontinuums kilder meget relativ intensitetsstøj, hvilket forringer billedkvaliteten i form af dårligere baggrundsstøj og lavere kontrast i forhold til andre spektralt mindre brede kilder. En del af denne afhandling er dedikeret til at sætte tal på støjen i relation til optisk kohærens tomografi på tværs af målemetoder.

Et kapitel af afhandlingen er dedikeret til en skridt for skridt udledning af den generaliserede ikke linære Schrödinger ligning, inklusiv både tapering, flere modes og "mode profile dispersion". En numerisk metode til at løse ligningen blev dernæst implementeret og testet. Den numeriske model blev brugt til at forstå hvordan "undertapering" kan reducerer relativ intensitets støj i superkontinuum nær de spektrale kanter. Modellen blev også brugt til at undersøge lav støj superkontinuum generering i normal dispersions fibre. Både Raman spredning og polarisations-modulations-instabilitet er påvist at forværre støjegenskaberne. En optimeret flad, og tæt på nul, dispersionsfiber blev designet og der blev taget skridt til at reducerer tabet. Fiberen blev dernæst undersøgt med en pumpelyskilde ved 1064 nm igennem et indledende skridt med soliton fission. Imens det var en forbedring i forhold til eksisterende kommercielle kilder, så var støjen ikke så god som forventet på grund af interferens.

Preface

The thesis focuses on the work that I have spearheaded, and does not go into detail with the work done as a co-author. But fear not, you can read all about that in the papers.

This thesis is the result of work carried out in the Shape-OCT consortium with funding from Innovation Fund Denmark (ShapeOCT-4107-00011A), under the supervision of Ole Bang. The full name of the consortium is *Spectrally shaped supercontinuum sources for high-resolution optical coherence tomography*. This thesis is part of the requirement for a Ph.D. degree from the Technical University of Denmark. During the studies from May 2015 to October 2018, numerical studies, theory and experiments were conducted at DTU Department of Photonics Engineering and to a lesser extend at NKT Photonics. Collaborators include DTU Compute, UCF CREOL, RECENDT, Bispebjerg Hospital, Rigshospitalet and University of Kent (Applied optics group in the school of physical sciences).

signature

Rasmus Dybbro Engelsholm
Department of Photonics
Technical University of Denmark
31 October 2018

Acknowledgements

It is said no man is an island, but from my short personal experience in academia it oftens seems that is exactly the case. Therefore I would like to thank my office mates without whom I would have become lost and lonely and have given up a long time ago. First and foremost on the list is Ivan Bravo Gonzalo, for whom I have the deepest professional and personal respect and who has always had time for a discussion or a laugh to brighten my day. I would like to thank Michael Maria, for the shared food and after work hours we have spent together. Manoj Kumar Dasa for his kind words and for always being there when you need him. To Kyei Kwakye, Abubakar Adamu and Mikkel Jensen for the countless breaks spent at the soccer table or goofing around. To Sophie Caujolle and Felix Fleischhauer for being delightfully silly and for putting up with me in the laboratory. And finally a thank you to my supervisor, Ole Bang, for believing in me, even at the times when I did not.

I am also grateful to NKT Photonics for letting me use their labs and their expertise. Thank you Thomas Feuchter, Peter M. Moselund and Jens K. Lyngsøfor always taking time to answer my (many) stupid questions and help me in the laboratory.

That leaves those that are too many to name, but yet too important not to mention. The research group, the research section, the institute and all the support staff attached. Thank you for making the university come alive, for providing the cosy ambiance and orderly yet flexible surroundings that enabled me to fully focus on my research.

Contents

List of Figures

List of Tables

List of Abbreviations

ANDi	All Normal Dispersion
CW	Continous Wave
CLT	Central Limit Theorem
DW	Dispersive Wave
ESA	Electrical Spectrum Analyzer
FEM	Finite Element Method
FT	Fourier Transform
FFT	Fast Fourier Transform
FWHM	Full Width Half Maximum
GNLSE	Generalized Nonlinear Schrödinger Equation
GV	Group Velocity
GVD	Group Velocity Dispersion
IR	Infrared
LE	Local Error
LEM	Local Error Method
MFD	Mode Field Diameter
MDW	Minimum Dispersion Wavelength
MLE	Maximum Likelihood Estimator
MI	Modulation Instability
NA	Numerical Aperture
NLSE	Nonlinear Schrödinger Equation
OCT	Optical Coherence Tomography
OSA	Optical Spectrum Analyzer
OWB	Optical Wave Breaking
PCF	Photonic Crystal Fiber
PD	Photodiode
PM	Polarization Maintaining
PMI	Polarization Modulation Instability
RIN	Relative Intensity Noise

RK4	Fourth order Runge-Kutta method
RK45	Fourth and Fifth order Runge-Kutta method
RKF	Runge-Kutta-Fehlberg method
SC	Supercontinuum
SCG	Supercontinuum Generation
SD-OCT	Spectral Domain Optical Coherence Tomography
SPM	Self Phase Modulation
SCG	Supercontinuum Generation
SHG	Second Harmonic Generation
SRS	Stimulated Raman Scattering
SSFS	Soliton Self Frequency Shift
TD-OCT	Time Domain Optical Coherence Tomography
UV	Ultra Violet
XPM	Cross Phase Modulation
ZDW	Zero Dispersion Wavelength

Chapter 1

Introduction and Outline

Before getting into the advanced things, it is necessary to establish the basics. The title of this thesis is *Low Noise Supercontinuum Lasers for Optical Coherence Tomography*. Optical Coherence Tomography (OCT) is an imaging method that has gotten a large amount of attention in the recent years [20,29,47,68,85], as it is a non destructive method to obtain 3D images of most kinds of materials with micro meter precision. In Fig. 1.1 is shown the number of new articles published every year containing those three keywords according to Google Scholar. The method is enormously popular as it as non destructive way of imaging things that we otherwise would not be able to see. These include applications in medicine for early detection of skin cancer [82] and diagnostic of a number of eye diseases such as glaucoma [77]. It can be used in production lines to spot structural defects inside things such as molded or 3D printet elements [28], as well as ensure that oxygen barriers in for instance food packaging is intact [84]. It can even measure pill coating thickness live during the coating process where the pills tumble around in a rotating cylinder [36].

While the technology is slowly maturing and becoming available commercially, there are a number of issues that are still in a state of flux, and are very much active research areas. The two main methods are Time Domain Optical Coherence Tomography (TD-OCT) and Spectral Domain Optical Coherence Tomography (SD-OCT). Both methods work by focusing a laser beam on the surface of a sample of interest and then measuring the light scattered by the change in refractive index down through the sample. In TD-OCT, the time delay is measured to reconstruct the layering. Usually this is done interferometrically with a Michaelson interferometer like setup, where one arm contains the sample and the other arm is used as a reference. SD-OCT also uses a Michaelson interferometer like setup, but retrieves the phase from spectral interference from broadband illumination. This method uses that the phase velocity is different at different wavelengths. This method will be explained in detail in section 2.3. Only SD-OCT will be discussed in the remainder of the thesis, and will henceforth be referred to as OCT.

Another way that OCT has not settled is in the choice of a broadband source. Some

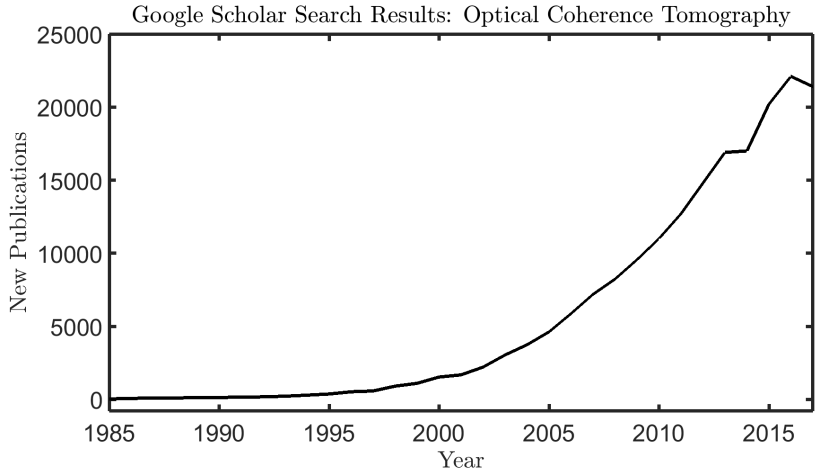

Figure 1.1: The number of new publications per year with the words *Optical Coherence Tomography* according to google scholar.

use SuperLuminescent Diodes (SLD) [63], others scanning lasers such as scanning Vertical Cavity Surface Emitting Lasers (VCSEL) [81] and others yet again use supercontinuum lasers at various wavelengths [47]. While they all have advantages and disadvantages, only supercontinuum lasers will be considered in this thesis. A supercontinuum laser is a spectrally broad laser [8, 50]. The record for the broadest span is several octaves for infrared lasers [59, 61]. It is generated through nonlinear processes, typically by the use of pulsed light in a waveguide such as an optical fiber [3, 8, 57] or on a chip [87]. Both of these environments concentrate the light enough to bring the electric fields to the required levels without the use of exotic (and expensive) lasers as pump sources. One of the disadvantages of supercontinuum sources is their tendency to fluctuate from pulse to pulse. As shall be explained in section 2.3, this noise directly leads to background noise, when the supercontinuum source is used in OCT.

The research described in this thesis explores different ways to reduce the Relative Intensity Noise (RIN) of supercontinuum sources. It is divided into the following chapters:

Chapter 2: Fibers, Supercontinuum Generation and OCT

In order to understand some of the more advanced topics, first it is necessary to grasp the fundamentals. The aim of this chapter is to introduce the most essential topics such as photonic crystal fibers, the Generalized Nonlinear Schrödinger Equation (GNLSE), various nonlinear phenomenon and the operating principles of OCT, hereunder how SC noise presents itself in OCT images.

Chapter 3: Derivation of the GNLSE from Maxwells Equations

Many different versions of the GNLSE exist. Given that the equation is not even

thirty years old, there is no general consensus on its form and shape. Choices such as normalization of the transverse fields, whether to include multiple modes, tapering and mode profile dispersion as well as which approximations were carried out in deriving the equation can be extremely confusing. This confusion can act as a barrier for newcomers to the field as well as collaboration and make it difficult to compare results. The aim of this chapter is to go through the derivation step by step of a very general form of the GNLSE and explicitly point out the approximations, and hopefully dispel some of the misconceptions that still prevail.

Chapter 4: Comparison to Litterature

The aim of this chapter is to put the derived version of the GNLSE in context in terms of some of the litterature. This is done by reduction through approximations and special cases to the equations widely accepted in the field.

Chapter 5: Numerical Implementation and Test

As with any numerical work, it can be almost impossible to distinguish between errors, mistakes and genuinly new phenomena. The burden of proof, to show that the results are correct is therefore that much greater. The aim of this chapter is to discuss the implementation and demonstrate that it is done correctly.

Chapter 6: Supercontinuum Relative Intensity Noise: Theory and Practice

Noise can be measured and quantified in many different ways, such as through spectrometer measurements, numerical simulation or pulse to pulse measurements with a photodiode connected to either an oscilloscope or an electrical spectrum analyzer. The relative intensity noise of a supercontinuum used in OCT is one of the determining factors for the final quality of an image in terms of background noise. The aim of this chapter is to establish sound practices and unify these methods in order to bring down the barriers that currently exist in between them, so that any noise measurement of a supercontinuum source can be used to estimate the resulting background noise in an OCT image.

Chapter 7: Normal Dispersion SCG for OCT at 1300nm

The first part of the chapter is dedicated to explaining the design of a flat and extremely close to zero, normal dispersion all silica PCF. This kind of fiber can suppress Raman scattering and thus prevent noise from Raman scattering. The second part of the chapter is dedicated to investigating a novel pumping scheme using redshifting solitons, in order to generate a supercontinuum centered around 1300 nm.

Chapter 8: Noise Reduction by Undertapering

It is well know that the edges in MI based supercontinuum generation is very noisy, owing to the rogue wave nature of the redshifting solitons that make up the power there. Undertapering is investigated as a method to reduce the noise associated with the rogue waves. Undertapering is when a fiber is tapered below the pitch that gives the optimal blue edge such that the second zero dispersion either sweeps through the rogue wave solitons or clamps solitons before they can redshift away from the

pump.

Chapter 9: Conclusion and Outlook

A summary of the results of the previous chapters is presented.

Chapter 2

Photonic Crystal Fibers, Supercontinuum Generation and OCT

In this chapter a few of the core concepts within fibers and supercontinuum generation will be introduced. These can also be found in textbooks, such as [2, 43, 60, 66]. At the end the general theory for OCT will be explained, and it will become clear why the RIN of the supercontinuum sources matter.

2.1 Photonic Crystal Fibers

Photonic crystal fibers (PCFs) work in much the same way as the classical step index fibers. The light is guided by a refractive index difference between a core and a cladding region. Instead of using doping to change the refractive index uniformly, a structure of air holes is used which on average lowers the refractive index of the cladding. An example of this can be seen in Fig. 2.1. In the figure, one of the most common types of PCF, the hexagonal structured solid core fiber is shown. This kind of fiber is a fairly recent development and has several advantages as well as disadvantages over other fibers. The main advantages are the degree of design freedom, the possibility of endlessly single mode fibers [54, 55] and the possibility of confining the light to a very small area. This in turn increases the nonlinear interaction. The major downside is the loss, and it comes in two ways. Firstly, there is scattering loss associated with the large, rough surface area due to the microstructuring. This is a practical problem, that has largely been resolved with improvements in manufacturing procedures. The second problem is the confinement of the modes. In a classical step index fiber the fundamental mode decays radially in an exponential manner theoretically forever. In practice until the refractive index changes again in the coating. In the hexagonal PCF, the mode stops decaying outside the region

of air holes, as the refractive index rises back up to match that of the core. Hence the number of rings is important to keep the confinement loss low. This is especially true when the hole to pitch ratio, d/Λ, is small, as this allows more light to escape between the holes.

Perhaps the most important parameter is the propagation constant. It is defined as

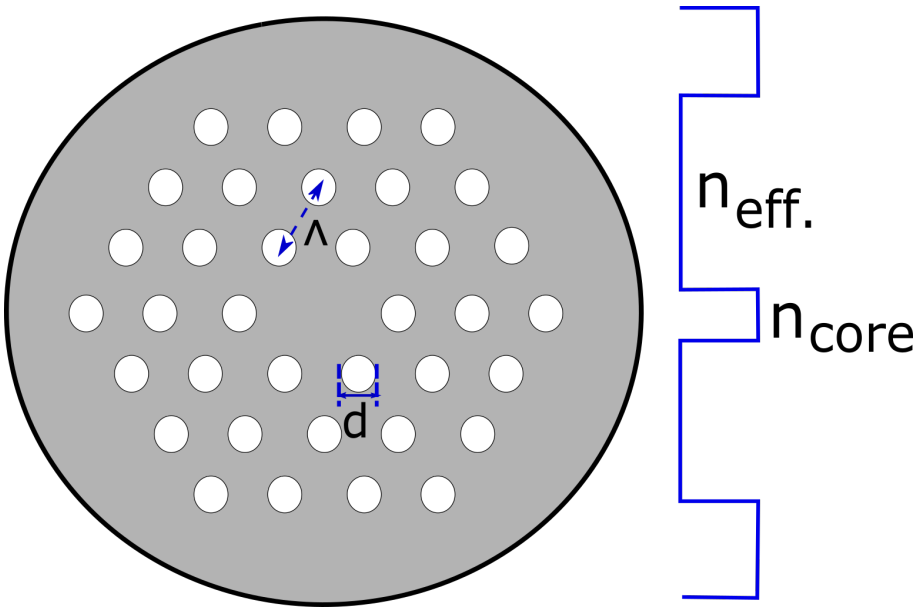

Figure 2.1: Illustration of a typical hexagonal PCF with 3 rings. The two important parameters, pitch and hole size, are marked with Λ and d respectively in the figure.

$$\beta(\omega) = \frac{\omega}{c} n_{eff} = \beta_0 + \beta_1(\omega - \omega_0) + \frac{1}{2}\beta_2(\omega - \omega_0)^2 \cdots \tag{2.1}$$

where the last equality is a Taylor expansion around the angular frequency ω_0 and $\beta_n = \frac{\partial^n \beta(\omega)}{\partial \omega^n}$ is evaluated at ω_0. n_{eff} is the effective refractive index. The Group Velocity Dispersion (GVD), β_2, determines how the different frequencies in a pulse spread. If the sign in positive, the longest wavelength light has the largest group velocity, and hence lead the pulse. This is called normal dispersion. If the sign is negative then the blue light leads the pulse. This is called anomalous dispersion. The naming convention was chosen for historic reasons, as the first glass measured, bulk silica, has normal dispersion for visible wavelengths. This can be seen in Fig. 2.2. Here also the dispersion and loss of two different PCF is shown. Note how the larger holes and larger pitch confines the light so well that the confinement loss is essential zero, and how the smaller pitch and holes is necessary to confine the light and bend the dispersion curve at higher optical frequencies. The characteristic length over which the pulse width defined at e^{-1} of the peak value is

increased by $\sqrt{2}$ due to dispersion is defined as

$$L_D = \frac{T_0^2}{|\beta_2|} \tag{2.2}$$

where T_0 is the pulse width.

A PCF can be made bifringent by introducing stress along one dimension. This can

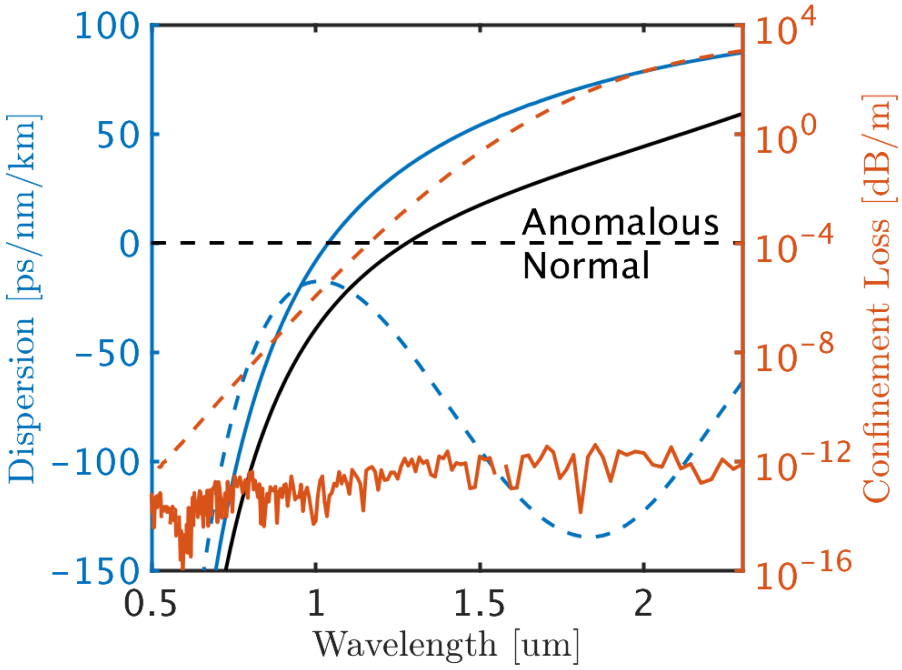

Figure 2.2: Simulated dispersion (blue) and loss (red) for two PCF's. The dotted line is for a PCF with pitch $\Lambda = 1440\,\text{nm}$ and hole size $d = 562\,\text{nm}$. The full line is for a PCF with $\Lambda = 3300\,\text{nm}$ and hole size $d = 1716\,\text{nm}$ The material dispersion of silica is shown in black.

be done by substituting holes with rods of a different material, or by placing the whole microsctructured area in between such rods. It is also possible to change the size of a few holes. The effect is to break the symmetry and change the propagation constant, so that it is different between the modes of different polarization. The difference is usually written up as a difference in the coefficients as, $\Delta\beta_n = \beta_{ny} - \beta_{nx}$. One important aspect of PCF's is that the spatial extend is different between for instance the two polarizations of the fundamental mode. This means that the overlap between those modes is less than one would expect in for instance a circular symmetric step index fiber, even when there is no bifringence.

2.2 Different Ways to Generate a Supercontinuum

In order to facilitate a discussion of some of the basics of supercontinuum generation, it is necessary to write up the GNLSE and the NLSE [2, 4, 46]. A more general version of the equation will be derived in chapter 3.

$$\frac{A(z,t)}{\partial z} = i\sum_{m\leq 1}\frac{i^m\beta_m}{m!}\frac{\partial A(t,z)}{\partial t} - \frac{\alpha}{2}A(z,t) + i\gamma\left(1+i\tau_{shock}\frac{\partial}{\partial t}\right)\left(A(z,t)\int_{-\infty}^{\infty}R(t')\left|A(z,t-t')\right|^2\,\mathrm{d}t'\right) \tag{2.3}$$

where $A(z,t)$ is the envelope, α is the loss,

$$\gamma = \frac{n_2\omega_0}{cA_{eff}(\omega_0)} \tag{2.4}$$

is the nonlinear coefficient, τ_{shock} is the shock time, $R(t)$ is the full material response and A_{eff} is the effective area. The red term describes loss, the green term is the dispersion and the blue term is the nonlinear effects. Simplifying the material response to exclude the delayed Raman part, and neglecting both the frequency dependency in the self steepening term by setting $\tau_{shock} = 0$ and the loss, we arrive at the NLSE,

$$\frac{A(z,t)}{\partial z} = i\sum_{m\leq 1}\frac{i^m\beta_m}{m!}\frac{\partial A(t,z)}{\partial t} + i\gamma A(z,t)\left|A(z,t-t')\right|^2 \tag{2.5}$$

We can see that the nonlinear part changes the phase. We can define the nonlinear length as the length for which the phase change is $\exp(1)$,

$$L_{NL} = \frac{1}{\gamma P_0} \tag{2.6}$$

There are many ways to generate a supercontinuum depending on fiber and pump parameters. Fig. 2.3 shows a rough overview of the different regimes and the effects that can lead to a supercontinuum if the pump power is high enough. The following subsections are dedicated to each of the areas in the figure, with the exception of the Raman cascade, which can be understod directly as a Raman line gaining enough power to excite another Raman line.

2.2.1 Self Phase Modulation

Perhaps the easiest way to generate a supercontinuum is by using a fiber with normal dispersion and short pulses. By direct inspection of Eq. 2.5, we can see that the nonlinear term introduces a time dependent phase change. This translates into a change in the

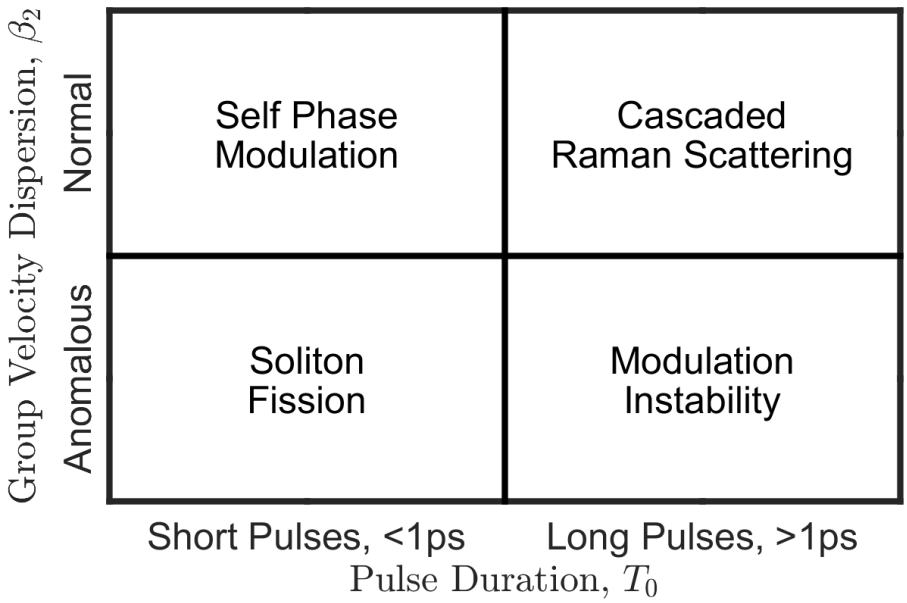

Figure 2.3: An illustration of the different effects that can generate a supercontinuum depending on pulse duration and dispersion. It assumes the peak power of the pump pulse is high enough, and the fiber is long enough to allow for sufficient nonlinear interaction.

instantaneous frequency, thus generating new frequencies. For normal dispersion fibers, the generated frequencies are shifted more to the same side of the pulse they were generated on. In other words, light with longer wavelengths are generated on the leading edge of the pulse, and has a larger group velocity than the light at the central frequency, so it will move away from the pulse. The short wavelength light is generated on the trailing edge of the pulse and also moves away from the pulse. This process can all be seen in Fig. 2.4(1-2). As the generated light moves away from the central part of the pulse, it starts to overlap with the parts of the pulse furthest away from the center in time. While they overlap, conversion to frequencies even further away from the pulse center can take place. This can be seen in Fig. 2.4(3). Once this process is complete, the pulse becomes a smooth line as seen in (4). In this stage different parts of the pulse do not overlap in either time or frequency, and thus there cannot be any interference patterns. The pulse is very smooth in both time and frequency domains. This is also described by [11, 24].

The side lobes that can be seen forming in the frequency evolution plot at the top of Fig. 2.4 and slowly expand towards the center of the pulse is very characteristic of Optical Wave Breaking (OWB). The extremely smooth spectrograms can be compressed to obtain few-cycle time-bandwidth limited pulses, much shorter than the initial pulse [76,79].

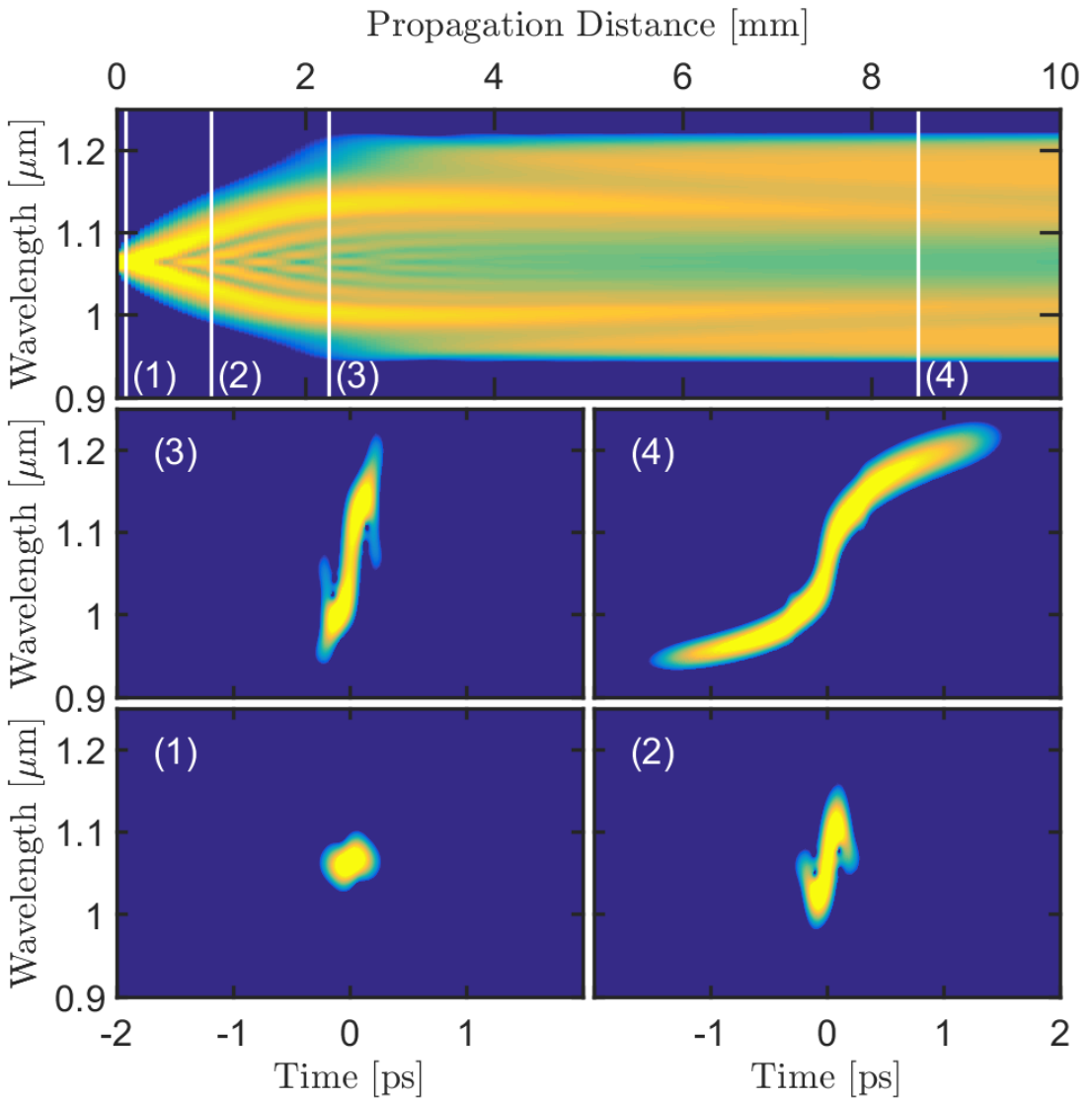

Figure 2.4: The spectral evolution in a fiber with $\beta_2 = 0.1\,\mathrm{ps}^2\,\mathrm{m}^{-1}$, $\beta_4 = 10^{-4}\,\mathrm{ps}^4\,\mathrm{m}^{-1}$, $\gamma = 0.1\,\mathrm{m}^{-1}\,\mathrm{W}^{-1}$ for a Gaussian pulse with $T_0 = 100\,\mathrm{fs}$ and $P_0 = 10\,\mathrm{kW}$. The spectrograms (1-4) correspond to the positions marked by the lines in the top figure.

2.2.2 Soliton Fission

Leaving the normal dispersion regime, and entering the anomalous dispersion regime for short pulses, a whole range of new exciting dynamics appear. The most important of them all is the possibility of soliton solutions. Solitons are solutions that do not change while propagating. They do not seem to disperse as we would normally expect. They arise even in system with nonzero dispersion in the special case when the dispersion is

exactly balanced by the nonlinear interaction. Described in words, the new frequencies generated by SPM run towards the center of the pulse instead of away from it, as was the case for normal dispersion. The condition can be expressed mathematically by the soliton number,

$$N_{sol}^2 = \frac{L_D}{L_{NL}} = \frac{\gamma P_0 T_0^2}{|\beta_2|}, \tag{2.7}$$

which is a balance between nonlinear effects and dispersion. The fundamental soliton ($N_{sol} = 1$) has a sech shape, $A(z,t) = \sqrt{P_0}\mathrm{sech}(t/T_0)$. In Fig. 2.5, the evolution with and without nonlinearity is shown, and we can see that turning the nonlinear coefficient on, prevents the pulse from broadening.

When $N_{sol} > 1$, the soliton change shape while propagating. It is however a periodic

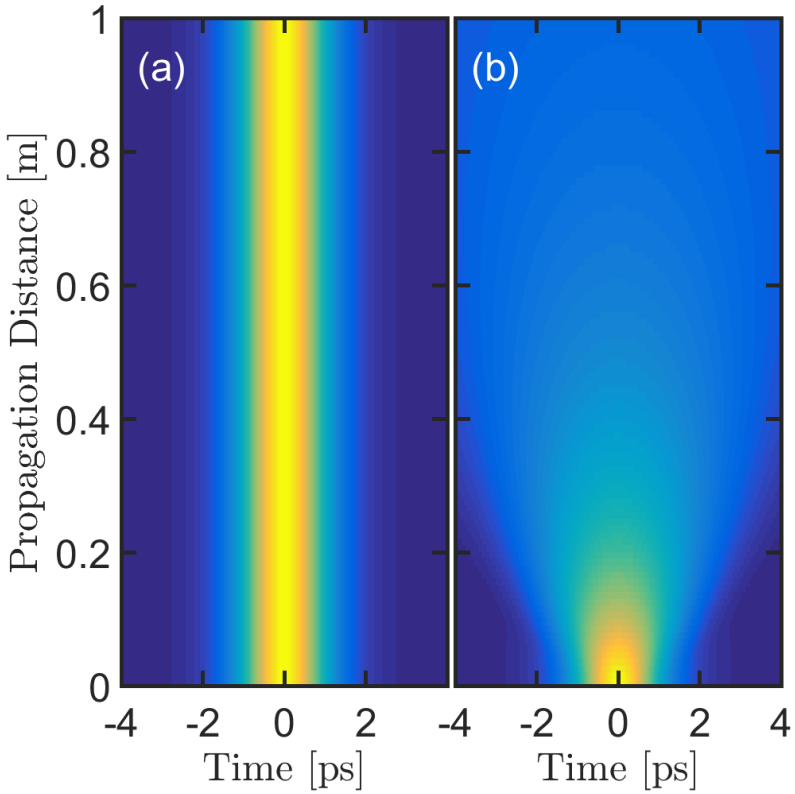

Figure 2.5: The time evolution of a fundamental soliton in a fiber with $\beta_2 = -10\,\mathrm{ps}^2\,\mathrm{m}^{-1}$ for a sech pulse with $T_0 = 1\,\mathrm{ps}$ and $P_0 = 100\,\mathrm{W}$. (a) $\gamma = 0.1\,\mathrm{m}^{-1}\,\mathrm{W}^{-1}$, (b) $\gamma = 0\,\mathrm{m}^{-1}\,\mathrm{W}^{-1}$.

oscillation where energy spreads out and then contracts again. Hence it can still be called a soliton solution. An example of this can be seen in Fig. 2.6(a). However, if a small pertubation is added to the system that does not have the same symmetry, for instance Raman scattering or higher order dispersion such as $\beta_3 \neq 0$, then the pulse can no longer contract again to rediscover the original shape. This can be seen in Fig. 2.6(b). Instead a

number of fundamental solitons are ejected. Usually not quite N_{sol} fundamental solitons, due to an imperfect breakup where energy is lost to dispersive waves, but it can be quite close.

Another possibility is the emergence of dispersive waves [2,18,78]. The nonlinear refractive

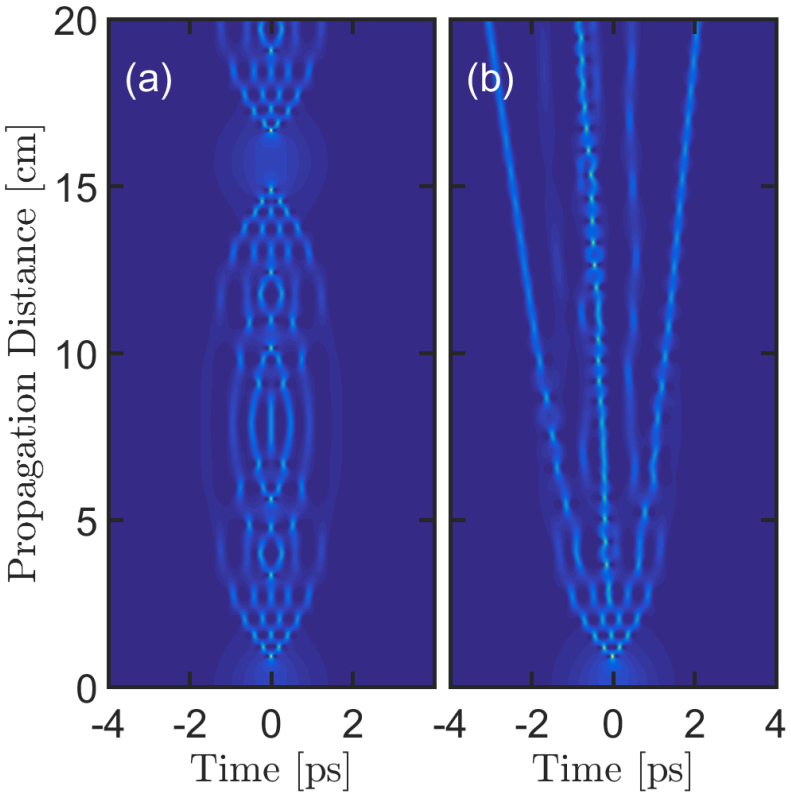

Figure 2.6: The time evolution of an 8th order soliton in a fiber with $\beta_2 = -10\,\mathrm{ps}^2\,\mathrm{m}^{-1}$, $\gamma = 0.1\,\mathrm{m}^{-1}\,\mathrm{W}^{-1}$ for a sech pulse with $T_0 = 1\,\mathrm{ps}$ and $P_0 = 6.4\,\mathrm{kW}$. (a) $\beta_3 = 0\,\mathrm{ps}^2\,\mathrm{m}^{-1}$, (b) $\beta_3 = 0.1\,\mathrm{ps}^3\,\mathrm{m}^{-1}$.

index from a soliton acts as barrier in time for light at other frequencies. Normally the mismatch in group velocity means the non solitonic light can easily smash through the potential barrier, but for the right match of group velocity it is possible to trap light. This is called a dispersive wave. They usually occur when a soliton becomes broad enough that it both acts as the barrier and at the same time has frequency components that can fit in the potential. An example of this can be seen in Fig. 2.7. The black line is the approximate wavelength at which light can be trapped by the soliton, calculated from

$$\beta(\omega) = \beta(\omega_{sol}) + \beta_1(\omega - \omega_{sol}) + \frac{1}{2}\gamma P_{sol}. \tag{2.8}$$

As can be seen in the figure, the light from the soliton is slowly siphoned into the sink at 1010 nm, where it builds up.

The last phenomenon of interest arises due to the Raman scattering present in Eq. (2.3).

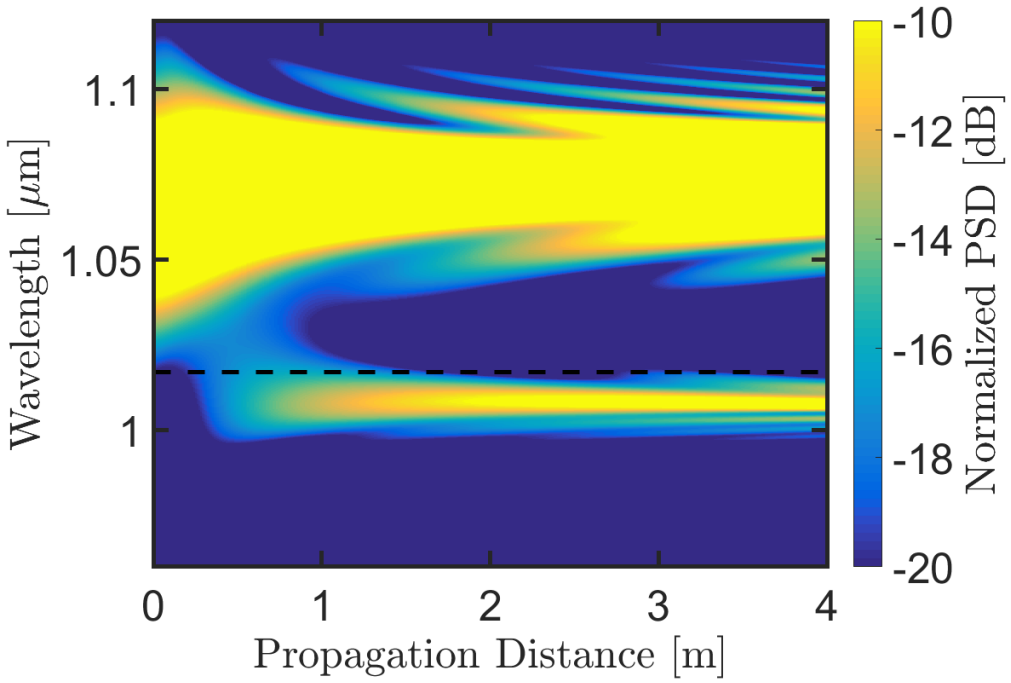

Figure 2.7: The frequency evolution of a fundamental soliton in a fiber with $\beta_2 = -0.002\,\mathrm{ps}^2\,\mathrm{m}^{-1}$, $\beta_3 = 10^{-4}\,\mathrm{ps}^3\,\mathrm{m}^{-1}$, $\gamma = 0.025\,\mathrm{m}^{-1}\,\mathrm{W}^{-1}$ for a sech pulse with $T_0 = 20\,\mathrm{fs}$ and $P_0 = 200\,\mathrm{W}$. The dotted line is the phasematching condition as described by Eq. (2.8).

Som fundamental solitons are so narrow in time, that they extend past the Raman peak at 13.2 THz. The pulse can thus act as both pump and probe for a continous stimulated Raman scattering process, where energy is lost to phonons. Such solitons experience a continous redshift, and due to their stability as a soliton, they do not disperse, but can keep redshifting in a fiber until they are overcome by fiber loss or the dispersion changes sign so that the soliton is no longer viable [69]. An example of such a redshift in a lossless fiber can be seen in Fig. 2.8. An approximate expression for the redshift rate from [2] is

$$\frac{\partial \omega_{sol}}{\partial z} = -\frac{8T_R\,|\beta_2|}{15T_0^4} \qquad T_0 >> 76\,\mathrm{fs} \tag{2.9}$$

$$\frac{\partial \omega_{sol}}{\partial z} = -0.09\frac{|\beta_2|\,\omega_R^2}{T_0} \qquad T_0 \leq 76\,\mathrm{fs} \tag{2.10}$$

where $T_R \approx 3\,\mathrm{fs}$ and ω_R is the Raman peak at 13.2 THz for silica glass.

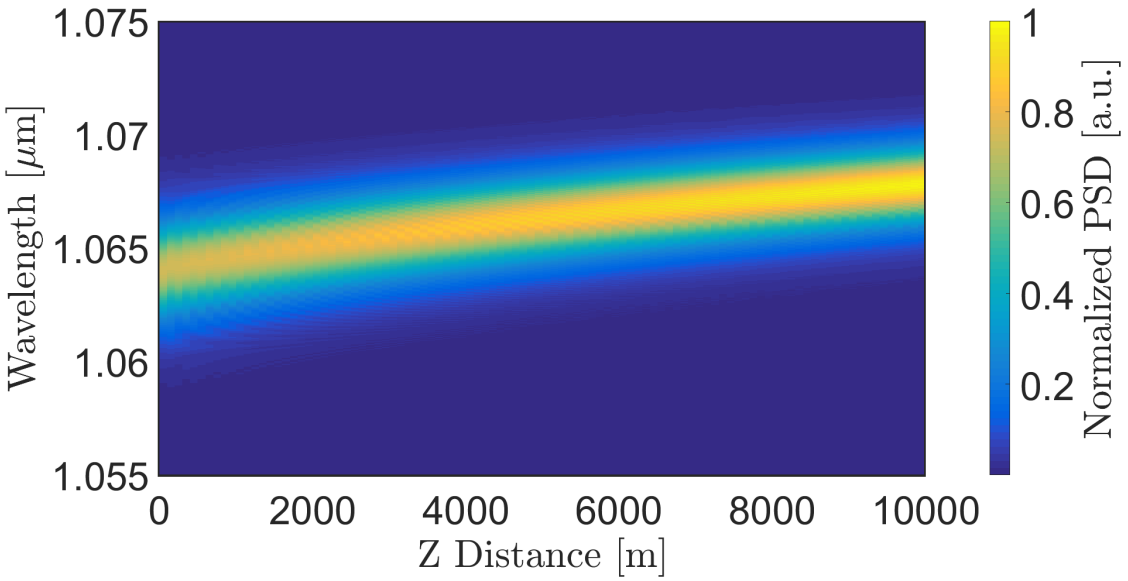

Figure 2.8: The frequency evolution of a fundamental soliton undergoing soliton self frequency shift in a fiber with $\beta_2 = -0.002\,\mathrm{ps}^2\,\mathrm{m}^{-1}$, $\beta_3 = 10^{-4}\,\mathrm{ps}^3\,\mathrm{m}^{-1}$, $\gamma = 0.025\,\mathrm{m}^{-1}\,\mathrm{W}^{-1}$ for a sech pulse with $T_0 = 200\,\mathrm{fs}$ and $P_0 = 200\,\mathrm{W}$.

2.2.3 Modulation Instability

The last case is the case of long pulses and anomalous dispersion. When perturbing the perfect pulse, it turns out that the pulse is unstable. Small fluctuations at the peak power begin to grow, and then, depending on the soliton number, the pulse splits up into many solitons. For the initial breakup, it is possible to show that the small perturbations take on a special form in the spectral domain. The gain is given by

$$g_{MI}(\omega) = \mathrm{Re}\left(|\beta_2\omega|\left(\frac{4\gamma P_0}{|\beta_2|} - \omega^2\right)^{1/2}\right) \qquad \omega_{\max} = \pm\left(\frac{2\gamma P_0}{|\beta_2|}\right)^{1/2} \qquad L_{\mathrm{gain}} = \frac{1}{2\gamma P0} \tag{2.11}$$

where $\omega_{\max}$ is the frequency with the maximum gain. L_{gain} is the power gain, and is thus defined as the distance after which the intensity is increased by a factor exp (1).

As the pulse begins to break up into many smaller solitons, the initial pertubation theory becomes ill suited for predictions. Instead the Akhmediev Breather theory can be applied [7, 9, 19, 32]. This is excellent at predicting the pedestal in the frequency domain, with evenly spaced peaks every $\omega_{\max}$ from the pump. As we saw with the 8th order soliton, higher order dispersion broke the symmetry and prevented the pulse from collecting itself again. The same principle applies to the breather. As a result, a chaotic state appears where a lot of fundamental solitons are created, and constantly collide with each other,

with the possibility of energy transfer. Eventually, from this sea of solitons a few big fundamental solitons emerge. These are short enough in time and have high enough peak power that they can redshift through SSFS. This broadens the spectrum further, but since the initial breakup was noise seeded, and the sea of solitons is a chaotic process, the ejection of single large redshifting solitons is a very chaotic event. This is what gives rise to the rogue wave statistics that is often associated with MI SC [13, 41, 70, 71]. If the pump is initially situated close to the ZDW, such as a 1064 nm pump for the $\Lambda = 3.3\,\mu$m dispersion curve shown in Fig. 2.2, then the solitons can trap GV matched light across the ZDW. As the soliton redshifts, the trapped light is forced to blueshift [72, 78]. This is the mechanic behind the extremely broadband supercontinuum sources that are available commercially today, and is thus of great interest.

2.3 Spectral Domain Optical Coherence Tomography

In SD-OCT, broadband light is sent into a Michelson interferometer as seen in Fig. 2.9(a). The mirror in one arm is replaced with a lens, focusing on, and collecting light from, a sample. In the sample, a phase is accumulated, that is almost linear in frequency. At every interface down through the sample, part of the light is reflected, and thus the phase accumulation depends on twice the length propagated inside the sample. In the other arm, which should have the same optical length, there is a reflector, typically a mirror, and possibly dispersion compensation to ensure the dispersion difference between the two arms is minimized. Upon returning to the beam splitter, the two beams are interfered, and the linear phase information of the sample is retrieved. It is a type of homodyne detection, where the very weak signal from the reflected light from the sample is boosted by the reference, and then detected with a spectrometer to retrieve the phase.

A mathematical model for the signal light measured by the spectrometer based on modelling the sample as a sum of N_R reflectors and assuming weak attenuation down through the sample is [6],

$$\begin{aligned}\tilde{I}_D(k) = &\frac{\rho}{4}\left[\tilde{S}(k)\left(R_R + \sum_{n=1}^{N_R} R_{S,n}\right)\right] \\ &+ \frac{\rho}{4}\left[\tilde{S}(k)\sum_{n\neq m=1}^{N_R}\sqrt{R_{S,n}R_{S,m}}\cos\left(2k\left(z_{s,n} - z_{S,m}\right)\right)\right] \\ &+ \frac{\rho}{2}\left[\tilde{S}(k)\sum_{n=1}^{N_R}\sqrt{R_{S,n}R_R}\cos\left(2k\left(z_R - z_{S,n}\right)\right)\right] \quad , \end{aligned} \tag{2.12}$$

where $\tilde{S}(k)$ is the broadband light source signal in k space (which could be a SC), ρ is the detector responsivity, R are the different reflectors and z is the position of them. The first term (red) is the DC term. The second term (green) is the auto correlation term and

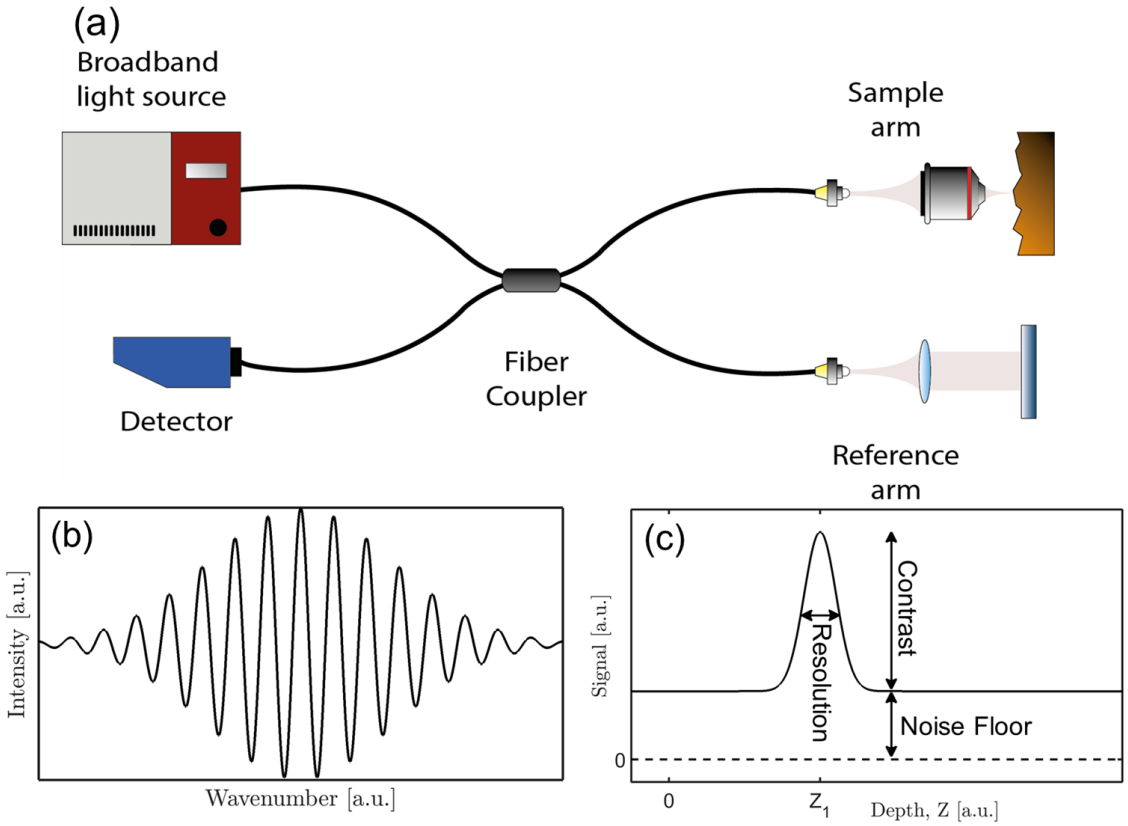

Figure 2.9: (a) Setup for SD-OCT. Borrowed with permission from Ivan Bravo Gonzalo. (b) Example of interference measured in the spectrometer in (a), after subtraction of and normalization with the reference. (c) The depth information obtained by applying an inverse Fourier transform to the spectral data in (b). This is also known as an A-scan.

the last term (blue) is the cross correlation term. The sum in the auto correlation term should be understod as running over all $n \neq m$, as those terms are moved to the DC term. Since the reflections from the sample are much smaller than the mirror in the reference arm, $R_{S,n} \ll R_R$, the expression can be reduced to

$$\begin{aligned} \tilde{I}_D(k) \approx & \frac{\rho}{4}\left[\tilde{S}(k)\ R_R\right] \\ & + \frac{\rho}{2}\left[\tilde{S}(k)\sum_{n=1}^{N_R}\sqrt{R_{S,n}R_R}\cos\left(2k\left(z_R - z_{S,n}\right)\right)\right] \end{aligned} \tag{2.13}$$

Taking the inverse Fourier transform and using the convolution theorem, the equation becomes

$$I_D(z) \approx \frac{\rho}{8}\left[S(z) \otimes \delta(z)\ R_R\right]$$

$$+\frac{\rho}{4}\left[S(z)\otimes\sum_{n=1}^{N_R}\sqrt{R_{S,n}R_R}\delta\left(z\pm 2\left(z_R-z_{S,n}\right)\right)\right]$$
$$=\frac{\rho}{8}R_R S(z)\otimes\left[\delta(z)+\sum_{n=1}^{N_R}\sqrt{\frac{R_{S,n}}{R_R}}\delta\left(z\pm 2\left(z_R-z_{S,n}\right)\right)\right] \quad . \tag{2.14}$$

From Eq. (2.14) a few things are immediatly obvious. The bandwidth of the source $\tilde{S}(k)$ determines the maximal spectral width of the depth signal, and hence the maximal resolution. The wider the bandwidth of the source, the better the resolution will be. For a Gaussian intensity profile $\tilde{S}(k)$, the best possible resolution will be

$$\Delta z=\frac{2\ln 2}{\pi}\frac{\lambda_0^2}{\Delta\lambda} \tag{2.15}$$

where Δz and $\Delta\lambda$ are the FWHM widths, and λ_0 is the central wavelength. We now see why the DC term is called a DC term. It is present as a peak at zero, and its width is inversely proportional to the spectral width of the source, $\tilde{S}(k)$. Usually it is subtracted in k-space by subtracting the reference signal. This is the spectrum obtained when the sample arm is blocked. The interference in k-space is also normalized by the same, $S(z)$, so that only the signal from the sample is left. An illustration for the case of a single reflector can be seen in Fig. 2.9 (b). After the application of the inverse Fourier transform, the depth information becomes readily visible as seen in Fig. 2.9 (c).

If $\tilde{S}(k)$ has some Gaussian distributed white noise, then there will also be Gaussian distributed white noise in $S(z)$. This noise, coming from the reference arm, is still present even after the subtraction of, and normalization with, the average reference. With the normalization, it is now the RIN of the source and not the noise directly that matters. It is directly responsible for the noise floor in the final image, if it is higher than the noise in the electronic readout and the shot noise. This is the case for most OCT systems using supercontinuum sources [5, 47].

In OCT, the spectrometers used are much slower than the pulse repetition rate. Therefore a single readout is typically a sum of many pulses. For Gaussian distributed noise, this lowers the relative noise. Increasing the exposure time will thus decrease the effective source noise, at the cost of a slower scan rate. The noise inherent in the light is not the only noise. There are also two other major noise contributions, such as electronic noise (dark noise, readout noise) and shot noise. These arrive from readout in the spectrometer. With the exception of dark noise, they are unaffected by the change in integration time if the total energy incident on the spectrometer during the exposure time is kept constant. In most OCT measurements involving supercontinuum sources, it is therefore possible to make shot or electronic noise limited measurements if the exposure time is long enough, as seen by the measurements in [5, 47]. This makes for some very slow systems, and is not feasible for in vivo imaging. It is therefore important to make supercontinuum sources that have a high repetition rates, low noise, or preferably both, in order to compete with other types of sources in terms of low noise.

Chapter 3

Derivation of the generalized non linear Schrödinger equation in optical fibers from Maxwells equations

In this section I will derive the generalized non linear Schrödinger equation (GNLSE) directly from Maxwell's equations in an optical fiber. The end results will include tapering and multiple modes with all polarization states and the effect of mode profile dispersion. Then I will proceed to show that in the special case of no mode profile dispersion and only a single polarization per mode, the result reduces to the known GNLSE, which includes four Fourier transforms. It turns out the obtained equation is naturally in the interaction picture, but, as i will show, a quick transform is enough to show that it can also be written as a sum of the dispersive and nonlinear operators. Special emphasis will be on the various approximations (which will be marked with italic text styling for quick referencing and overview) and all the small tricks used in the derivation.

Throughout the derivation the definition of the Fourier transform and the delta function will be used multiple times. Therefore it is appropriate to start by defining these as

$$\mathcal{F}\left[A\left(t\right)\right]=\tilde{A}\left(\Omega\right)=\int_{-\infty}^{\infty}A\left(t\right)\exp\left(-i\Omega t\right)\,\mathrm{d}t \tag{3.1}$$

$$\mathcal{F}^{-1}\left[\tilde{A}\left(\Omega\right)\right]=A\left(t\right)=\frac{1}{2\,\pi}\int_{-\infty}^{\infty}\tilde{A}\left(\Omega\right)\exp\left(i\Omega t\right)\,\mathrm{d}\Omega \tag{3.2}$$

$$\delta\left(t_1-t_2\right)=\frac{1}{2\,\pi}\int_{-\infty}^{\infty}\exp\left(i\left(t_1-t_2\right)\Omega\right)\,\mathrm{d}\Omega \tag{3.3}$$

where Ω is the usual angular frequency. The above definition is the same used by Matlab. Note how the tilde denotes a variable that has been transformed into the frequency domain.

Since there will be a lot of Fourier transforms in the following, whenever there are no limits on the integrals, it means they run from minus infinity to infinity. As we shall see within a couple of pages, it will also be necessary with a mathematical vector calculus identity,

$$\mathbf{A} \cdot (\nabla \times \mathbf{B}) = \mathbf{B} \cdot (\nabla \times \mathbf{A}) - \nabla \cdot (\mathbf{A} \times \mathbf{B}) \tag{3.4}$$

where $\mathbf{A}$ and $\mathbf{B}$ are arbitrary vector fields, and ∇ is the del or nabla operator. The bold font means we are dealing with a vector variable. Now we are ready to derive the GNLSE.

3.1 Envelope changes due to the nonlinear polarization

We begin from Maxwells equations. For electromagnetic waves in matter, these are

$$\nabla \cdot \mathbf{D} = \rho_f \tag{3.5a}$$
$$\nabla \cdot \mathbf{H} = 0 \tag{3.5b}$$
$$\nabla \times \mathbf{E} = -\mu_0 \frac{\partial \mathbf{H}}{\partial t} \tag{3.5c}$$
$$\nabla \times \mathbf{H} = \mathbf{J}_f + \frac{\partial \mathbf{D}}{\partial t} \tag{3.5d}$$

where $\mathbf{E}$, $\mathbf{B}$, $\mathbf{D}$ and $\mathbf{H}$ are the electric, magnetic, displacement and magnetizing fields respectively. ρ_f and $\mathbf{J}_f$ are the free charges and free currents, which in the following will be set to zero, as we are working with charge neutral non conductive materials in our fibers. Likewise there is no induced magnetization, so the ratio between the magnetic and magnetizing fields is the vacuum permeability. Using the definition of the displacement field and writing the polarization as a sum between the linear and nonlinear ($\mathbf{P}_{NL}$) contributions,

$$\mathbf{D} = \epsilon_0 \mathbf{E} + \epsilon_0 \chi^{(1)} \mathbf{E} + \mathbf{P}_{NL} = \epsilon_0 \epsilon_r \mathbf{E} + \mathbf{P}_{NL} \tag{3.6}$$

where ϵ_r is the relative electric permittivity, we can rewrite Maxwell's equations to

$$\nabla \cdot \mathbf{D} = 0 \tag{3.7a}$$
$$\nabla \cdot \mathbf{H} = 0 \tag{3.7b}$$
$$\nabla \times \mathbf{E} = -\mu_0 \frac{\partial \mathbf{H}}{\partial t} \tag{3.7c}$$
$$\nabla \times \mathbf{H} = \epsilon_0 \frac{\partial \left(\epsilon_r \mathbf{E}\right)}{\partial t} + \frac{\partial \mathbf{P}_{NL}}{\partial t} \tag{3.7d}$$

From here, the method used by Kolesik et al. [34] and Laegsgaard [40] will be used, as I find it to be more elegant than the original method used by Blow and Wood [4] and Chernikov and Mamyshev [46]. However, in the end the two methods give the same result seen in Eq. (3.31). The first step in this method is to see that we can split the fields into a product of different spectral and spatial components. This is done by applying the

inverse Fourier transform and write the fields, in the frequency domain, as a sum over all the different modes as

$$\mathbf{E}(\tau,x,y,z)=\frac{1}{2\pi}\int\sum_m \tilde{A}_m(\Omega,z)\,\boldsymbol{\mathcal{E}}_m(\Omega,x,y,z)\exp\left(i\int_0^z\hat{\beta}_m\left(\Omega,z'\right)\,\mathrm{d}z'+i\Omega\tau\right)\mathrm{d}\Omega \tag{3.8a}$$

$$\mathbf{H}(\tau,x,y,z)=\frac{1}{2\pi}\int\sum_m \tilde{A}_m(\Omega,z)\,\boldsymbol{\mathcal{H}}_m(\Omega,x,y,z)\exp\left(i\int_0^z\hat{\beta}_m\left(\Omega,z'\right)\,\mathrm{d}z'+i\Omega\tau\right)\mathrm{d}\Omega \tag{3.8b}$$

where $\boldsymbol{\mathcal{E}}_m(\Omega,x,y,z)$ and $\boldsymbol{\mathcal{H}}_m(\Omega,x,y,z)$ include the polarization state and transverse field profiles (the transverse field profile can depend on z when working with tapers) while the sum is over all the different modes and polarization states. $\tilde{A}_m(\Omega,z)$ is the complex weight of each frequency Ω at position z. In the sense that each frequency is decoupled, it can also be understod as the complex amplitude of both frequency and spatial modes.

Now let us Taylor expand $\hat{\beta}_m$ around ω_0, and define $\omega\equiv\Omega-\omega_0$. The notation $\hat{\beta}_{mn}(z')$ should be understod as the n'th order derivative of $\hat{\beta}_m(\Omega,z')$ at $\Omega=\omega_0$ or equivalently at $\omega=0$. That way we can write the fields as

$$\begin{aligned}\mathbf{E}(\tau,x,y,z)=&\frac{1}{2\pi}\int\sum_m\tilde{A}_m(\Omega,z)\,\boldsymbol{\mathcal{E}}_m(\Omega,x,y,z)\\&\exp\left(i\int_0^z\hat{\beta}_{m0}\left(z'\right)+\hat{\beta}_{m1}\left(z'\right)(\Omega-\omega_0)+\sum_{n=2}^{\infty}\frac{\hat{\beta}_{mn}(z')}{n!}(\Omega-\omega_0)^n\,\mathrm{d}z'+i\Omega\tau\right)\mathrm{d}\Omega\end{aligned} \tag{3.9a}$$

$$\begin{aligned}\mathbf{H}(\tau,x,y,z)=&\frac{1}{2\pi}\int\sum_m\tilde{A}_m(\Omega,z)\,\boldsymbol{\mathcal{H}}_m(\Omega,x,y,z)\\&\exp\left(i\int_0^z\hat{\beta}_{m0}\left(z'\right)+\hat{\beta}_{m1}\left(z'\right)(\Omega-\omega_0)+\sum_{n=2}^{\infty}\frac{\hat{\beta}_{mn}(z')}{n!}(\Omega-\omega_0)^n\,\mathrm{d}z'+i\Omega\tau\right)\mathrm{d}\Omega\end{aligned}\quad. \tag{3.9b}$$

It is a hassle to work in the real physical time, τ, since we would need to constantly change time window to follow any pulse moving in time, while we propagate in z. The way to get around this is to introduce a moving time frame, where we follow the pulse. The pulse will initially move with the speed of the first derivative of $\hat{\beta}_m$. Since we will mostly pump in the fundamental mode, and there would be a lot of bookkeeping involved in a seperately moving time frame for each mode, we decide that the time frame should move with the first fundamental mode, $m=1$. Mathematically, we can see directly from Eq. (3.9a) and (3.9b) that we would need to chose

$$\tau=t-t_0=t-\int_0^z\hat{\beta}_{11}\left(z'\right)\mathrm{d}z' \tag{3.10}$$

to get rid of the first derivative of $\hat{\beta}_1(\Omega, z')$. Substituting this in, we arrive at

$$\begin{aligned}\mathbf{E}(\tau,x,y,z) =&\frac{1}{2\pi}\int\sum_m \tilde{A}_m(\Omega,z)\,\boldsymbol{\mathcal{E}}_m(\Omega,x,y,z)\\ &\exp\left(i\int_0^z \hat{\beta}_{m0}(z') - i\omega_0\hat{\beta}_{11}(z')\right.\\ &\left.+\left[\hat{\beta}_{m1}(z')-\hat{\beta}_{11}(z')\right](\Omega-\omega_0)+\sum_{n=2}^{\infty}\frac{\hat{\beta}_{mn}(z')}{n!}(\Omega-\omega_0)^n\,\mathrm{d}z' + i\Omega t\right)\mathrm{d}\Omega\end{aligned} \tag{3.11a}$$

$$\begin{aligned}\mathbf{H}(\tau,x,y,z) =&\frac{1}{2\pi}\int\sum_m \tilde{A}_m(\Omega,z)\,\boldsymbol{\mathcal{H}}_m(\Omega,x,y,z)\\ &\exp\left(i\int_0^z \hat{\beta}_{m0}(z') - i\omega_0\hat{\beta}_{11}(z')\right.\\ &\left.+\left[\hat{\beta}_{m1}(z')-\hat{\beta}_{11}(z')\right](\Omega-\omega_0)+\sum_{n=2}^{\infty}\frac{\hat{\beta}_{mn}(z')}{n!}(\Omega-\omega_0)^n\,\mathrm{d}z' + i\Omega t\right)\mathrm{d}\Omega.\end{aligned} \tag{3.11b}$$

To make the equations more manageable, we define a new phase as

$$\begin{aligned}\phi_m(\Omega,z) &= \int_0^z \hat{\beta}_{m0}(z') - i\omega_0\hat{\beta}_{11}(z') + \left[\hat{\beta}_{m1}(z')-\hat{\beta}_{11}(z')\right](\Omega-\omega_0)+\sum_{n=2}^{\infty}\frac{\hat{\beta}_{mn}(z')}{n!}(\Omega-\omega_0)^n\,\mathrm{d}z'\\ &= \int_0^z \beta_m(\Omega,z')\,\mathrm{d}z',\end{aligned} \tag{3.12}$$

where $\beta_m(\Omega, z')$ (note: without the hat) will become relevant later, as it is the extra factor obtained when taking the z derivative of $\exp(\phi_m(\Omega, z))$. The decomposed equations are then

$$\begin{aligned}\mathbf{E}(t,x,y,z) =&\frac{1}{2\pi}\int\sum_m \tilde{A}_m(\Omega,z)\,\boldsymbol{\mathcal{E}}_m(\Omega,x,y,z)\\ &\exp\left(i\phi_m(\Omega,z)+i\Omega t\right)\mathrm{d}\Omega\end{aligned} \tag{3.13a}$$

$$\begin{aligned}\mathbf{H}(t,x,y,z) =&\frac{1}{2\pi}\int\sum_m \tilde{A}_m(\Omega,z)\,\boldsymbol{\mathcal{H}}_m(\Omega,x,y,z)\\ &\exp\left(i\phi_m(\Omega,z)+i\Omega t\right)\mathrm{d}\Omega,\end{aligned} \tag{3.13b}$$

or in frequency domain as

$$\tilde{\mathbf{E}}(\Omega,x,y,z) = \sum_m \tilde{A}_m(\Omega,z)\,\boldsymbol{\mathcal{E}}_m(\Omega,x,y,z)\exp\left(i\phi_m(\Omega,z)\right), \tag{3.14a}$$

$$\tilde{\mathbf{H}}(\Omega,x,y,z) = \sum_m \tilde{A}_m(\Omega,z)\,\boldsymbol{\mathcal{H}}_m(\Omega,x,y,z)\exp\left(i\phi_m(\Omega,z)\right). \tag{3.14b}$$

Now that this little mathmatical digression has come to an end, it might be prudent to make a short summary. By changing to a moving time frame we reduce the complexity of the numerical scheme we will need later. The only cost was a suitable redefinition of our phase.

Returning to Maxwell's equations, let us dot the curl Maxwell equations, Eq. (3.7c) and (3.7d), in the frequency domain, with the complex conjugated transverse magnetizing, $\widehat{\boldsymbol{\mathcal{H}}}^*$, and electric, $\widehat{\boldsymbol{\mathcal{E}}}^*$, field components combined with their conjugated phase envelopes. Note the hat on $\widehat{\boldsymbol{\mathcal{E}}}^*$ and $\widehat{\boldsymbol{\mathcal{H}}}^*$, which means the fields are normalised by a yet to be determined normalisation factor, $N_m(\Omega, z)$,

$$\widehat{\boldsymbol{\mathcal{E}}}_m(\Omega, x, y, z) = \frac{\boldsymbol{\mathcal{E}}_m(\Omega, x, y, z)}{N_m(\Omega, z)} \qquad \widehat{\boldsymbol{\mathcal{H}}}_m(\Omega, x, y, z) = \frac{\boldsymbol{\mathcal{H}}_m(\Omega, x, y, z)}{N_m(\Omega, z)}, \tag{3.15}$$

which gives

$$\begin{aligned}
&\left[\exp\left(i\phi_n(\Omega, z)\right)\widehat{\boldsymbol{\mathcal{H}}}_n(\Omega, x, y, z)\right]^* \cdot \left[\nabla \times \mathbf{E}(\Omega, x, y, z)\right] \\
&\quad = i\mu_0\Omega\left[\exp\left(i\phi_n(\Omega, z)\right)\widehat{\boldsymbol{\mathcal{H}}}_n(\Omega, x, y, z)\right]^* \cdot \mathbf{H}(\Omega, x, y, z), \qquad (3.16a) \\
&\left[\exp\left(i\phi_n(\Omega, z)\right)\widehat{\boldsymbol{\mathcal{E}}}_n(\Omega, x, y, z)\right]^* \cdot \left[\nabla \times \mathbf{H}(\Omega, x, y, z)\right] \\
&\quad = -i\Omega\left[\exp\left(i\phi_n(\Omega, z)\right)\widehat{\boldsymbol{\mathcal{E}}}_n(\Omega, x, y, z)\right]^* \\
&\cdot \left(\epsilon_0\left(\epsilon_r\mathbf{E}(\Omega, x, y, z)\right) + \mathbf{P}_{NL}(\Omega, x, y, z)\right). \qquad (3.16b)
\end{aligned}$$

From here on, the dependence on Ω, x, y, z are still there, but due to paper size constraints it is omitted until the equation has been reduced a bit. The complex conjugated phase terms introduced will follow their polarization fields, but otherwise remain unchanged. Now the vector identity in Eq. (3.4) can be used to rewrite the two curl terms, so the equations become

$$\begin{aligned}
&\mathbf{E} \cdot \left(\nabla \times \left[\exp\left(i\phi_n(\Omega, z)\right)\widehat{\boldsymbol{\mathcal{H}}}_n\right]^*\right) \\
&- \nabla \cdot \left(\left[\exp\left(i\phi_n(\Omega, z)\right)\widehat{\boldsymbol{\mathcal{H}}}_n\right]^* \times \mathbf{E}\right) \\
&\qquad = -i\Omega\mu_0\left[\exp\left(i\phi_n(\Omega, z)\right)\widehat{\boldsymbol{\mathcal{H}}}_n\right]^* \cdot \mathbf{H}, \qquad (3.17a) \\
&\mathbf{H} \cdot \left(\nabla \times \left[\exp\left(i\phi_n(\Omega, z)\right)\widehat{\boldsymbol{\mathcal{E}}}_n\right]^*\right) \\
&- \nabla \cdot \left(\left[\exp\left(i\phi_n(\Omega, z)\right)\widehat{\boldsymbol{\mathcal{E}}}_n\right]^* \times \mathbf{H}\right) \\
&\qquad = i\Omega\left[\exp\left(i\phi_n(\Omega, z)\right)\widehat{\boldsymbol{\mathcal{E}}}_n\right]^* \cdot \left(\epsilon_0\epsilon_r\mathbf{E} + \mathbf{P}_{NL}\right). \qquad (3.17b)
\end{aligned}$$

In order to proceed from here we have to make the *assumption that each individual mode satisfies Maxwell's equations when the nonlinear term is neglected. This is equivalent to assuming the induced nonlinear polarization is a small perturbation to the electric field,*

that does not change the modes. Furthermore, the transverse mode profiles have a dependence on the z coordinate in a taper, which is not included when calculating the modes. This means that we can not use Eq. (3.5c) and (3.5d) directly. Instead we remember that there is now a z dependence inherent in the expressions. By using the following Maxwell equations, with the z derivative explicitly written out, it should be clear that the z dependence is moved from being implicit in the tapered mode equations into being explicit, so the transverse fields match those of normal, untapered modes. This means, for a given z we can calculate the transverse modes using the normal mode equations and use them directly in the place for $\mathcal{E}$ and $\mathcal{H}$ in the equations below, even though these change with z. For all intents and purposes the derivatives due to tapering has been moved from the modes and into the envelope equations, so that modes may be calculated with the untapered mode equations for any given z. To see that Eq. 3.18a and 3.18b are really Maxwells equations, note that normally when doing the curl there are two z-derivatives that are set to zero. This is not the case anymore. Writing these out explicitly from the curl, the last term in each equation is obtained.

$$\begin{aligned}
&\nabla \times \left[\exp\left(i\phi_n\left(\Omega,z\right)\right)\widehat{\boldsymbol{\mathcal{H}}}_n\left(\Omega,x,y,z\right)\right]^* \\
&= i\Omega\epsilon_0\epsilon_r\left[\widehat{\boldsymbol{\mathcal{E}}}_n\left(\Omega,x,y,z\right)\exp\left(i\phi_n\left(\Omega,z\right)\right)\right]^* \\
&\quad - \left[\exp\left(i\phi_n\left(\Omega,z\right)\right)\hat{\boldsymbol{z}}\times\frac{\partial\widehat{\boldsymbol{\mathcal{H}}}_n\left(\Omega,x,y,z\right)}{\partial z}\right]^* \qquad (3.18a)\\
&\nabla \times \left[\exp\left(i\phi_n\left(\Omega,z\right)\right)\widehat{\boldsymbol{\mathcal{E}}}_n\left(\Omega,x,y,z\right)\right]^* \\
&= -i\Omega\mu_0\left[\widehat{\boldsymbol{\mathcal{H}}}_n\left(\Omega,x,y,z\right)\exp\left(i\phi_n\left(\Omega,z\right)\right)\right]^* \\
&\quad - \left[\exp\left(i\phi_n\left(\Omega,z\right)\right)\hat{\boldsymbol{z}}\times\frac{\partial\boldsymbol{\mathcal{E}}_n\left(\Omega,x,y,z\right)}{\partial z}\right]^* \qquad (3.18b)
\end{aligned}$$

here $\hat{\boldsymbol{z}}$ is the unit vector in the z direction. Now we can proceed to insert Eq. (3.18a) and (3.18b) into Eq. (3.17a) and (3.17b) to obtain

$$\begin{aligned}
&\mathbf{E}\cdot\Bigg(i\Omega\epsilon_0\epsilon_r\left[\exp\left(i\phi_n\left(\Omega,z\right)\right)\widehat{\boldsymbol{\mathcal{E}}}_n\right]^* \\
&- \left[\exp\left(i\phi_n\left(\Omega,z\right)\right)\widehat{\hat{\boldsymbol{z}}}\times\frac{\partial\widehat{\boldsymbol{\mathcal{H}}}_n}{\partial z}\right]^*\Bigg) \\
&- \nabla\cdot\left(\left[\exp\left(i\phi_n\left(\Omega,z\right)\right)\widehat{\boldsymbol{\mathcal{H}}}_n\right]^*\times\mathbf{E}\right) \\
&= -i\Omega\mu_0\left[\exp\left(i\phi_n\left(\Omega,z\right)\right)\widehat{\boldsymbol{\mathcal{H}}}_n\right]^*\cdot\mathbf{H}, \qquad (3.19a)\\
&\mathbf{H}\cdot\Bigg(-i\Omega\mu_0\left[\exp\left(i\phi_n\left(\Omega,z\right)\right)\widehat{\boldsymbol{\mathcal{H}}}_n\right]^* \\
&- \left[\exp\left(i\phi_n\left(\Omega,z\right)\right)\hat{\boldsymbol{z}}\times\frac{\partial\widehat{\boldsymbol{\mathcal{E}}}_n}{\partial z}\right]^*\Bigg)
\end{aligned}$$

$$
\begin{aligned}
&-\nabla\cdot\left(\left[\exp\left(i\phi_n\left(\Omega,z\right)\right)\widehat{\boldsymbol{\mathcal{E}}}_n\right]^*\times\mathbf{H}\right)\\
&=i\Omega\left[\exp\left(i\phi_n\left(\Omega,z\right)\right)\widehat{\boldsymbol{\mathcal{E}}}_n\right]^*\cdot\left(\epsilon_0\epsilon_r\mathbf{E}+\mathbf{P}_{NL}\right).
\end{aligned}
\tag{3.19b}
$$

Now we can rearrange the equations and subtract Eq. (3.19a) from Eq. (3.19b), so that only the two divergence terms are left on the left side,

$$
\begin{aligned}
&\nabla\cdot\left(\left[\exp\left(i\phi_n\left(\Omega,z\right)\right)\right]^*\left(\widehat{\boldsymbol{\mathcal{H}}}_n^*\times\mathbf{E}-\widehat{\boldsymbol{\mathcal{E}}}_n^*\times\mathbf{H}\right)\right)\\
&=-i\mu_0\Omega\left[\exp\left(i\phi_n\left(\Omega,z\right)\right)\right]^*\widehat{\boldsymbol{\mathcal{H}}}_n^*\cdot\mathbf{H} &&\leftarrow\\
&\quad+i\epsilon_r\epsilon_r\Omega\left[\exp\left(i\phi_n\left(\Omega,z\right)\right)\right]^*\widehat{\boldsymbol{\mathcal{E}}}_n^*\cdot\mathbf{E} &&\leftarrow\\
&\quad-\left[\exp\left(i\phi_n\left(\Omega,z\right)\right)\right]^*\mathbf{E}\cdot\left(\hat{\boldsymbol{z}}\times\frac{\partial\widehat{\boldsymbol{\mathcal{H}}}_n}{\partial z}\right)^*\\
&\quad-i\epsilon_r\epsilon_r\Omega\left[\exp\left(i\phi_n\left(\Omega,z\right)\right)\right]^*\widehat{\boldsymbol{\mathcal{E}}}_n^*\cdot\mathbf{E} &&\leftarrow\\
&\quad+i\mu_0\Omega\left[\exp\left(i\phi_n\left(\Omega,z\right)\right)\right]^*\widehat{\boldsymbol{\mathcal{H}}}_n^*\cdot\mathbf{H} &&\leftarrow\\
&\quad+\left[\exp\left(i\phi_n\left(\Omega,z\right)\right)\right]^*\mathbf{H}\cdot\left(\hat{\boldsymbol{z}}\times\frac{\partial\widehat{\boldsymbol{\mathcal{E}}}_n}{\partial z}\right)^*\\
&\quad-i\Omega\left[\exp\left(i\phi_n\left(\Omega,z\right)\right)\right]^*\widehat{\boldsymbol{\mathcal{E}}}_n^*\cdot\mathbf{P}_{NL}
\end{aligned}
\tag{3.20}
$$

The four terms marked in pairs with the red and blue arrows cancel and we are left with the divergence on the left hand side while there are two tapering terms and a nonlinear term on the right hand side. By integrating x and y over the whole space, minus infinity to infinity, using that the integrals are interchangeable and writing out the divergence and the shift property of a vector tripple product we get

$$
\begin{aligned}
&\int\int\frac{\partial}{\partial z}\left(\left[\exp\left(i\phi_n\left(\Omega,z\right)\right)\right]^*\hat{\boldsymbol{z}}\cdot\left(\widehat{\boldsymbol{\mathcal{H}}}_n^*\times\mathbf{E}-\widehat{\boldsymbol{\mathcal{E}}}_n^*\times\mathbf{H}\right)\right)\mathrm{d}x\mathrm{d}y\\
&+\int\int\frac{\partial}{\partial y}\left(\left[\exp\left(i\phi_n\left(\Omega,z\right)\right)\right]^*\hat{\boldsymbol{y}}\cdot\left(\widehat{\boldsymbol{\mathcal{H}}}_n^*\times\mathbf{E}-\widehat{\boldsymbol{\mathcal{E}}}_n^*\times\mathbf{H}\right)\right)\mathrm{d}y\mathrm{d}x\\
&+\int\int\frac{\partial}{\partial x}\left(\left[\exp\left(i\phi_n\left(\Omega,z\right)\right)\right]^*\hat{\boldsymbol{x}}\cdot\left(\widehat{\boldsymbol{\mathcal{H}}}_n^*\times\mathbf{E}-\widehat{\boldsymbol{\mathcal{E}}}_n^*\times\mathbf{H}\right)\right)\mathrm{d}x\mathrm{d}y\\
&+\int\int\left[\exp\left(i\phi_n\left(\Omega,z\right)\right)\right]^*\hat{\boldsymbol{z}}\cdot\left(\frac{\partial\widehat{\boldsymbol{\mathcal{H}}}_n^*}{\partial z}\times\mathbf{E}-\frac{\partial\widehat{\boldsymbol{\mathcal{E}}}_n^*}{\partial z}\times\mathbf{H}\right)\mathrm{d}x\mathrm{d}y\\
&=-i\Omega\left[\exp\left(i\phi_n\left(\Omega,z\right)\right)\right]^*\int\int\widehat{\boldsymbol{\mathcal{E}}}_n^*\cdot\mathbf{P}_{NL}\,\mathrm{d}x\mathrm{d}y
\end{aligned}
\tag{3.21}
$$

Since we must assume the fields vanish infinitely far away in both the x and y coordinates, the integration of the x and y derivatives from the divergence dissappear. We are left with only three terms in the equation, that can further be rearranged since the x and y integrals are independant of the z derivative,

$$
\frac{\partial}{\partial z}\left[\exp\left(i\phi_n\left(\Omega,z\right)\right)^*\int\int\hat{\boldsymbol{z}}\cdot\left(\widehat{\boldsymbol{\mathcal{H}}}_n^*\times\mathbf{E}-\widehat{\boldsymbol{\mathcal{E}}}_n^*\times\mathbf{H}\right)\mathrm{d}x\mathrm{d}y\right]
$$

$$+\int\int\left[\exp\left(i\phi_n\left(\Omega,z\right)\right)\right]^*\hat{\boldsymbol{z}}\cdot\left(\frac{\partial\widehat{\boldsymbol{\mathcal{H}}}_n^*}{\partial z}\times\mathbf{E}-\frac{\partial\widehat{\boldsymbol{\mathcal{E}}}_n^*}{\partial z}\times\mathbf{H}\right)\mathrm{d}x\mathrm{d}y$$
$$=-i\Omega\left[\exp\left(i\phi_n\left(\Omega,z\right)\right)\right]^*\int\int\widehat{\boldsymbol{\mathcal{E}}}_n^*\cdot\mathbf{P}_{NL}\,\mathrm{d}x\mathrm{d}y. \tag{3.22}$$

Now it is finally time to reintroduce the explicit Ω, x, y, z dependence of the fields and then insert the decomposition introduced in Eq. (3.14a) and (3.14b) on the left side of the equation. This yields, with the explicit variable dependencies now written and the sum moved outside the derivative and integrals,

$$\begin{aligned}
&\sum_m\frac{\partial}{\partial z}\Big[\left[\exp\left(i\phi_n\left(\Omega,z\right)\right)\right]^*\exp\left(i\phi_m\left(\Omega,z\right)\right)\tilde{A}_m\left(\Omega,z\right)\\
&\int\int\hat{\boldsymbol{z}}\cdot\left[\widehat{\boldsymbol{\mathcal{H}}}_n^*\left(\Omega,x,y,z\right)\times\boldsymbol{\mathcal{E}}_m\left(\Omega,x,y,z\right)-\widehat{\boldsymbol{\mathcal{E}}}_n^*\left(\Omega,x,y,z\right)\times\boldsymbol{\mathcal{H}}_m\left(\Omega,x,y,z\right)\right]\mathrm{d}x\mathrm{d}y\Big]\\
&+\sum_m\left[\exp\left(i\phi_n\left(\Omega,z\right)\right)\right]^*\exp\left(i\phi_m\left(\Omega,z\right)\right)\tilde{A}_m\left(\Omega,z\right)\\
&\int\int\hat{\boldsymbol{z}}\cdot\left[\boldsymbol{\mathcal{H}}_m\left(\Omega,x,y,z\right)\times\frac{\partial\widehat{\boldsymbol{\mathcal{E}}}_n^*\left(\Omega,x,y,z\right)}{\partial z}+\frac{\partial\widehat{\boldsymbol{\mathcal{H}}}_n^*\left(\Omega,x,y,z\right)}{\partial z}\times\boldsymbol{\mathcal{E}}_m\left(\Omega,x,y,z\right)\right]\mathrm{d}x\mathrm{d}y\\
=&-i\Omega\left[\exp\left(i\phi_n\left(\Omega,z\right)\right)\right]^*\int\int\widehat{\boldsymbol{\mathcal{E}}}_n^*\left(\Omega,x,y,z\right)\cdot\tilde{\mathbf{P}}_{NL}\left(\Omega,x,y,z\right)\,\mathrm{d}x\mathrm{d}y.
\end{aligned}\tag{3.23}$$

In order to get rid of the x and y integrals on the left side, all we need is to write up the time averaged Poynting vector for the case of a perfect guiding fiber without nonlinearities and integrate it. Since the power must be preserved in this case in a mode, the derivative must be zero. *This implies that we are dealing with a perfect world lossless fiber. In reality we will always truncate the fields at some point, so that we dont need an infinitely large calculational space (and in the physical world infinitely thick fibers!). This gives us two problems. Firstly, we are no longer guaranteed that modes form a perfect orthonormal set. Secondly, there will be loss directly related to how much of the fields of a mode extent outside the computational region and into the lossy buffer but perfectly matched layer (PML) that is usually applied numerically. This is true for normal step index fibers with exact mathematical solutions, but even more so for microstructured fibers, where the fields do not decay to zero outside the microstructure, that are investigated by for instance the Finite Element Method and other such numerical methods. The first problem is solved by assuming the changes in the transverse integrals due to truncation are small compared to the true eigenmodes. This means we can use the eigenmodes found by numerical means directly. The second problem is not really a problem, as we can introduce loss directly by allowing $\phi_n\left(\Omega,z\right)$ to be complex. Hence why the complex conjugate was kept on the phase term in all the above calculations.*

In order to get a better understanding of what the transverse integral on the left side is, and how to deal with it, let us take a small but worthwhile detour and write down the

cycle averaged Poyting vector in the frequency domain,

$$\begin{aligned}\left\langle \tilde{\boldsymbol{S}}\left(\Omega,z,y,z\right)\right\rangle &= \frac{1}{2}\mathrm{Re}\left[\mathbf{E}\left(\Omega,x,y,z\right)\times\mathbf{H}^{*}\left(\Omega,x,y,z\right)\right]\\ &= \frac{1}{4}\left(\mathbf{E}\left(\Omega,x,y,z\right)\times\mathbf{H}^{*}\left(\Omega,x,y,z\right)+\mathbf{E}^{*}\left(\Omega,x,y,z\right)\times\mathbf{H}\left(\Omega,x,y,z\right)\right)\end{aligned} \tag{3.24}$$

Since the cycle averaged Poynting vector is the intensity of the field at a given frequency, we can now calculate the power transported along the fiber at any given z coordinate. If we require that the power, P, is conserved, the derivative must be zero. Inserting the definition of the fields from Eq. (3.13a) and (3.13b), we get

$$\begin{aligned}0 &= \frac{\partial\tilde{P}\left(\Omega,z\right)}{\partial z} = \frac{\partial}{\partial z}\int\int\left\langle\tilde{\boldsymbol{S}}\right\rangle\cdot\hat{\boldsymbol{z}}\,\mathrm{d}x\mathrm{d}y\\ &= \frac{1}{4}\sum_{m,n}\tilde{A}_{m}\left(\Omega,z\right)\tilde{A}_{n}^{*}\left(\Omega,z\right)i\left(\beta_{m}\left(\Omega,z\right)-\beta_{n}\left(\Omega,z\right)\right)\exp\left(i\phi_{m}\left(\Omega,z\right)-i\phi_{n}\left(\Omega,z\right)\right)\\ &\int\int\left[\boldsymbol{\mathcal{E}}_{m}\left(\Omega,x,y\right)\times\boldsymbol{\mathcal{H}}_{n}^{*}\left(\Omega,x,y\right)+\boldsymbol{\mathcal{E}}_{n}^{*}\left(\Omega,x,y\right)\times\boldsymbol{\mathcal{H}}_{m}\left(\Omega,x,y\right)\right]\cdot\hat{\boldsymbol{z}}\,\mathrm{d}x\mathrm{d}y\end{aligned} \tag{3.25}$$

When β is the same for two modes, either by $m=n$, by design or a non bifringent fiber (when it is two polarizations of the same mode), the integrals can give anything, as the expression is still zero, giving power conservation of each mode. When this is not the case, $m\neq n$, the x,y integrals have to be zero to ensure that the power is conserved. We also know that we can decouple the fields completely in the degenerate case (same β for different m and n), so even in this case the integrals must give zero. The above arguments also work for adiabatic fiber tapers, as the power is conserved in a mode. In the case where $m=n$, we get a value, which we will call $N_{n}\left(\Omega,z\right)$, and also use as the normalization introduced earlier. This gives

$$\begin{aligned}&\int\int\left[\boldsymbol{\mathcal{H}}_{n}^{*}\left(\Omega,x,y,z\right)\times\boldsymbol{\mathcal{E}}_{m}\left(\Omega,x,y,z\right)-\boldsymbol{\mathcal{E}}_{n}^{*}\left(\Omega,x,y,z\right)\times\boldsymbol{\mathcal{H}}_{m}\left(\Omega,x,y,z\right)\right]\cdot\hat{\boldsymbol{z}}\,\mathrm{d}x\mathrm{d}y\\ &= -4\delta_{nm}N_{n}^{2}\left(\Omega,z\right),\end{aligned} \tag{3.26}$$

Why did we make this exact, seemingly arbitrary, choice for normalization? To answer that, let us write up the integral of the Poynting vector again for the completely general case, and then rewrite it with the normalization on the transverse fields,

$$\begin{aligned}\tilde{P}\left(\Omega,z\right) &= \int\int\tilde{\mathbf{S}}\left(\Omega,z,y,z\right)\cdot\hat{\boldsymbol{z}}\,\mathrm{d}x\mathrm{d}y\\ &= \frac{1}{4}\sum_{m,n}\tilde{A}_{m}\left(\Omega,z\right)\tilde{A}_{n}^{*}\left(\Omega,z\right)\exp\left(i\phi_{m}\left(\Omega,z\right)\right)\left[\exp\left(i\phi_{n}\left(\Omega,z\right)\right)\right]^{*}\\ &\quad\int\int\left[\boldsymbol{\mathcal{E}}_{m}\left(\Omega,x,y\right)\times\boldsymbol{\mathcal{H}}_{n}^{*}\left(\Omega,x,y\right)+\boldsymbol{\mathcal{E}}_{n}^{*}\left(\Omega,x,y\right)\times\boldsymbol{\mathcal{H}}_{m}\left(\Omega,x,y\right)\right]\cdot\hat{\boldsymbol{z}}\,\mathrm{d}x\mathrm{d}y\\ &= \frac{1}{4}\sum_{m,n}\tilde{A}_{m}\left(\Omega,z\right)\tilde{A}_{n}^{*}\left(\Omega,z\right)\,4\,\delta_{nm}\,N_{n}^{2}\left(\Omega,z\right)\exp\left(i\phi_{m}\left(\Omega,z\right)\right)\left[\exp\left(i\phi_{n}\left(\Omega,z\right)\right)\right]^{*}\end{aligned}$$

$$
\begin{aligned}
&= \sum_n \left| \tilde{A}_n (\Omega, z) \right|^2 N_n^2 (\Omega, z) \\
&= \sum_n \left| \tilde{\mathcal{A}}_n (\Omega, z) \right|^2
\end{aligned} \tag{3.27}
$$

where

$$
\tilde{\mathcal{A}}_n (\Omega, z) = N_n (\Omega, z) \, \tilde{A}_n (\Omega, z) \tag{3.28}
$$

In other words, if we normalize the transverse $\boldsymbol{\mathcal{E}}_n$ and $\boldsymbol{\mathcal{H}}_n$ fields so that $N_n (\Omega, z) = 1$, for all z and Ω, under the assumption of no loss ($\phi_n (\Omega, z) = \phi_n (\Omega, z)^*$), then $|A_n (\Omega, z)|^2$ is directly the power carried in mode n. In fact, the assumption of no loss is overkill here, as a complex phase would just add the normal known exponential loss factor, $\exp(-2 \operatorname{Im}(\phi_m (\Omega, z)))$. It also conveniently happens that one of the integrals in Eq. (3.23) is brought to its most simple form - it dissappears entirely.

The other part of Eq. 3.23, the part with the derivatives, is now easy to deal with when the indices are the same, since we can then use the chain rule inversely and our definition of $N_n (\Omega, z)$. This gives,

$$
\begin{aligned}
&\int\int \hat{\boldsymbol{z}} \cdot \left[\boldsymbol{\mathcal{H}}_m (\Omega, x, y, z) \times \frac{\partial \boldsymbol{\mathcal{E}}_m^* (\Omega, x, y, z)}{\partial z} + \frac{\partial \boldsymbol{\mathcal{H}}_m^* (\Omega, x, y, z)}{\partial z} \times \boldsymbol{\mathcal{E}}_m (\Omega, x, y, z) \right] \mathrm{d}x\mathrm{d}y \\
=&\frac{\partial N_n (\Omega, z)}{\partial z} = 0.
\end{aligned} \tag{3.29}
$$

How will this interlude affect our derivation? First of all, we need to get the left hand side integrals in Eq. (3.23) to the form in Eq. (3.26), by writing out the scalar $N_n (\Omega, z)$ from the fields (drawing out the normalization by using Eq. (3.15)) and then sum out the delta function to get

$$
\begin{aligned}
&- 4 \frac{\partial}{\partial z} \Big[\left[\exp (i \phi_n (\Omega, z)) \right]^* \exp (i \phi_n (\Omega, z)) \, \tilde{A}_n (\Omega, z) \, N_n (\Omega, z) \Big] \\
&+ \sum_{m \neq n} \left[\exp (i \phi_n (\Omega, z)) \right]^* \exp (i \phi_m (\Omega, z)) \, \tilde{A}_m (\Omega, z) \, N_m (\Omega, z) \\
&\int\int \hat{\boldsymbol{z}} \cdot \left[\boldsymbol{\mathcal{H}}_m (\Omega, x, y, z) \times \frac{\partial \widehat{\boldsymbol{\mathcal{E}}}_n^* (\Omega, x, y, z)}{\partial z} + \frac{\partial \widehat{\boldsymbol{\mathcal{H}}}_n^* (\Omega, x, y, z)}{\partial z} \times \boldsymbol{\mathcal{E}}_m (\Omega, x, y, z) \right] \mathrm{d}x\mathrm{d}y \\
=& - i\Omega \left[\exp (i \phi_n (\Omega, z)) \right]^* \int\int \widehat{\boldsymbol{\mathcal{E}}}_n^* (\Omega, x, y, z) \cdot \tilde{\mathbf{P}}_{NL} (\Omega, x, y, z) \, \mathrm{d}x\mathrm{d}y.
\end{aligned} \tag{3.30}
$$

The following arguments match those made by Laegsgaard [40]. The $m \neq n$ sum here describes taper induced coupling between the different modes. This includes radiation modes, and it should be obvious that this sum can be quite cumbersome. However, losses to these radiation modes can typically be incorporated with z dependant imaginary parts, either by measurements or by educated guesses. *In this case we might be able to disregard the sum entirely. This is due to the approximation that the oscillating nature of the phase terms would kill off any contributions in the sum, except in the case of phase matching, at*

specific frequencies. However since the phase matching condition changes continously with the taper, there will only be short lengths with phase matching for any given frequency and mode. Therefore the sum term can, in most cases, be neglected. It might be possible to design a taper where phase matching occurs throughout the taper, in which case the sum can not be neglected. Even if the sum has to be considered, it is possible to disregard terms due to symmetries and polarization states. From here it is easy to perform the last step in order to get the general equation for the envelope $\tilde{A}_m(\Omega, z)$ given by the electric field and the nonlinear induced polarization,

$$\begin{aligned}&\frac{\partial}{\partial z}\Big[\exp\left(-2\,\mathrm{Im}\left(\phi_n(\Omega,z)\right)\right)\tilde{A}_n(\Omega,z)\,N_n(\Omega,z)\Big]\\ =&i\frac{\Omega}{4}\left[\exp\left(i\phi_n(\Omega,z)\right)\right]^*\int\int\widehat{\boldsymbol{\mathcal{E}}}_n^*(\Omega,x,y,z)\cdot\tilde{\mathbf{P}}_{NL}(\Omega,x,y,z)\,\mathrm{d}x\mathrm{d}y.\end{aligned}\tag{3.31}$$

Before going into the induced nonlinear polarization, let me comment on the normalisation now present in the equation, and the apparent lack thereof in $\tilde{\mathbf{P}}_{NL}(\Omega, x, y, z)$. Later, it will be used to redefine $A_m(\Omega, z)$ and $\boldsymbol{\mathcal{E}}_m(\Omega, z)$ by the definition in Eq. (3.28) so that each of the three $\boldsymbol{\mathcal{E}}_{\boldsymbol{m}}(\Omega, z)$ inside $\tilde{\mathbf{P}}_{NL}(\Omega, x, y, z)$ transfers a $N_m(\Omega, z)$ (unit of $\sqrt{\mathrm{W}}$) into the unitless envelope, $A_m(\Omega, z)$. The square of the new $A_m(\Omega, z)$ is thus truly an expression of optical power in a given mode, as seen in Eq. (3.27). As it stands in the above equation, the nonlinear polarization is unchanged by this as there is an equal number of envelopes ($A_m(\Omega, z)$'s) in need of $N_m(\Omega, z)$ and unnormalized transverse fields ($\boldsymbol{\mathcal{E}}_m(\Omega, z)$'s) to supply $N_m(\Omega, z)$. The introduction of the normalisation early on means that we now have the missing terms to make the transformation complete and in the end write the GNLSE in terms of the power variable $\tilde{\mathcal{A}}(\Omega, z)$.

3.2 The Induced Nonlinear Polarization

Now that we have arrived at a solvable expression on the left side, it is time to take a close look on the right side of the expression in Eq. (3.31). Namely, it is time to look at the elephant in the room, the induced nonlinear polarization. Continuing the textbook approach we started when we drew out the first order response, we can write it as a power expansion in the remaining, higher order, powers of the electric field,

$$\mathbf{P}_{NL}(t,x,y,z)=\mathbf{P}_{NL}^{(2)}(t,x,y,z)+\mathbf{P}_{NL}^{(3)}(t,x,y,z)+\mathbf{P}_{NL}^{(4)}(t,x,y,z)\ldots\tag{3.32}$$

where the strength of each order falls with increasing order number. It can be shown using a quantum mechanical approach that the third order induced polarization has to take on a specific form, as done by for instance Hellwarth [26]. The third order induced polarization can in general be written as a single time convolution of a response tensor, that depends on time. Since we are already relying on the fact that the induced non linear polarization is much smaller than the electric field, we should in most cases truncate the expansion after the first term higher order term. However usually one keeps both second and third order terms as the third order term has a delayed response (unlike the second order term),

which makes it fundamentally different, and might be of interest for very high power. This means we can write the induced polarization as

$$\mathbf{P}_{NL}^{(2)}(t,x,y,z) = \epsilon_0 \chi^{(2)} : \mathbf{E}(t,x,y,z)\,\mathbf{E}(t,x,y,z) \tag{3.33}$$

$$\mathbf{P}_{NL}^{(3)}(t,x,y,z) = \epsilon_0 \int \chi^{(3)}(t-t_1) \vdots \mathbf{E}(t_1,x,y,z)\,\mathbf{E}(t_1,x,y,z)\,\mathbf{E}(t,x,y,z)\,\mathrm{d}t_1. \tag{3.34}$$

Note how the double and tripple dot denotes a tensor product. *We can assume the second order induced polarization is zero, by limiting ourselves to isotropic (silica glass) fibers, which due to their inherent random crystal and molecular orientation are spatially symmetric. This only works if the fibers are not treated to break the symmetry by for instance electric fields. Furthermore, by working with isotropic materials, the remaining third order tensor will be reduced enormously in complexity due to symmetry considerations. Therefore the following expressions and derivations are not valid for anisotropic materials such as silicium waveguides, which have an orderly crystal structure. That said, it is rather straightforward to include the second order term in* $\mathbf{P}_{NL}(t,x,y,z)$*, and it would not impact the third order term and how we treat it, except by changing the symmetries of the tensor.* The response tensor, $\chi^{(3)}(t-t_1)$, can be written as done by for instance Agrawal [2, eq. 8.5.3], for isotropic materials like amorphous silica glass, using Einstein index notation in cartesian coordinates. It is straightforward to show that the indices do not have to be cartesian coordinates, but can also be fiber modes, in which case,

$$\begin{aligned}
\chi_{mnpq}^{(3)}(t) = \chi \Big[& \frac{1}{3}(1-f_a-f_b)\,\delta(t)\left(\delta_{mn}\delta_{pq}+\delta_{mp}\delta_{nq}+\delta_{mq}\delta_{np}\right) && \Big\} \text{SPM} + \text{XPM} + \text{Deg. FWM} \\
& + f_a h_a(t)\,\delta_{mn}\delta_{pq} && \Big\} \text{Raman} \\
& + \frac{1}{2} f_b h_b(t)\left(\delta_{mp}\delta_{nq}+\delta_{mq}\delta_{np}\right) \Big] && \Big\} \text{Cross} - \text{Raman}.
\end{aligned} \tag{3.35}$$

Often it has been used that, $h_b(t) << h_a(t)$ and its contribution has thus been neglected, as done for instance by Laegsgaard, [40]. Here it will be included as it might have an important effect in the inherent unstable and polarization dependent behaviour of supercontinuum generation. The response function, $h_a(t)$ has been thoroughly studied for silica, and several approximated analytical expressions exist, [2, 17, 26, 44, 75]. Likewise the response function $h_b(t)$ has been measured for silica and is shown in [2]. In the following the full numerical values will be used, unless otherwise stated. There is no gain by using an approximate analytic expression as the numerical solver would have to evaluate this expression at specific points anyway. Values for χ can be found in the review article by [49] or in chapter 11 in [2]. The latter also has a good discussion and explanation of the different reported values. Returning to the expression in Eq. (3.34), it is time to insert the general expression for the electric field from Eq. (3.13a), while remembering that the sum also includes polarization states. Also since the fields are real in time, they must be hermitian in frequency. Thus we can complex conjugate all fields for p'th mode. The integrals and sums for the three individual fields can be expanded to include the other

two fields, which means we end up with

$$\begin{aligned}\mathbf{P}_{NL}(t,x,y,z) = \frac{\epsilon_0}{(2\pi)^3}\sum_{n,p,q}\int\int\int\int \\ \tilde{A}_n(\Omega_1,z)\,\tilde{A}_p(\Omega_2,z)\,\tilde{A}_q(\Omega_3,z) \\ \exp\left(i\phi_n(\Omega_1,z)+i\Omega_1 t\right)\exp\left(i\phi_p(\Omega_2,z)+i\Omega_2 t_1\right)\exp\left(i\phi_q(\Omega_3,z)+i\Omega_3 t_1\right) \\ \left[\chi^{(3)}(t-t_1)\vdots\boldsymbol{\mathcal{E}}_n(\Omega_1,x,y,z)\,\boldsymbol{\mathcal{E}}_p(\Omega_2,x,y,z)\,\boldsymbol{\mathcal{E}}_q(\Omega_3,x,y,z)\right]\mathrm{d}t_1\mathrm{d}\Omega_1\mathrm{d}\Omega_2\mathrm{d}\Omega_3. \quad (3.36)\end{aligned}$$

Taking the Fourier transform on both sides in order to get to $\tilde{\mathbf{P}}_{NL}(\Omega,x,y,z)$ and by using the inverse Fourier transform of the response function we get,

$$\begin{aligned}\tilde{\mathbf{P}}_{NL}(\Omega,x,y,z) = \frac{\epsilon_0}{(2\pi)^4}\sum_{n,p,q}\int\int\int\int\int\int \\ \exp\left(i\phi_n(\Omega_1,z)+i\Omega_1 t\right)\exp\left(i\phi_p(\Omega_2,z)+i\Omega_2 t_1\right)\exp\left(i\phi_q(\Omega_3,z)+i\Omega_3 t_1\right) \\ \exp\left(i\Omega_4 t - i\Omega_4 t_1\right)\exp\left(-i\Omega t\right)\tilde{A}_n(\Omega_1,z)\,\tilde{A}_p(\Omega_2,z)\,\tilde{A}_q(\Omega_3,z) \\ \left[\tilde{\chi}^{(3)}(\Omega_4)\vdots\boldsymbol{\mathcal{E}}_n(\Omega_1,x,y,z)\,\boldsymbol{\mathcal{E}}_p(\Omega_2,x,y,z)\,\boldsymbol{\mathcal{E}}_q(\Omega_3,x,y,z)\right]\mathrm{d}t_1\mathrm{d}t\mathrm{d}\Omega_1\mathrm{d}\Omega_2\mathrm{d}\Omega_3\mathrm{d}\Omega_4. \quad (3.37)\end{aligned}$$

In this expression it is possible to collect exponential terms of both t and t_1, which can then be combined with the t and t_1 integrals to yield two delta functions according to the definition in Eq. (3.3),

$$\begin{aligned}\tilde{\mathbf{P}}_{NL}(\Omega,x,y,z) = \frac{\epsilon_0}{(2\pi)^2}\sum_{n,p,q}\int\int\int\int\delta(\Omega_4+\Omega_1-\Omega)\,\delta(\Omega_3+\Omega_2-\Omega_4) \\ \exp\left(i\phi_n(\Omega_1,z)\right)\exp\left(i\phi_p(\Omega_2,z)\right)\exp\left(i\phi_q(\Omega_3,z)\right) \\ \tilde{A}_n(\Omega_1,z)\,\tilde{A}_p(\Omega_2,z)\,\tilde{A}_q(\Omega_3,z) \\ \left[\tilde{\chi}^{(3)}(\Omega_4)\vdots\boldsymbol{\mathcal{E}}_n(\Omega_1,x,y,z)\,\boldsymbol{\mathcal{E}}_p(\Omega_2,x,y,z)\,\boldsymbol{\mathcal{E}}_q(\Omega_3,x,y,z)\right]\mathrm{d}\Omega_1\mathrm{d}\Omega_2\mathrm{d}\Omega_3\mathrm{d}\Omega_4. \quad (3.38)\end{aligned}$$

Now we can perform the Ω_2 and Ω_4 integrals in order to arrive at

$$\begin{aligned}\tilde{\mathbf{P}}_{NL}(\Omega,x,y,z) = \frac{\epsilon_0}{(2\pi)^2}\sum_{n,p,q}\int\int \\ \exp\left(i\phi_n(\Omega_1,z)\right)\exp\left(i\phi_p(\Omega-\Omega_1-\Omega_3,z)\right)\exp\left(i\phi_q(\Omega_3,z)\right) \\ \tilde{A}_n(\Omega_1,z)\,\tilde{A}_p(\Omega-\Omega_1-\Omega_3,z)\,\tilde{A}_q(\Omega_3,z) \\ \left[\tilde{\chi}^{(3)}(\Omega-\Omega_1)\vdots\boldsymbol{\mathcal{E}}_n(\Omega_1,x,y,z)\,\boldsymbol{\mathcal{E}}_p(\Omega-\Omega_1-\Omega_3,x,y,z)\,\boldsymbol{\mathcal{E}}_q(\Omega_3,x,y,z)\right]\mathrm{d}\Omega_1\mathrm{d}\Omega_3. \quad (3.39)\end{aligned}$$

This can be inserted into Eq. (3.31) and three different normalisation fractions can be drawn out of an implicit 1, in order to prepare for the normalisation variable change from

Eq. (3.28),

$$\begin{aligned}
&\frac{\partial}{\partial z}\left[\exp\left(-2\,\mathrm{Im}\left(\phi_m\left(\Omega,z\right)\right)\right)N_m\left(\Omega,z\right)\tilde{A}_m\left(\Omega,z\right)\right]\\
&=i\Omega\frac{\epsilon_0}{4\left(2\pi\right)^2}\left[\exp\left(i\phi_m\left(\Omega,z\right)\right)\right]^*\sum_{n,p,q}\int\int\\
&\int\int\Big[\frac{\boldsymbol{\mathcal{E}}_m^*\left(\Omega,x,y,z\right)}{N_m\left(\Omega,z\right)}\cdot\tilde{\chi}^{(3)}\left(\Omega-\Omega_1\right)\vdots\frac{\boldsymbol{\mathcal{E}}_n\left(\Omega_1,x,y,z\right)}{N_n\left(\Omega_1,z\right)}\frac{\boldsymbol{\mathcal{E}}_p\left(\Omega-\Omega_1-\Omega_3,x,y,z\right)}{N_p\left(\Omega-\Omega_1-\Omega_3,z\right)}\frac{\boldsymbol{\mathcal{E}}_q\left(\Omega_3,x,y,z\right)}{N_q\left(\Omega_3,z\right)}\Big]\,\mathrm{d}x\mathrm{d}y\\
&\exp\left(i\phi_n\left(\Omega_1,z\right)\right)\exp\left(i\phi_p\left(\Omega-\Omega_1-\Omega_3,z\right)\right)\exp\left(i\phi_q\left(\Omega_3,z\right)\right)\\
&N_n\left(\Omega_1,z\right)\tilde{A}_n\left(\Omega_1,z\right)N_p\left(\Omega-\Omega_1-\Omega_3,z\right)\tilde{A}_p\left(\Omega-\Omega_1-\Omega_3,z\right)N_q\left(\Omega_3,z\right)\tilde{A}_q\left(\Omega_3,z\right)\,\mathrm{d}\Omega_1\mathrm{d}\Omega_3.
\end{aligned}\tag{3.40}$$

From here all we need to do to get to the known version of the GNLSE is to introduce the variable change briefly discussed earlier in Eq. (3.28) and (3.15). Reiterating, $\left|\tilde{\mathcal{A}}_n\left(\Omega,z\right)\right|^2$ is the Poyinting vector integrated over x,y, as seen in Eq. (3.27), and thus gives the instantaneous power in the mode. This change of variables yields the completely generalized non linear Schrödinger equation,

$$\begin{aligned}
&\frac{\partial}{\partial z}\left[\exp\left(-2\,\mathrm{Im}\left(\phi_m\left(\Omega,z\right)\right)\right)\tilde{\mathcal{A}}_m\left(\Omega,z\right)\right]=\\
&i\Omega\frac{\epsilon_0}{4\left(2\pi\right)^2}\left[\exp\left(i\phi_m\left(\Omega,z\right)\right)\right]^*\sum_{n,p,q}\int\int\tilde{\chi}^{(3)}_{mnpq}\left(\Omega-\Omega_1\right)\\
&\int\int\Big[\widehat{\boldsymbol{\mathcal{E}}}_m^*\left(\Omega,x,y,z\right)\cdot\widehat{\boldsymbol{\mathcal{E}}}_n\left(\Omega_1,x,y,z\right)\widehat{\boldsymbol{\mathcal{E}}}_p\left(\Omega-\Omega_1-\Omega_3,x,y,z\right)\cdot\widehat{\boldsymbol{\mathcal{E}}}_q\left(\Omega_3,x,y,z\right)\Big]\,\mathrm{d}x\mathrm{d}y\\
&\exp\left(i\phi_n\left(\Omega_1,z\right)\right)\exp\left(i\phi_p\left(\Omega-\Omega_1-\Omega_3,z\right)\right)\exp\left(i\phi_q\left(\Omega_3,z\right)\right)\\
&\tilde{\mathcal{A}}_n\left(\Omega_1,z\right)\tilde{\mathcal{A}}_p\left(\Omega-\Omega_1-\Omega_3,z\right)\tilde{\mathcal{A}}_q\left(\Omega_3,z\right)\,\mathrm{d}\Omega_1\mathrm{d}\Omega_3.
\end{aligned}\tag{3.41}$$

This equation not only includes mode profile dispersion and tapering in multimode fibers, it also includes different polarization states (in the mode sums), including the effects of bifringence. It can be shown that it conserves the photon number. Let us finish this section by checking the units of the equation. $\tilde{A}\left(\Omega,z\right)$ is s (unitless in time domain), $N\left(\Omega,z\right)$ has the unit $\sqrt{\mathrm{W}}$, $\mathcal{E}\left(\Omega,x,y,z\right)$ has the unit $\mathrm{V\,m^{-1}}$, χ has the unit $\mathrm{m^2\,V^{-2}}$, Ω has the unit $\mathrm{s^{-1}}$ and lastly ϵ_0 has unit $\mathrm{A^2\,W^{-1}\,s\,m^{-1}}$. The integrals yield $\mathrm{m^2}$ and $\mathrm{s^{-2}}$ while the z derivative yields $\mathrm{m^{-1}}$. Combined this gives the unit equation,

$$\frac{\sqrt{\mathrm{W}}\,\mathrm{s}}{\mathrm{m}}=\frac{\mathrm{s^3A^2\,s\,m^2\,V^4\,m^2}}{\mathrm{s\,W\,m\,s^2}\,\sqrt{\mathrm{W}}\mathrm{m^4V^2}}=\frac{\mathrm{W^2}}{\mathrm{W^{3/2}}}\frac{\mathrm{m^4}}{\mathrm{m^5}}\frac{\mathrm{s^4}}{\mathrm{s^3}}=\frac{\sqrt{\mathrm{W}}\,\mathrm{s}}{\mathrm{m}},\tag{3.42}$$

and since it checks out, and the envelope now has the correct units, we are done.

As a final note, it is prudent to address a very important question, which the curiously observant reader might be wondering about. What happens to the induced nonlinearity if we are dealing with multi material fibers? At a glance, it seems like the equation cannot

handle multi glass fibers, or more relevant for this thesis, holey fibers. But actually they can be quite easily included as the transverse integrals can be expanded into a sum of transverse integrals each covering a single material with a corresponding nonlinear response function. For example, for silica photonic crystal fibers, this means that the transverse integrals are not from minus infinity to infinity, but are instead only over the region with silica glass.

3.3 The envelope equation

While the expression derived in the previous section is generally applicable, it is far more convenient to work with an envelope equation. In this short section, we will change the equation to an envelope equation, by using a well known mathematical trick. Since we know that the electric field in Eq. (3.41) is real in time, we know that the electric field in the frequency domain, Eq. (3.14a), is hermitian:

$$\tilde{\boldsymbol{E}}(\Omega, x, y, z) = \tilde{\boldsymbol{E}}^*(-\Omega, x, y, z). \tag{3.43}$$

or

$$\begin{aligned} &\sum_m \tilde{\mathcal{A}}_m(\Omega, z)\, \widehat{\boldsymbol{\mathcal{E}}}_m(\Omega, x, y, z) \exp\left(i\phi_m(\Omega, z)\right) \\ =&\sum_m \tilde{\mathcal{A}}_m(\Omega, z)\, \widehat{\boldsymbol{\mathcal{E}}}_m(\Omega, x, y, z) \exp\left(i\phi_m(\Omega, z)\right). \end{aligned} \tag{3.44}$$

From here we can argue that each term in the sum corresponding to each mode must fulfill the equation, so that the equation must be true for each term individually and further each of the three products in the equation should be the same, as they are all individual functions of frequency. This yields the well known properties

$$\tilde{\mathcal{A}}_m(\Omega, z) = \tilde{\mathcal{A}}_m^*(-\Omega, z) \tag{3.45}$$

$$\widehat{\boldsymbol{\mathcal{E}}}_m(\Omega, x, y, z) = \widehat{\boldsymbol{\mathcal{E}}}_m^*(-\Omega, x, y, z) \tag{3.46}$$

$$\phi_m(\Omega, z) = -\phi_m^*(-\Omega, z) \tag{3.47}$$

$$\mathrm{Im}\left(\phi_m(\Omega, z)\right) = \mathrm{Im}\left(\phi_m(-\Omega, z)\right) \tag{3.48}$$

$$\mathrm{Re}\left(\phi_m(\Omega, z)\right) = -\mathrm{Re}\left(\phi_m(-\Omega, z)\right) \tag{3.49}$$

It is straightforward to split $\tilde{\mathcal{A}}_m(\Omega, z)$ in two equal parts, and use the above property on the second term to write

$$\tilde{\mathcal{A}}_m(\Omega, z) = \frac{1}{2}\tilde{\mathcal{A}}_m(\Omega, z) + \frac{1}{2}\tilde{\mathcal{A}}_m^*(-\Omega, z) \tag{3.50}$$

and likewise with each mode of the full electric field in the frequency domain

$$\tilde{\mathcal{A}}_m(\Omega, z)\, \widehat{\boldsymbol{\mathcal{E}}}_m(\Omega, x, y, z) \exp\left(i\phi_m(\Omega, z)\right)$$

$$= \frac{1}{2}\tilde{\mathcal{A}}_m(\Omega,z)\,\widehat{\boldsymbol{\mathcal{E}}}_m(\Omega,x,y,z)\exp\left(i\phi_m(\Omega,z)\right)$$
$$+ \frac{1}{2}\tilde{\mathcal{A}}^*_m(-\Omega,z)\,\widehat{\boldsymbol{\mathcal{E}}}^*_m(-\Omega,x,y,z)\exp\left(-i\phi^*_m(-\Omega,z)\right). \tag{3.51}$$

The choice of expanding $\tilde{\mathcal{A}}_m(\Omega,z)$ on the left side, while expanding the product of all three terms together on the right side is for convenience in generating a symmetric equation. It is equally valid to any other choice, but this choice makes it straightforward to split the equation in two equations and show that a solution to one, also guarantees a solution to the other, and hence a solution to the overall equation. It sounds confusing, but mathematically it is quite beautiful, especially if one uses colors to keep track of what goes where. Inserting into Eq. (3.41), rearranging the fractions, writing out the products and using Eq. (3.45)-(3.50) we get the following

$$\frac{\partial}{\partial z}\left[\exp\left(-2\,\mathrm{Im}\left(\phi_m(\Omega,z)\right)\right)\tilde{\mathcal{A}}_m(\Omega,z) + \exp\left(-2\,\mathrm{Im}\left(\phi_m(-\Omega,z)\right)\right)\tilde{\mathcal{A}}^*_m(-\Omega,z)\right] =$$
$$\frac{1}{4}i\Omega\frac{\epsilon_0}{4(2\pi)^2}\left[\exp\left(i\phi_m(\Omega,z)\right)\right]^*\sum_{n,p,q}\int\int\tilde{\chi}^{(3)}_{mnpq}(\Omega-\Omega_1)$$
$$\int\int\left[\widehat{\boldsymbol{\mathcal{E}}}^*_m(\Omega,x,y,z)\cdot\widehat{\boldsymbol{\mathcal{E}}}_n(\Omega_1,x,y,z)\,\widehat{\boldsymbol{\mathcal{E}}}_p(\Omega-\Omega_1-\Omega_3,x,y,z)\cdot\widehat{\boldsymbol{\mathcal{E}}}_q(\Omega_3,x,y,z)\right]\mathrm{d}x\mathrm{d}y$$
$$\exp\left(i\phi_n(\Omega_1,z)\right)\exp\left(i\phi_p(\Omega-\Omega_1-\Omega_3,z)\right)\exp\left(i\phi_q(\Omega_3,z)\right)$$
$$\tilde{\mathcal{A}}_n(\Omega_1,z)\,\tilde{\mathcal{A}}_p(\Omega-\Omega_1-\Omega_3,z)\,\tilde{\mathcal{A}}_q(\Omega_3,z)\;\mathrm{d}\Omega_1\mathrm{d}\Omega_3$$
$$+\frac{1}{4}i\Omega\frac{\epsilon_0}{4(2\pi)^2}\left[\exp\left(i\phi_m(\Omega,z)\right)\right]^*\sum_{n,p,q}\int\int\tilde{\chi}^{(3)}_{mnpq}(\Omega-\Omega_1)$$
$$\int\int\left[\widehat{\boldsymbol{\mathcal{E}}}^*_m(\Omega,x,y,z)\cdot\widehat{\boldsymbol{\mathcal{E}}}^*_n(-\Omega_1,x,y,z)\,\widehat{\boldsymbol{\mathcal{E}}}^*_p(-\Omega+\Omega_1+\Omega_3,x,y,z)\cdot\widehat{\boldsymbol{\mathcal{E}}}^*_q(-\Omega_3,x,y,z)\right]\mathrm{d}x\mathrm{d}y$$
$$\exp\left(-i\phi^*_n(-\Omega_1,z)\right)\exp\left(-i\phi^*_p(-\Omega+\Omega_1+\Omega_3,z)\right)\exp\left(-i\phi^*_q(-\Omega_3,z)\right)$$
$$\tilde{\mathcal{A}}^*_n(-\Omega_1,z)\,\tilde{\mathcal{A}}^*_p(-\Omega+\Omega_1+\Omega_3,z)\,\tilde{\mathcal{A}}^*_q(-\Omega_3,z)\;\mathrm{d}\Omega_1\mathrm{d}\Omega_3$$
$$+\frac{1}{4}i\Omega\frac{\epsilon_0}{4(2\pi)^2}\left[\exp\left(i\phi_m(\Omega,z)\right)\right]^*\sum_{n,p,q}\int\int\tilde{\chi}^{(3)}_{mnpq}(\Omega-\Omega_1)$$
$$\int\int\left[\widehat{\boldsymbol{\mathcal{E}}}^*_m(\Omega,x,y,z)\cdot\widehat{\boldsymbol{\mathcal{E}}}^*_n(-\Omega_1,x,y,z)\,\widehat{\boldsymbol{\mathcal{E}}}_p(\Omega-\Omega_1-\Omega_3,x,y,z)\cdot\widehat{\boldsymbol{\mathcal{E}}}_q(\Omega_3,x,y,z)\right]\mathrm{d}x\mathrm{d}y$$
$$\exp\left(-i\phi^*_n(-\Omega_1,z)\right)\exp\left(i\phi_p(\Omega-\Omega_1-\Omega_3,z)\right)\exp\left(i\phi_q(\Omega_3,z)\right)$$
$$\tilde{\mathcal{A}}^*_n(-\Omega_1,z)\,\tilde{\mathcal{A}}_p(\Omega-\Omega_1-\Omega_3,z)\,\tilde{\mathcal{A}}_q(\Omega_3,z)\;\mathrm{d}\Omega_1\mathrm{d}\Omega_3$$
$$+\frac{1}{4}i\Omega\frac{\epsilon_0}{4(2\pi)^2}\left[\exp\left(i\phi_m(\Omega,z)\right)\right]^*\sum_{n,p,q}\int\int\tilde{\chi}^{(3)}_{mnpq}(\Omega-\Omega_1)$$
$$\int\int\left[\widehat{\boldsymbol{\mathcal{E}}}^*_m(\Omega,x,y,z)\cdot\widehat{\boldsymbol{\mathcal{E}}}_n(\Omega_1,x,y,z)\,\widehat{\boldsymbol{\mathcal{E}}}^*_p(-\Omega+\Omega_1+\Omega_3,x,y,z)\cdot\widehat{\boldsymbol{\mathcal{E}}}^*_q(-\Omega_3,x,y,z)\right]\mathrm{d}x\mathrm{d}y$$
$$\exp\left(i\phi_n(\Omega_1,z)\right)\exp\left(-i\phi^*_p(-\Omega+\Omega_1+\Omega_3,z)\right)\exp\left(-i\phi^*_q(-\Omega_3,z)\right)$$
$$\tilde{\mathcal{A}}_n(\Omega_1,z)\,\tilde{\mathcal{A}}^*_p(-\Omega+\Omega_1+\Omega_3,z)\,\tilde{\mathcal{A}}^*_q(-\Omega_3,z)\;\mathrm{d}\Omega_1\mathrm{d}\Omega_3$$

$$
\begin{aligned}
&+\frac{1}{4}i\Omega\frac{\epsilon_0}{4\left(2\pi\right)^2}\left[\exp\left(i\phi_m\left(\Omega,z\right)\right)\right]^*\sum_{n,p,q}\int\int\tilde{\chi}^{(3)}_{mnpq}\left(\Omega-\Omega_1\right)\\
&\int\int\left[\widehat{\boldsymbol{\mathcal{E}}}^*_m\left(\Omega,x,y,z\right)\cdot\widehat{\boldsymbol{\mathcal{E}}}_n\left(\Omega_1,x,y,z\right)\widehat{\boldsymbol{\mathcal{E}}}^*_p\left(-\Omega+\Omega_1+\Omega_3,x,y,z\right)\cdot\widehat{\boldsymbol{\mathcal{E}}}_q\left(\Omega_3,x,y,z\right)\right]\mathrm{d}x\mathrm{d}y\\
&\exp\left(i\phi_n\left(\Omega_1,z\right)\right)\exp\left(-i\phi^*_p\left(-\Omega+\Omega_1+\Omega_3,z\right)\right)\exp\left(i\phi_q\left(\Omega_3,z\right)\right)\\
&\tilde{\mathcal{A}}_n\left(\Omega_1,z\right)\tilde{\mathcal{A}}^*_p\left(-\Omega+\Omega_1+\Omega_3,z\right)\tilde{\mathcal{A}}_q\left(\Omega_3,z\right)\,\mathrm{d}\Omega_1\mathrm{d}\Omega_3\\
&+\frac{1}{4}i\Omega\frac{\epsilon_0}{4\left(2\pi\right)^2}\left[\exp\left(i\phi_m\left(\Omega,z\right)\right)\right]^*\sum_{n,p,q}\int\int\tilde{\chi}^{(3)}_{mnpq}\left(\Omega-\Omega_1\right)\\
&\int\int\left[\widehat{\boldsymbol{\mathcal{E}}}^*_m\left(\Omega,x,y,z\right)\cdot\widehat{\boldsymbol{\mathcal{E}}}^*_n\left(-\Omega_1,x,y,z\right)\widehat{\boldsymbol{\mathcal{E}}}_p\left(\Omega-\Omega_1-\Omega_3,x,y,z\right)\cdot\widehat{\boldsymbol{\mathcal{E}}}^*_q\left(-\Omega_3,x,y,z\right)\right]\mathrm{d}x\mathrm{d}y\\
&\exp\left(-i\phi^*_n\left(-\Omega_1,z\right)\right)\exp\left(i\phi_p\left(\Omega-\Omega_1-\Omega_3,z\right)\right)\exp\left(-i\phi^*_q\left(-\Omega_3,z\right)\right)\\
&\tilde{\mathcal{A}}^*_n\left(-\Omega_1,z\right)\tilde{\mathcal{A}}_p\left(\Omega-\Omega_1-\Omega_3,z\right)\tilde{\mathcal{A}}^*_q\left(-\Omega_3,z\right)\,\mathrm{d}\Omega_1\mathrm{d}\Omega_3\\
&+\frac{1}{4}i\Omega\frac{\epsilon_0}{4\left(2\pi\right)^2}\left[\exp\left(i\phi_m\left(\Omega,z\right)\right)\right]^*\sum_{n,p,q}\int\int\tilde{\chi}^{(3)}_{mnpq}\left(\Omega-\Omega_1\right)\\
&\int\int\left[\widehat{\boldsymbol{\mathcal{E}}}^*_m\left(\Omega,x,y,z\right)\cdot\widehat{\boldsymbol{\mathcal{E}}}_n\left(\Omega_1,x,y,z\right)\widehat{\boldsymbol{\mathcal{E}}}_p\left(\Omega-\Omega_1-\Omega_3,x,y,z\right)\cdot\widehat{\boldsymbol{\mathcal{E}}}^*_q\left(-\Omega_3,x,y,z\right)\right]\mathrm{d}x\mathrm{d}y\\
&\exp\left(i\phi_n\left(\Omega_1,z\right)\right)\exp\left(i\phi_p\left(\Omega-\Omega_1-\Omega_3,z\right)\right)\exp\left(-i\phi^*_q\left(-\Omega_3,z\right)\right)\\
&\tilde{\mathcal{A}}_n\left(\Omega_1,z\right)\tilde{\mathcal{A}}_p\left(\Omega-\Omega_1-\Omega_3,z\right)\tilde{\mathcal{A}}^*_q\left(-\Omega_3,z\right)\,\mathrm{d}\Omega_1\mathrm{d}\Omega_3\\
&+\frac{1}{4}i\Omega\frac{\epsilon_0}{4\left(2\pi\right)^2}\left[\exp\left(i\phi_m\left(\Omega,z\right)\right)\right]^*\sum_{n,p,q}\int\int\tilde{\chi}^{(3)}_{mnpq}\left(\Omega-\Omega_1\right)\\
&\int\int\left[\widehat{\boldsymbol{\mathcal{E}}}^*_m\left(\Omega,x,y,z\right)\cdot\widehat{\boldsymbol{\mathcal{E}}}^*_n\left(-\Omega_1,x,y,z\right)\widehat{\boldsymbol{\mathcal{E}}}^*_p\left(-\Omega+\Omega_1+\Omega_3,x,y,z\right)\cdot\widehat{\boldsymbol{\mathcal{E}}}_q\left(\Omega_3,x,y,z\right)\right]\mathrm{d}x\mathrm{d}y\\
&\exp\left(-i\phi^*_n\left(-\Omega_1,z\right)\right)\exp\left(-i\phi^*_p\left(-\Omega+\Omega_1+\Omega_3,z\right)\right)\exp\left(i\phi_q\left(\Omega_3,z\right)\right)\\
&\tilde{\mathcal{A}}^*_n\left(-\Omega_1,z\right)\tilde{\mathcal{A}}^*_p\left(-\Omega+\Omega_1+\Omega_3,z\right)\tilde{\mathcal{A}}_q\left(\Omega_3,z\right)\,\mathrm{d}\Omega_1\mathrm{d}\Omega_3
\end{aligned}
\tag{3.52}
$$

We see that we can split the equation in two equations (made explicit by the choice of color), where one equation is the complex conjugate taken at negative frequencies of the other. The solution to one equation is thus guaranteed to be a solution to the other, and therefore also a solution to the overall problem. The difference from this equation to the previous one is that this equation is an envelope equation. To get the full solution one needs to add together both solutions, which then guarantees a real electric field in time. In practice we can solve one of the two equations, and then add it with its complex conjugate of negative frequencies. Using the solution from one equation without adding its complex conjugate of negative frequencies will give the envelope solution in both time and frequency domains. Hence why each of the two equations are named envelope equations. Writing one out,

$$
\frac{\partial}{\partial z}\left[\exp\left(-2\,\mathrm{Im}\left(\phi_m\left(\Omega,z\right)\right)\right)\tilde{\mathcal{A}}_m\left(\Omega,z\right)\right]=
$$

$$
\begin{aligned}
&\frac{1}{4}i\Omega\frac{\epsilon_0}{4\left(2\pi\right)^2}\left[\exp\left(i\phi_m\left(\Omega,z\right)\right)\right]^*\sum_{n,p,q}\int\int\tilde{\chi}^{(3)}_{mnpq}\left(\Omega-\Omega_1\right)\\
&\int\int\left[\widehat{\boldsymbol{\mathcal{E}}}^*_m\left(\Omega,x,y,z\right)\cdot\widehat{\boldsymbol{\mathcal{E}}}_n\left(\Omega_1,x,y,z\right)\widehat{\boldsymbol{\mathcal{E}}}_p\left(\Omega-\Omega_1-\Omega_3,x,y,z\right)\cdot\widehat{\boldsymbol{\mathcal{E}}}_q\left(\Omega_3,x,y,z\right)\right]\mathrm{d}x\mathrm{d}y\\
&\exp\left(i\phi_n\left(\Omega_1,z\right)\right)\exp\left(i\phi_p\left(\Omega-\Omega_1-\Omega_3,z\right)\right)\exp\left(i\phi_q\left(\Omega_3,z\right)\right)\\
&\tilde{\mathcal{A}}_n\left(\Omega_1,z\right)\tilde{\mathcal{A}}_p\left(\Omega-\Omega_1-\Omega_3,z\right)\tilde{\mathcal{A}}_q\left(\Omega_3,z\right)\,\mathrm{d}\Omega_1\mathrm{d}\Omega_3\\
&+\frac{1}{4}i\Omega\frac{\epsilon_0}{4\left(2\pi\right)^2}\left[\exp\left(i\phi_m\left(\Omega,z\right)\right)\right]^*\sum_{n,p,q}\int\int\tilde{\chi}^{(3)}_{mnpq}\left(\Omega-\Omega_1\right)\\
&\int\int\left[\widehat{\boldsymbol{\mathcal{E}}}^*_m\left(\Omega,x,y,z\right)\cdot\widehat{\boldsymbol{\mathcal{E}}}^*_n\left(-\Omega_1,x,y,z\right)\widehat{\boldsymbol{\mathcal{E}}}_p\left(\Omega-\Omega_1-\Omega_3,x,y,z\right)\cdot\widehat{\boldsymbol{\mathcal{E}}}_q\left(\Omega_3,x,y,z\right)\right]\mathrm{d}x\mathrm{d}y\\
&\exp\left(-i\phi^*_n\left(-\Omega_1,z\right)\right)\exp\left(i\phi_p\left(\Omega-\Omega_1-\Omega_3,z\right)\right)\exp\left(i\phi_q\left(\Omega_3,z\right)\right)\\
&\tilde{\mathcal{A}}^*_n\left(-\Omega_1,z\right)\tilde{\mathcal{A}}_p\left(\Omega-\Omega_1-\Omega_3,z\right)\tilde{\mathcal{A}}_q\left(\Omega_3,z\right)\,\mathrm{d}\Omega_1\mathrm{d}\Omega_3\\
&+\frac{1}{4}i\Omega\frac{\epsilon_0}{4\left(2\pi\right)^2}\left[\exp\left(i\phi_m\left(\Omega,z\right)\right)\right]^*\sum_{n,p,q}\int\int\tilde{\chi}^{(3)}_{mnpq}\left(\Omega-\Omega_1\right)\\
&\int\int\left[\widehat{\boldsymbol{\mathcal{E}}}^*_m\left(\Omega,x,y,z\right)\cdot\widehat{\boldsymbol{\mathcal{E}}}_n\left(\Omega_1,x,y,z\right)\widehat{\boldsymbol{\mathcal{E}}}^*_p\left(-\Omega+\Omega_1+\Omega_3,x,y,z\right)\cdot\widehat{\boldsymbol{\mathcal{E}}}_q\left(\Omega_3,x,y,z\right)\right]\mathrm{d}x\mathrm{d}y\\
&\exp\left(i\phi_n\left(\Omega_1,z\right)\right)\exp\left(-i\phi^*_p\left(-\Omega+\Omega_1+\Omega_3,z\right)\right)\exp\left(i\phi_q\left(\Omega_3,z\right)\right)\\
&\tilde{\mathcal{A}}_n\left(\Omega_1,z\right)\tilde{\mathcal{A}}^*_p\left(-\Omega+\Omega_1+\Omega_3,z\right)\tilde{\mathcal{A}}_q\left(\Omega_3,z\right)\,\mathrm{d}\Omega_1\mathrm{d}\Omega_3\\
&+\frac{1}{4}i\Omega\frac{\epsilon_0}{4\left(2\pi\right)^2}\left[\exp\left(i\phi_m\left(\Omega,z\right)\right)\right]^*\sum_{n,p,q}\int\int\tilde{\chi}^{(3)}_{mnpq}\left(\Omega-\Omega_1\right)\\
&\int\int\left[\widehat{\boldsymbol{\mathcal{E}}}^*_m\left(\Omega,x,y,z\right)\cdot\widehat{\boldsymbol{\mathcal{E}}}_n\left(\Omega_1,x,y,z\right)\widehat{\boldsymbol{\mathcal{E}}}_p\left(\Omega-\Omega_1-\Omega_3,x,y,z\right)\cdot\widehat{\boldsymbol{\mathcal{E}}}^*_q\left(-\Omega_3,x,y,z\right)\right]\mathrm{d}x\mathrm{d}y\\
&\exp\left(i\phi_n\left(\Omega_1,z\right)\right)\exp\left(i\phi_p\left(\Omega-\Omega_1-\Omega_3,z\right)\right)\exp\left(-i\phi^*_q\left(-\Omega_3,z\right)\right)\\
&\tilde{\mathcal{A}}_n\left(\Omega_1,z\right)\tilde{\mathcal{A}}_p\left(\Omega-\Omega_1-\Omega_3,z\right)\tilde{\mathcal{A}}^*_q\left(-\Omega_3,z\right)\,\mathrm{d}\Omega_1\mathrm{d}\Omega_3
\end{aligned}
\tag{3.53}
$$

we are now ready to proceed in order to reduce the equation to FFT form. Showing that the red and blue equations are indeed each others complex conjugate at negative frequencies can be done. One beautiful symmetry property that is made clear through doing it is that the signs on Ω_1 and Ω_3 can be flipped freely, as long as both are flipped if one is flipped. The trick is to use the identities in Eq. (3.45)-(3.47) as well as substitutions and integral limit inversion rules, while using the knowledge that the nonlinear tensor is also hermitian.

3.4 Reduction of the derived expression to FFT form

Now that the equation has been derived, we can see there are two nasty convolutions in each term, which could take significant time to compute. We can also see that perhaps we can get rid of these by making use of the convolution theorem and suitable approximations.

In particular we need the convolution theorem for the inverse Fourier transform,

$$\mathcal{F}\left[f\left(t\right)g\left(t\right)\right]\left(\Omega\right)=\frac{1}{2\pi}\int\mathcal{F}\left[f\left(t\right)\right]\left(\Omega-\Omega_1\right)\mathcal{F}\left[g\left(t\right)\right]\left(\Omega_1\right)\,\mathrm{d}\Omega_1. \tag{3.54}$$

In the following two subsections I will first make the change to FFT form in the simple case where we assume the transverse integral is frequency independent, and then in the more general case where we assume it can be factorized into functions of a single variable.

3.4.1 Simple Approach

In Eq. 3.53, by assuming *all the transverse integral functions can be safely evaluated at* Ω_0 *irrespective of the actual frequencies involved*, we see that we can immediatly rearrange the equation and move the $\mathrm{d}\Omega_3$ integral to only encompass the envelope and phase of the p and q terms.

$$\begin{aligned}
&\frac{\partial}{\partial z}\left[\exp\left(-2\,\mathrm{Im}\left(\phi_m\left(\Omega,z\right)\right)\right)\tilde{\mathcal{A}}_m\left(\Omega,z\right)\right]=\\
&\frac{1}{4}i\Omega\frac{\epsilon_0}{4\left(2\pi\right)^2}\left[\exp\left(i\phi_m\left(\Omega,z\right)\right)\right]^*\sum_{n,p,q}\\
&\int\int\left[\widehat{\boldsymbol{\mathcal{E}}}_m^*\left(\Omega_0,x,y,z\right)\cdot\widehat{\boldsymbol{\mathcal{E}}}_n\left(\Omega_0,x,y,z\right)\widehat{\boldsymbol{\mathcal{E}}}_p\left(\Omega_0,x,y,z\right)\cdot\widehat{\boldsymbol{\mathcal{E}}}_q\left(\Omega_0,x,y,z\right)\right]\mathrm{d}x\mathrm{d}y\\
&\int\tilde{\chi}^{(3)}_{mnpq}\left(\Omega-\Omega_1\right)\tilde{\mathcal{A}}_n\left(\Omega_1,z\right)\exp\left(i\phi_n\left(\Omega_1,z\right)\right)\\
&\int\underbrace{\tilde{\mathcal{A}}_p\left(\Omega-\Omega_1-\Omega_3,z\right)\exp\left(i\phi_p\left(\Omega-\Omega_1-\Omega_3,z\right)\right)}\underbrace{\tilde{\mathcal{A}}_q\left(\Omega_3,z\right)\exp\left(i\phi_q\left(\Omega_3,z\right)\right)}\,\mathrm{d}\Omega_3\mathrm{d}\Omega_1\\
&+\frac{1}{4}i\Omega\frac{\epsilon_0}{4\left(2\pi\right)^2}\left[\exp\left(i\phi_m\left(\Omega,z\right)\right)\right]^*\sum_{n,p,q}\\
&\int\int\left[\widehat{\boldsymbol{\mathcal{E}}}_m^*\left(\Omega_0,x,y,z\right)\cdot\widehat{\boldsymbol{\mathcal{E}}}_n^*\left(\Omega_0,x,y,z\right)\widehat{\boldsymbol{\mathcal{E}}}_p\left(\Omega_0,x,y,z\right)\cdot\widehat{\boldsymbol{\mathcal{E}}}_q\left(\Omega_0,x,y,z\right)\right]\mathrm{d}x\mathrm{d}y\\
&\int\tilde{\chi}^{(3)}_{mnpq}\left(\Omega-\Omega_1\right)\tilde{\mathcal{A}}_n^*\left(-\Omega_1,z\right)\exp\left(-i\phi_n^*\left(-\Omega_1,z\right)\right)\\
&\int\underbrace{\tilde{\mathcal{A}}_p\left(\Omega-\Omega_1-\Omega_3,z\right)\exp\left(i\phi_p\left(\Omega-\Omega_1-\Omega_3,z\right)\right)}\underbrace{\tilde{\mathcal{A}}_q\left(\Omega_3,z\right)\exp\left(i\phi_q\left(\Omega_3,z\right)\right)}\,\mathrm{d}\Omega_3\mathrm{d}\Omega_1\\
&+\frac{1}{4}i\Omega\frac{\epsilon_0}{4\left(2\pi\right)^2}\left[\exp\left(i\phi_m\left(\Omega,z\right)\right)\right]^*\sum_{n,p,q}\\
&\int\int\left[\widehat{\boldsymbol{\mathcal{E}}}_m^*\left(\Omega_0,x,y,z\right)\cdot\widehat{\boldsymbol{\mathcal{E}}}_n\left(\Omega_0,x,y,z\right)\widehat{\boldsymbol{\mathcal{E}}}_p^*\left(\Omega_0,x,y,z\right)\cdot\widehat{\boldsymbol{\mathcal{E}}}_q\left(\Omega_0,x,y,z\right)\right]\mathrm{d}x\mathrm{d}y\\
&\int\tilde{\chi}^{(3)}_{mnpq}\left(\Omega-\Omega_1\right)\tilde{\mathcal{A}}_n\left(\Omega_1,z\right)\exp\left(i\phi_n\left(\Omega_1,z\right)\right)\\
&\int\underbrace{\tilde{\mathcal{A}}_p^*\left(-\Omega+\Omega_1+\Omega_3,z\right)\exp\left(-i\phi_p^*\left(-\Omega+\Omega_1+\Omega_3,z\right)\right)}\underbrace{\tilde{\mathcal{A}}_q\left(\Omega_3,z\right)\exp\left(i\phi_q\left(\Omega_3,z\right)\right)}\,\mathrm{d}\Omega_3\mathrm{d}\Omega_1
\end{aligned}$$

$$
\begin{aligned}
&+\frac{1}{4}i\Omega\frac{\epsilon_0}{4\left(2\pi\right)^2}\left[\exp\left(i\phi_m\left(\Omega,z\right)\right)\right]^*\sum_{n,p,q}\\
&\int\int\left[\widehat{\boldsymbol{\mathcal{E}}}_m^*\left(\Omega_0,x,y,z\right)\cdot\widehat{\boldsymbol{\mathcal{E}}}_n\left(\Omega_0,x,y,z\right)\widehat{\boldsymbol{\mathcal{E}}}_p\left(\Omega_0,x,y,z\right)\cdot\widehat{\boldsymbol{\mathcal{E}}}_q^*\left(\Omega_0,x,y,z\right)\right]\mathrm{d}x\mathrm{d}y\\
&\int\tilde{\chi}_{mnpq}^{(3)}\left(\Omega-\Omega_1\right)\tilde{\mathcal{A}}_n\left(\Omega_1,z\right)\exp\left(i\phi_n\left(\Omega_1,z\right)\right)\\
&\int\underbrace{\tilde{\mathcal{A}}_p\left(\Omega-\Omega_1-\Omega_3,z\right)\exp\left(i\phi_p\left(\Omega-\Omega_1-\Omega_3,z\right)\right)}\underbrace{\tilde{\mathcal{A}}_q^*\left(-\Omega_3,z\right)\exp\left(-i\phi_q^*\left(-\Omega_3,z\right)\right)}\,\mathrm{d}\Omega_3\mathrm{d}\Omega_1
\end{aligned}
\tag{3.55}
$$

This approximation should hold as long as the involved frequencies at any time are not too far apart, which for practical purposes translates to supercontinua where the generated bandwidth at any point is much smaller than the carrier frequency. The underlined markings show how the Ω_3 integral has the exact form for the inverse convolution theorem in Eq. (3.54). We can apply it to obtain an expression involving Fourier and inverse Fourier transforms instead of one of the integrals.

$$
\begin{aligned}
&\frac{\partial}{\partial z}\left[\exp\left(-2\,\mathrm{Im}\left(\phi_m\left(\Omega,z\right)\right)\right)\tilde{\mathcal{A}}_m\left(\Omega,z\right)\right]=\\
&\frac{1}{4}i\Omega\frac{\epsilon_0}{4\left(2\pi\right)}\left[\exp\left(i\phi_m\left(\Omega,z\right)\right)\right]^*\sum_{n,p,q}\\
&\int\int\left[\widehat{\boldsymbol{\mathcal{E}}}_m^*\left(\Omega_0,x,y,z\right)\cdot\widehat{\boldsymbol{\mathcal{E}}}_n\left(\Omega_0,x,y,z\right)\widehat{\boldsymbol{\mathcal{E}}}_p\left(\Omega_0,x,y,z\right)\cdot\widehat{\boldsymbol{\mathcal{E}}}_q\left(\Omega_0,x,y,z\right)\right]\mathrm{d}x\mathrm{d}y\\
&\int\tilde{\chi}_{mnpq}^{(3)}\left(\Omega-\Omega_1\right)\tilde{\mathcal{A}}_n\left(\Omega_1,z\right)\exp\left(i\phi_n\left(\Omega_1,z\right)\right)\\
&\mathcal{F}\left[\mathcal{F}^{-1}\left[\tilde{\mathcal{A}}_p\left(\Omega,z\right)\exp\left(i\phi_p\left(\Omega,z\right)\right)\right]\mathcal{F}^{-1}\left[\tilde{\mathcal{A}}_q\left(\Omega,z\right)\exp\left(i\phi_q\left(\Omega,z\right)\right)\right]\right]\left(\Omega-\Omega_1\right)\,\mathrm{d}\Omega_1\\
&+\frac{1}{4}i\Omega\frac{\epsilon_0}{4\left(2\pi\right)}\left[\exp\left(i\phi_m\left(\Omega,z\right)\right)\right]^*\sum_{n,p,q}\\
&\int\int\left[\widehat{\boldsymbol{\mathcal{E}}}_m^*\left(\Omega_0,x,y,z\right)\cdot\widehat{\boldsymbol{\mathcal{E}}}_n^*\left(\Omega_0,x,y,z\right)\widehat{\boldsymbol{\mathcal{E}}}_p\left(\Omega_0,x,y,z\right)\cdot\widehat{\boldsymbol{\mathcal{E}}}_q\left(\Omega_0,x,y,z\right)\right]\mathrm{d}x\mathrm{d}y\\
&\int\tilde{\chi}_{mnpq}^{(3)}\left(\Omega-\Omega_1\right)\tilde{\mathcal{A}}_n^*\left(-\Omega_1,z\right)\exp\left(-i\phi_n^*\left(-\Omega_1,z\right)\right)\\
&\mathcal{F}\left[\mathcal{F}^{-1}\left[\tilde{\mathcal{A}}_p\left(\Omega,z\right)\exp\left(i\phi_p\left(\Omega,z\right)\right)\right]\mathcal{F}^{-1}\left[\tilde{\mathcal{A}}_q\left(\Omega,z\right)\exp\left(i\phi_q\left(\Omega,z\right)\right)\right]\right]\left(\Omega-\Omega_1\right)\,\mathrm{d}\Omega_1\\
&+\frac{1}{4}i\Omega\frac{\epsilon_0}{4\left(2\pi\right)}\left[\exp\left(i\phi_m\left(\Omega,z\right)\right)\right]^*\sum_{n,p,q}\\
&\int\int\left[\widehat{\boldsymbol{\mathcal{E}}}_m^*\left(\Omega_0,x,y,z\right)\cdot\widehat{\boldsymbol{\mathcal{E}}}_n\left(\Omega_0,x,y,z\right)\widehat{\boldsymbol{\mathcal{E}}}_p^*\left(\Omega_0,x,y,z\right)\cdot\widehat{\boldsymbol{\mathcal{E}}}_q\left(\Omega_0,x,y,z\right)\right]\mathrm{d}x\mathrm{d}y\\
&\int\tilde{\chi}_{mnpq}^{(3)}\left(\Omega-\Omega_1\right)\tilde{\mathcal{A}}_n\left(\Omega_1,z\right)\exp\left(i\phi_n\left(\Omega_1,z\right)\right)\\
&\mathcal{F}\left[\mathcal{F}^{-1}\left[\tilde{\mathcal{A}}_p^*\left(\Omega,z\right)\exp\left(-i\phi_p^*\left(\Omega,z\right)\right)\right]\mathcal{F}^{-1}\left[\tilde{\mathcal{A}}_q\left(\Omega,z\right)\exp\left(i\phi_q\left(\Omega,z\right)\right)\right]\right]\left(\Omega-\Omega_1\right)\,\mathrm{d}\Omega_1
\end{aligned}
$$

$$
\begin{aligned}
&+\frac{1}{4}i\Omega\frac{\epsilon_0}{4\left(2\pi\right)}\left[\exp\left(i\phi_m\left(\Omega,z\right)\right)\right]^*\sum_{n,p,q}\\
&\int\int\left[\widehat{\boldsymbol{\mathcal{E}}}_m^*\left(\Omega_0,x,y,z\right)\cdot\widehat{\boldsymbol{\mathcal{E}}}_n\left(\Omega_0,x,y,z\right)\widehat{\boldsymbol{\mathcal{E}}}_p\left(\Omega_0,x,y,z\right)\cdot\widehat{\boldsymbol{\mathcal{E}}}_q^*\left(\Omega_0,x,y,z\right)\right]\mathrm{d}x\mathrm{d}y\\
&\int\tilde{\chi}_{mnpq}^{(3)}\left(\Omega-\Omega_1\right)\tilde{\mathcal{A}}_n\left(\Omega_1,z\right)\exp\left(i\phi_n\left(\Omega_1,z\right)\right)\\
&\mathcal{F}\left[\mathcal{F}^{-1}\left[\tilde{\mathcal{A}}_p\left(\Omega,z\right)\exp\left(i\phi_p\left(\Omega,z\right)\right)\right]\mathcal{F}^{-1}\left[\tilde{\mathcal{A}}_q^*\left(\Omega,z\right)\exp\left(-i\phi_q^*\left(\Omega,z\right)\right)\right]\right]\left(\Omega-\Omega_1\right)\,\mathrm{d}\Omega_1
\end{aligned}
\tag{3.56}
$$

We can use Eq. (3.54) a second time to get rid of the Ω_1 integral as well. At the same time we prepare the equation for numerical implementation, by making the phase variable change

$$
\tilde{C}_n\left(\Omega,z\right)=\tilde{\mathcal{A}}_n\left(\Omega,z\right)\exp\left(i\phi_n\left(\Omega,z\right)\right)
\tag{3.57}
$$

and using that we can move the complex conjugates outside the Fourier transform through use of Eq. (3.45) to (3.49). All this combines to yield

$$
\begin{aligned}
&\frac{\partial}{\partial z}\left[\left[\exp\left(i\phi_m\left(\Omega,z\right)\right)\right]^*\tilde{C}_m\left(\Omega,z\right)\right]=\\
&\frac{1}{4}i\Omega\frac{\epsilon_0}{4}\left[\exp\left(i\phi_m\left(\Omega,z\right)\right)\right]^*\sum_{n,p,q}\\
&\int\int\left[\widehat{\boldsymbol{\mathcal{E}}}_m^*\left(\Omega_0,x,y,z\right)\cdot\widehat{\boldsymbol{\mathcal{E}}}_n\left(\Omega_0,x,y,z\right)\widehat{\boldsymbol{\mathcal{E}}}_p\left(\Omega_0,x,y,z\right)\cdot\widehat{\boldsymbol{\mathcal{E}}}_q\left(\Omega_0,x,y,z\right)\right]\mathrm{d}x\mathrm{d}y\\
&\mathcal{F}\Big[\mathcal{F}^{-1}\left[\tilde{C}_n\left(\Omega,z\right)\right]\mathcal{F}^{-1}\Big[\tilde{\chi}_{mnpq}^{(3)}\left(\Omega\right)\\
&\mathcal{F}\left[\mathcal{F}^{-1}\left[\tilde{C}_p\left(\Omega,z\right)\right]\mathcal{F}^{-1}\left[\tilde{C}_q\left(\Omega,z\right)\right]\right]\left(\Omega\right)\Big]\Big]\left(\Omega\right)\\
&+\frac{1}{4}i\Omega\frac{\epsilon_0}{4}\left[\exp\left(i\phi_m\left(\Omega,z\right)\right)\right]^*\sum_{n,p,q}\\
&\int\int\left[\widehat{\boldsymbol{\mathcal{E}}}_m^*\left(\Omega_0,x,y,z\right)\cdot\widehat{\boldsymbol{\mathcal{E}}}_n^*\left(\Omega_0,x,y,z\right)\widehat{\boldsymbol{\mathcal{E}}}_p\left(\Omega_0,x,y,z\right)\cdot\widehat{\boldsymbol{\mathcal{E}}}_q\left(\Omega_0,x,y,z\right)\right]\mathrm{d}x\mathrm{d}y\\
&\mathcal{F}\Big[\mathcal{F}^{-1}\left[\tilde{C}_n\left(\Omega,z\right)\right]^*\mathcal{F}^{-1}\Big[\tilde{\chi}_{mnpq}^{(3)}\left(\Omega\right)\\
&\mathcal{F}\left[\mathcal{F}^{-1}\left[\tilde{C}_p\left(\Omega,z\right)\right]\mathcal{F}^{-1}\left[\tilde{C}_q\left(\Omega,z\right)\right]\right]\left(\Omega\right)\Big]\Big]\left(\Omega\right)\\
&+\frac{1}{4}i\Omega\frac{\epsilon_0}{4}\left[\exp\left(i\phi_m\left(\Omega,z\right)\right)\right]^*\sum_{n,p,q}\\
&\int\int\left[\widehat{\boldsymbol{\mathcal{E}}}_m^*\left(\Omega_0,x,y,z\right)\cdot\widehat{\boldsymbol{\mathcal{E}}}_n\left(\Omega_0,x,y,z\right)\widehat{\boldsymbol{\mathcal{E}}}_p^*\left(\Omega_0,x,y,z\right)\cdot\widehat{\boldsymbol{\mathcal{E}}}_q\left(\Omega_0,x,y,z\right)\right]\mathrm{d}x\mathrm{d}y\\
&\mathcal{F}\Big[\mathcal{F}^{-1}\left[\tilde{C}_n\left(\Omega,z\right)\right]\mathcal{F}^{-1}\Big[\tilde{\chi}_{mnpq}^{(3)}\left(\Omega\right)\\
&\mathcal{F}\left[\mathcal{F}^{-1}\left[\tilde{C}_p\left(\Omega,z\right)\right]^*\mathcal{F}^{-1}\left[\tilde{C}_q\left(\Omega,z\right)\right]\right]\left(\Omega\right)\Big]\Big]\left(\Omega\right)
\end{aligned}
$$

$$
\begin{aligned}
&+\frac{1}{4}i\Omega\frac{\epsilon_0}{4}\left[\exp\left(i\phi_m\left(\Omega,z\right)\right)\right]^*\sum_{n,p,q}\\
&\int\int\left[\widehat{\boldsymbol{\mathcal{E}}}_m^*\left(\Omega_0,x,y,z\right)\cdot\widehat{\boldsymbol{\mathcal{E}}}_n\left(\Omega_0,x,y,z\right)\widehat{\boldsymbol{\mathcal{E}}}_p\left(\Omega_0,x,y,z\right)\cdot\widehat{\boldsymbol{\mathcal{E}}}_q^*\left(\Omega_0,x,y,z\right)\right]\mathrm{d}x\mathrm{d}y\\
&\mathcal{F}\Big[\mathcal{F}^{-1}\left[\tilde{C}_n\left(\Omega,z\right)\right]\mathcal{F}^{-1}\Big[\tilde{\chi}^{(3)}_{mnpq}\left(\Omega\right)\\
&\mathcal{F}\left[\mathcal{F}^{-1}\left[\tilde{C}_p\left(\Omega,z\right)\right]\mathcal{F}^{-1}\left[\tilde{C}_q\left(\Omega,z\right)\right]^*\right]\left(\Omega\right)\Big]\Big]\left(\Omega\right)
\end{aligned}
\tag{3.58}
$$

Note how the imaginary part of the phase inside the differentiation on the left side of the equality made sure that the leftover phase terms on both sides match. It was obtained with the identity

$$
\exp\left(-2\,\mathrm{Im}\left(\phi_m\left(\Omega,z\right)\right)\right)=\left[\exp\left(i\phi_m\left(\Omega,z\right)\right)\right]^*\exp\left(i\phi_m\left(\Omega,z\right)\right)
\tag{3.59}
$$

By carrying out the differentiation on the left hand side and limiting the sums to a single mode we would end up with the usual result, including the correct form of the loss. This will be done in chapter 4.

3.4.2 Mode Profile Dispersion

Instead of approximating the transverse overlap integrals directly with a fixed value, let us now take a look at what can be done to get it outside the convolution integrals. The most obvious method is to do as in [39], and make a Taylor expansion in the four variables, and then assign each term to the envelope and phase terms with the same frequency dependency. The number of terms explode quickly, and this makes the method impractical. Instead we can, as also suggested in [46], do a factorization into a product of two. One factor that depends on frequency and not x, y, and another that does not depend on frequency, but includes the x, y dependence.

$$
\widehat{\boldsymbol{\mathcal{E}}}_m\left(\Omega,x,y,z\right)\approx\widehat{\boldsymbol{\mathcal{E}}}_m\left(\Omega_0,x,y,z\right)K_m\left(\Omega,z\right)
\tag{3.60}
$$

The easiest way to do this is to simply approximate the electric field at Ω_0 and then the Ω dependance through a correction factor that contains the x, y average normalized to the value at Ω_0. Thus the correction factor is defined as

$$
K_m\left(\Omega,z\right)=\left[\frac{\int\int\left[\widehat{\boldsymbol{\mathcal{E}}}_m^*\left(\Omega,x,y,z\right)\cdot\widehat{\boldsymbol{\mathcal{E}}}_m\left(\Omega,x,y,z\right)\widehat{\boldsymbol{\mathcal{E}}}_m^*\left(\Omega,x,y,z\right)\cdot\widehat{\boldsymbol{\mathcal{E}}}_m\left(\Omega,x,y,z\right)\right]\mathrm{d}x\mathrm{d}y}{\int\int\left[\widehat{\boldsymbol{\mathcal{E}}}_m^*\left(\Omega_0,x,y,z\right)\cdot\widehat{\boldsymbol{\mathcal{E}}}_m\left(\Omega_0,x,y,z\right)\widehat{\boldsymbol{\mathcal{E}}}_m^*\left(\Omega_0,x,y,z\right)\cdot\widehat{\boldsymbol{\mathcal{E}}}_m\left(\Omega_0,x,y,z\right)\right]\mathrm{d}x\mathrm{d}y}\right]^{\frac{1}{4}}
\tag{3.61}
$$

We see that $K_m\left(\Omega_0,z\right)=1$ as it should be. After this initial factorization the exact same method as in section 3.4.1 can be applied step by step. The result is almost the same equation,

$$
\frac{\partial}{\partial z}\left[\left[\exp\left(i\phi_m\left(\Omega,z\right)\right)\right]^*\tilde{C}_m\left(\Omega,z\right)\right]=
$$

$$
\begin{aligned}
&\frac{1}{4}i\Omega\frac{\epsilon_0}{4}\left[\exp\left(i\phi_m\left(\Omega,z\right)\right)\right]^* K_n\left(\Omega,z\right)\sum_{n,p,q}\\
&\int\int\left[\widehat{\boldsymbol{\mathcal{E}}}_m^*\left(\Omega_0,x,y,z\right)\cdot\widehat{\boldsymbol{\mathcal{E}}}_n\left(\Omega_0,x,y,z\right)\widehat{\boldsymbol{\mathcal{E}}}_p\left(\Omega_0,x,y,z\right)\cdot\widehat{\boldsymbol{\mathcal{E}}}_q\left(\Omega_0,x,y,z\right)\right]\mathrm{d}x\mathrm{d}y\\
&\mathcal{F}\Big[\mathcal{F}^{-1}\left[\tilde{C}_n\left(\Omega,z\right)K_n\left(\Omega,z\right)\right]\mathcal{F}^{-1}\Big[\tilde{\chi}^{(3)}_{mnpq}\left(\Omega\right)\\
&\mathcal{F}\left[\mathcal{F}^{-1}\left[\tilde{C}_p\left(\Omega,z\right)K_p\left(\Omega,z\right)\right]\mathcal{F}^{-1}\left[\tilde{C}_q\left(\Omega,z\right)K_p\left(\Omega,z\right)\right]\right]\left(\Omega\right)\Big]\Big]\left(\Omega\right)\\
&+\frac{1}{4}i\Omega\frac{\epsilon_0}{4}\left[\exp\left(i\phi_m\left(\Omega,z\right)\right)\right]^* K_m\left(\Omega,z\right)\sum_{n,p,q}\\
&\int\int\left[\widehat{\boldsymbol{\mathcal{E}}}_m^*\left(\Omega_0,x,y,z\right)\cdot\widehat{\boldsymbol{\mathcal{E}}}_n^*\left(\Omega_0,x,y,z\right)\widehat{\boldsymbol{\mathcal{E}}}_p\left(\Omega_0,x,y,z\right)\cdot\widehat{\boldsymbol{\mathcal{E}}}_q\left(\Omega_0,x,y,z\right)\right]\mathrm{d}x\mathrm{d}y\\
&\mathcal{F}\Big[\mathcal{F}^{-1}\left[\tilde{C}_n\left(\Omega,z\right)K_n\left(\Omega,z\right)\right]^*\mathcal{F}^{-1}\Big[\tilde{\chi}^{(3)}_{mnpq}\left(\Omega\right)\\
&\mathcal{F}\left[\mathcal{F}^{-1}\left[\tilde{C}_p\left(\Omega,z\right)K_p\left(\Omega,z\right)\right]\mathcal{F}^{-1}\left[\tilde{C}_q\left(\Omega,z\right)K_q\left(\Omega,z\right)\right]\right]\left(\Omega\right)\Big]\Big]\left(\Omega\right)\\
&+\frac{1}{4}i\Omega\frac{\epsilon_0}{4}\left[\exp\left(i\phi_m\left(\Omega,z\right)\right)\right]^* K_m\left(\Omega,z\right)\sum_{n,p,q}\\
&\int\int\left[\widehat{\boldsymbol{\mathcal{E}}}_m^*\left(\Omega_0,x,y,z\right)\cdot\widehat{\boldsymbol{\mathcal{E}}}_n\left(\Omega_0,x,y,z\right)\widehat{\boldsymbol{\mathcal{E}}}_p^*\left(\Omega_0,x,y,z\right)\cdot\widehat{\boldsymbol{\mathcal{E}}}_q\left(\Omega_0,x,y,z\right)\right]\mathrm{d}x\mathrm{d}y\\
&\mathcal{F}\Big[\mathcal{F}^{-1}\left[\tilde{C}_n\left(\Omega,z\right)K_n\left(\Omega,z\right)\right]\mathcal{F}^{-1}\Big[\tilde{\chi}^{(3)}_{mnpq}\left(\Omega\right)\\
&\mathcal{F}\left[\mathcal{F}^{-1}\left[\tilde{C}_p\left(\Omega,z\right)K_p\left(\Omega,z\right)\right]^*\mathcal{F}^{-1}\left[\tilde{C}_q\left(\Omega,z\right)K_q\left(\Omega,z\right)\right]\right]\left(\Omega\right)\Big]\Big]\left(\Omega\right)\\
&+\frac{1}{4}i\Omega\frac{\epsilon_0}{4}\left[\exp\left(i\phi_m\left(\Omega,z\right)\right)\right]^* K_m\left(\Omega,z\right)\sum_{n,p,q}\\
&\int\int\left[\widehat{\boldsymbol{\mathcal{E}}}_m^*\left(\Omega_0,x,y,z\right)\cdot\widehat{\boldsymbol{\mathcal{E}}}_n\left(\Omega_0,x,y,z\right)\widehat{\boldsymbol{\mathcal{E}}}_p\left(\Omega_0,x,y,z\right)\cdot\widehat{\boldsymbol{\mathcal{E}}}_q^*\left(\Omega_0,x,y,z\right)\right]\mathrm{d}x\mathrm{d}y\\
&\mathcal{F}\Big[\mathcal{F}^{-1}\left[\tilde{C}_n\left(\Omega,z\right)K_n\left(\Omega,z\right)\right]\mathcal{F}^{-1}\Big[\tilde{\chi}^{(3)}_{mnpq}\left(\Omega\right)\\
&\mathcal{F}\left[\mathcal{F}^{-1}\left[\tilde{C}_p\left(\Omega,z\right)K_p\left(\Omega,z\right)\right]\mathcal{F}^{-1}\left[\tilde{C}_q\left(\Omega,z\right)K_q\left(\Omega,z\right)\right]^*\right]\left(\Omega\right)\Big]\Big]\left(\Omega\right)
\end{aligned}
\tag{3.62}
$$

now including the correction factor. Using the same method as in [80], it can be shown that the photon number is conserved in this equation. Previously, the effective area has been used as the correction factor. As we are using the power normalization as opposed to the electric field normalization we do not directly get out the correction factor in terms of the effective area. Hence it does not make sense to introduce it here in place of the transverse integrals. As noted in [46], the frequency dependency contained in $K_m\left(\Omega,z\right)$ should be used with caution in cases involving more than two modes or transverse field distributions that are very non Gaussian. In chapter 4, Eq. 3.62 will be placed in context of other literatture in the field.

The equations should stand on their own as a conclusion to this chapter. Nevertheless,

a few remarks on how to make the equations more general still need to be printed. One way to make the equation more general would be to include second harmonic generation, in which case it would be possible to model non isotropic materials. A second way would be to include plasma generation to model for instance gas filled fibers, as well as rate equations to enable gain and amplification. In this case the dispersion should satisfy the Kramers-Kronig relation, which could have quite the influence for fibers with absorption lines.

Chapter 4

Comparison of the GNLSE to Literature

The equations governing nonlinear propagation in isotropic waveguides such as silica fibers were derived in chapter 3, Eq. (3.58) and (3.62). In this chapter it will be placed in the context of other literature in the field. An overview of this can be seen in Fig. 4.1. As previously mentioned, the very general equation derived in this work was based upon the method shown in [35] and refined in [33], leading to equation (18), and reiterated in [34], equation (A.1) to (A.15). In the subsequent papers by Poletti, Horak and Laegs-

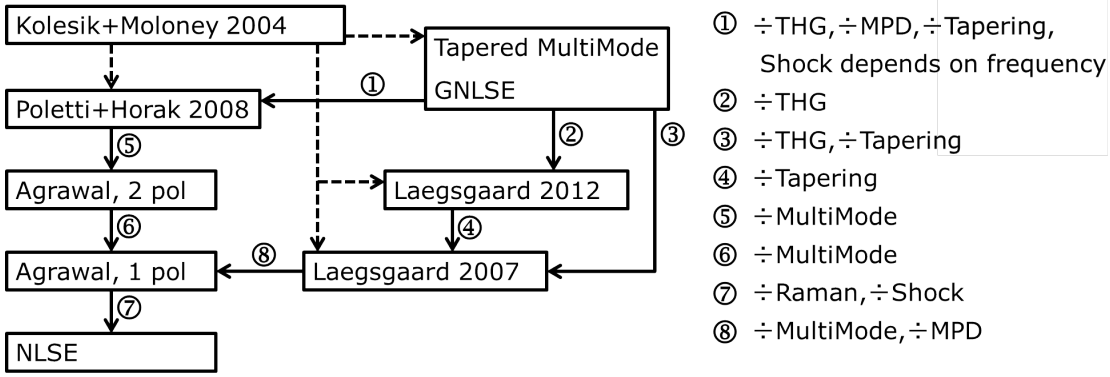

Figure 4.1: Overview of the different published versions of the Generalized Non Linear Schrödinger Equation (GNLSE) fits in compared to each other, in terms of approximations and applicability. The references are [2,33–35,39,40,62]. Dotted lines indicate inspiration, solid lines represent reduction of a more general equation to a less general case. The numbering and corresponding description describes under what conditions the narrowing of scope applies. THG and MPD stands for Third Harmonic Generation and Mode Profile Dispersion.

gaard [39, 40, 62] there are clear references to the work done by Kolesik, Wright and Moloney [33, 34] as the inspiration. In Fig. 4.1 this is indicated by the dotted lines. The final dotted line indicates the inspiration for the derivation in chapter 3 drawn from Laegsgaards inclusion of tapering in [40], but to be fair also [80] should be mentioned. While all the work can be traced back to [33, 34], there are differences in applicability and scope. It would be my claim that Eq. (3.58) and (3.62) are the most general, as they can be reduced to the results presented in [39, 40, 62]. Of these reductions, numbered (1), (2) and (3) in the figure, (1) will be the focus of the following subsection. The further reduction to the widely accepted and used results printed in [2], the numbered arrows (5) and (8), are shown in the respective papers [39, 62]. The arrows denoted (6) and (7) can be done directly and the result can be seen in different equations in [2].

The first step to any of the reductions is to throw away the third harmonic term. Considering the broadband guidance properties of PCF fibers and the high peak power nature of the solitons typically involved in SCG, this seems like very rough approximation. The second step is to note that two of the terms are identical under permutation of the sum ordering. With this, the equation becomes,

$$
\begin{aligned}
&\frac{\partial}{\partial z}\left[\left[\exp\left(i\phi_m\left(\Omega,z\right)\right)\right]^* \tilde{C}_m\left(\Omega,z\right)\right] = \\
&\frac{1}{4}i\Omega\frac{\epsilon_0}{4}\left[\exp\left(i\phi_m\left(\Omega,z\right)\right)\right]^* K_m\left(\Omega,z\right)\sum_{n,p,q} \\
&\int\int\left[\widehat{\boldsymbol{\mathcal{E}}}_m^*\left(\Omega_0,x,y,z\right)\cdot\widehat{\boldsymbol{\mathcal{E}}}_n^*\left(\Omega_0,x,y,z\right)\widehat{\boldsymbol{\mathcal{E}}}_p\left(\Omega_0,x,y,z\right)\cdot\widehat{\boldsymbol{\mathcal{E}}}_q\left(\Omega_0,x,y,z\right)\right]\mathrm{d}x\mathrm{d}y \\
&\mathcal{F}\left[\mathcal{F}^{-1}\left[\tilde{C}_n\left(\Omega,z\right)K_n\left(\Omega,z\right)\right]^*\mathcal{F}^{-1}\left[\tilde{\chi}^{(3)}_{mnpq}\left(\Omega\right)\right.\right. \\
&\left.\left.\mathcal{F}\left[\mathcal{F}^{-1}\left[\tilde{C}_p\left(\Omega,z\right)K_p\left(\Omega,z\right)\right]\mathcal{F}^{-1}\left[\tilde{C}_q\left(\Omega,z\right)K_q\left(\Omega,z\right)\right]\right]\left(\Omega\right)\right]\right]\left(\Omega\right) \\
&+\frac{2}{4}i\Omega\frac{\epsilon_0}{4}\left[\exp\left(i\phi_m\left(\Omega,z\right)\right)\right]^* K_m\left(\Omega,z\right)\sum_{n,p,q} \\
&\int\int\left[\widehat{\boldsymbol{\mathcal{E}}}_m^*\left(\Omega_0,x,y,z\right)\cdot\widehat{\boldsymbol{\mathcal{E}}}_n\left(\Omega_0,x,y,z\right)\widehat{\boldsymbol{\mathcal{E}}}_p^*\left(\Omega_0,x,y,z\right)\cdot\widehat{\boldsymbol{\mathcal{E}}}_q\left(\Omega_0,x,y,z\right)\right]\mathrm{d}x\mathrm{d}y \\
&\mathcal{F}\left[\mathcal{F}^{-1}\left[\tilde{C}_n\left(\Omega,z\right)K_n\left(\Omega,z\right)\right]\mathcal{F}^{-1}\left[\tilde{\chi}^{(3)}_{mnpq}\left(\Omega\right)\right.\right. \\
&\left.\left.\mathcal{F}\left[\mathcal{F}^{-1}\left[\tilde{C}_p\left(\Omega,z\right)K_p\left(\Omega,z\right)\right]^*\mathcal{F}^{-1}\left[\tilde{C}_q\left(\Omega,z\right)K_q\left(\Omega,z\right)\right]\right]\left(\Omega\right)\right]\right]\left(\Omega\right). \qquad (4.1)
\end{aligned}
$$

After getting rid of the third harmonic generation term it is possible to make another phase redifinition of the envelope, using the real function $\phi_0\left(z\right)$,

$$\tilde{G}_m\left(\Omega,z\right) = \tilde{C}_m\left(\Omega,z\right)\exp\left(i\phi_0\left(z\right)\right). \qquad (4.2)$$

The phase terms can be moved through the Fourier transforms as they have no dependency on frequency. Furthermore, the complex conjugation means that two of them on the right hand side go out with each other. This leaves a single term on each side of the equality

sign to be grouped with the already existing phase terms, $\exp\left(i\phi_m\left(\Omega,z\right)\right)$,

$$\begin{aligned}
&\frac{\partial}{\partial z}\left[\left[\exp\left(i\phi_m\left(\Omega,z\right)+i\phi_0\left(z\right)\right)\right]^*\tilde{G}_m\left(\Omega,z\right)\right]=\\
&\frac{1}{4}i\Omega\frac{\epsilon_0}{4}\left[\exp\left(i\phi_m\left(\Omega,z\right)\right)+i\phi_0\left(z\right)\right]^*K_m\left(\Omega,z\right)\sum_{n,p,q}\\
&\int\int\left[\widehat{\boldsymbol{\mathcal{E}}}_m^*\left(\Omega_0,x,y,z\right)\cdot\widehat{\boldsymbol{\mathcal{E}}}_n^*\left(\Omega_0,x,y,z\right)\widehat{\boldsymbol{\mathcal{E}}}_p\left(\Omega_0,x,y,z\right)\cdot\widehat{\boldsymbol{\mathcal{E}}}_q\left(\Omega_0,x,y,z\right)\right]\mathrm{d}x\mathrm{d}y\\
&\mathcal{F}\Big[\mathcal{F}^{-1}\left[\tilde{G}_n\left(\Omega,z\right)K_n\left(\Omega,z\right)\right]^*\mathcal{F}^{-1}\Big[\tilde{\chi}^{(3)}_{mnpq}\left(\Omega\right)\\
&\mathcal{F}\left[\mathcal{F}^{-1}\left[\tilde{G}_p\left(\Omega,z\right)K_p\left(\Omega,z\right)\right]\mathcal{F}^{-1}\left[\tilde{G}_q\left(\Omega,z\right)K_q\left(\Omega,z\right)\right]\right]\left(\Omega\right)\Big]\Big]\left(\Omega\right)\\
&+\frac{2}{4}i\Omega\frac{\epsilon_0}{4}\left[\exp\left(i\phi_m\left(\Omega,z\right)\right)+i\phi_0\left(z\right)\right]^*K_m\left(\Omega,z\right)\sum_{n,p,q}\\
&\int\int\left[\widehat{\boldsymbol{\mathcal{E}}}_m^*\left(\Omega_0,x,y,z\right)\cdot\widehat{\boldsymbol{\mathcal{E}}}_n\left(\Omega_0,x,y,z\right)\widehat{\boldsymbol{\mathcal{E}}}_p^*\left(\Omega_0,x,y,z\right)\cdot\widehat{\boldsymbol{\mathcal{E}}}_q\left(\Omega_0,x,y,z\right)\right]\mathrm{d}x\mathrm{d}y\\
&\mathcal{F}\Big[\mathcal{F}^{-1}\left[\tilde{G}_n\left(\Omega,z\right)K_n\left(\Omega,z\right)\right]\mathcal{F}^{-1}\Big[\tilde{\chi}^{(3)}_{mnpq}\left(\Omega\right)\\
&\mathcal{F}\left[\mathcal{F}^{-1}\left[\tilde{G}_p\left(\Omega,z\right)K_p\left(\Omega,z\right)\right]^*\mathcal{F}^{-1}\left[\tilde{G}_q\left(\Omega,z\right)K_q\left(\Omega,z\right)\right]\right]\left(\Omega\right)\Big]\Big]\left(\Omega\right).
\end{aligned}\tag{4.3}$$

This goes to show that it is always possible to change the dispersion by applying a phase-shift only dependent on z to the final solution. It is only the relative phase that matters once third harmonic generation is neglected, and the equation is thus Gauge invariant with respect to phase in the observables such as intensity, power, photon number and so on.

4.1 Reduction without Tapering and Mode Profile Dispersion

In [62], Eq. (4.4) is printed,

$$\begin{aligned}
&\frac{\partial}{\partial z}A_p\left(z,t\right)=\\
&i\left(\beta_0^{(p)}-\beta_0\right)A_p\left(z,t\right)-\left(\beta_1^{(p)}-\beta_1\right)\frac{\partial}{\partial t}A_p\left(z,t\right)+i\sum_{n\leq 2}\frac{\beta_n^{(p)}}{n!}\left(i\frac{\partial}{\partial t}\right)^n A_p\left(z,t\right)+i\frac{n_2\omega_0}{c}\sum_{n,l,m}\Big\{\\
&\left(1+i\tau^{(1)}_{plmn}\frac{\partial}{\partial t}\right)Q^{(1)}_{plmn}\left(\omega_0\right)2A_l\left(z,t\right)\int R\left(t'\right)A_m\left(z,t-t'\right)A_n^*\left(z,t-t'\right)\mathrm{d}t'\\
&\left(1+i\tau^{(2)}_{plmn}\frac{\partial}{\partial t}\right)Q^{(2)}_{plmn}\left(\omega_0\right)A_l^*\left(z,t\right)\int R\left(t'\right)A_m\left(z,t-t'\right)A_n\left(z,t-t'\right)\exp\left(i2\omega_0t'\right)\mathrm{d}t'\Big\}
\end{aligned}\tag{4.4}$$

$$Q^{(1)}_{plmn}\left(\omega\right)=\frac{\epsilon_0^2n_0^2c^2}{12}\int\int\frac{\left[\boldsymbol{F}_p^*\left(\omega\right)\cdot\boldsymbol{F}_l\left(\omega\right)\right]\left[\boldsymbol{F}_m\left(\omega\right)\cdot\boldsymbol{F}_n^*\left(\omega\right)\right]}{N_p\left(\omega\right)N_l\left(\omega\right)N_m\left(\omega\right)N_n\left(\omega\right)}\mathrm{d}x\mathrm{d}y$$

$$
\begin{aligned}
Q_{plmn}^{(2)}(\omega) &= \frac{\epsilon_0^2 n_0^2 c^2}{12} \int\int \frac{\left[\boldsymbol{F}_p^*(\omega)\cdot\boldsymbol{F}_l^*(\omega)\right]\left[\boldsymbol{F}_m(\omega)\cdot\boldsymbol{F}_n(\omega)\right]}{N_p(\omega)\,N_l(\omega)\,N_m(\omega)\,N_n(\omega)}\mathrm{d}x\mathrm{d}y \\
\tau_{plmn}^{(1,2)} &= \frac{1}{\omega_0} + \frac{\partial}{\partial\omega}\left[\ln\left(Q_{plmn}^{(1,2)}(\omega)\right)\right] \\
R(t) &= (1-f_R)\,\delta(t) + \frac{3}{2} f_R h(t)
\end{aligned}
$$

using the notation of the paper, where $f_R = 0.18$. This equation is an envelope equation, in which tapering and mode profile dispersion has been neglected. It also uses the forward definition of the Fourier transform, instead of the one used to derive the result. Since Eq. (4.7) is written as an equation going from the frequency domain to the frequency domain, we can directly use the forward Fourier transform definitions,

$$
\mathcal{F}\left[G(t)\right] = \tilde{G}(\Omega) = \int_{-\infty}^{\infty} G(t)\exp\left(i\Omega t\right)\,\mathrm{d}t \tag{4.5}
$$

$$
\mathcal{F}^{-1}\left[\tilde{G}(\Omega)\right] = G(t) = \frac{1}{2\,\pi}\int_{-\infty}^{\infty} \tilde{G}(\Omega)\exp\left(-i\Omega t\right)\,\mathrm{d}\Omega, \tag{4.6}
$$

in place of the old ones. Neglecting tapering and mode profile dispersion in Eq. (4.7), amounts to dropping the z dependence in the wave number and setting $K_m(\Omega, z) = 1$. But first it is necessary to go through the interaction picture transform. In the notation here, this amounts to performing the differentiation on the left side in order to move the phase term down,

$$
\begin{aligned}
&\frac{\partial}{\partial z}\tilde{G}_m(\Omega,z) = i\frac{\partial\left[\phi^*(\Omega,z)+\phi_0(z)\right]}{\partial z}\tilde{G}_m(\Omega,z) \\
&+\frac{1}{4}i\Omega\frac{\epsilon_0}{4}\sum_{n,p,q} \\
&\int\int\left[\widehat{\boldsymbol{\mathcal{E}}}_m^*(\Omega_0,x,y,z)\cdot\widehat{\boldsymbol{\mathcal{E}}}_n^*(\Omega_0,x,y,z)\,\widehat{\boldsymbol{\mathcal{E}}}_p(\Omega_0,x,y,z)\cdot\widehat{\boldsymbol{\mathcal{E}}}_q(\Omega_0,x,y,z)\right]\mathrm{d}x\mathrm{d}y \\
&\mathcal{F}\Big[\mathcal{F}^{-1}\left[\tilde{G}_n(\Omega,z)\right]^*\mathcal{F}^{-1}\Big[\tilde{\chi}_{mnpq}^{(3)}(\Omega) \\
&\mathcal{F}\left[\mathcal{F}^{-1}\left[\tilde{G}_p(\Omega,z)\right]\mathcal{F}^{-1}\left[\tilde{G}_q(\Omega,z)\right]\right](\Omega)\Big]\Big](\Omega) \\
&+\frac{2}{4}i\Omega\frac{\epsilon_0}{4}\sum_{n,p,q} \\
&\int\int\left[\widehat{\boldsymbol{\mathcal{E}}}_m^*(\Omega_0,x,y,z)\cdot\widehat{\boldsymbol{\mathcal{E}}}_n(\Omega_0,x,y,z)\,\widehat{\boldsymbol{\mathcal{E}}}_p^*(\Omega_0,x,y,z)\cdot\widehat{\boldsymbol{\mathcal{E}}}_q(\Omega_0,x,y,z)\right]\mathrm{d}x\mathrm{d}y \\
&\mathcal{F}\Big[\mathcal{F}^{-1}\left[\tilde{G}_n(\Omega,z)\right]\mathcal{F}^{-1}\Big[\tilde{\chi}_{mnpq}^{(3)}(\Omega) \\
&\mathcal{F}\left[\mathcal{F}^{-1}\left[\tilde{G}_p(\Omega,z)\right]^*\mathcal{F}^{-1}\left[\tilde{G}_q(\Omega,z)\right]\right](\Omega)\Big]\Big](\Omega)\,.
\end{aligned} \tag{4.7}
$$

Taking the inverse Fourier transform on both sides, inserting the definition of $\phi(\Omega, z)$ from Eq. (3.12), as well as chosing $\phi_0(z) = \int_0^z i\omega_0\hat{\beta}_{11}(z') - \hat{\beta}_{10}(z')$ and applying the

Fourier shift theorem while writing out the inner Fourier transforms, the following is obtained,

$$
\begin{aligned}
&\exp\left(-i\omega_0 t\right)\frac{\partial}{\partial z}G_m\left(t,z\right)=\\
&i\mathcal{F}^{-1}\left[\left[\hat{\beta}_{m0}\left(z\right)-\hat{\beta}_{10}\left(z\right)+\left[\hat{\beta}_{m1}\left(z\right)-\hat{\beta}_{11}\left(z\right)\right]\left(\Omega-\omega_0\right)+\sum_{n=2}^{\infty}\frac{\hat{\beta}_{mn}\left(z\right)}{n!}\left(\Omega-\omega_0\right)^n\right]\tilde{G}_m\left(\Omega,z\right)\right]\\
&+\frac{1}{4}i\omega_0\frac{\epsilon_0}{4}\sum_{n,p,q}\left(1+\frac{i}{\omega_0}\frac{\partial}{\partial t}\right)\\
&\int\int\left[\widehat{\boldsymbol{\mathcal{E}}}_m^*\left(\Omega_0,x,y,z\right)\cdot\widehat{\boldsymbol{\mathcal{E}}}_n^*\left(\Omega_0,x,y,z\right)\widehat{\boldsymbol{\mathcal{E}}}_p\left(\Omega_0,x,y,z\right)\cdot\widehat{\boldsymbol{\mathcal{E}}}_q\left(\Omega_0,x,y,z\right)\right]\mathrm{d}x\mathrm{d}y\\
&\left[G_n\left(t,z\right)\exp\left(-i\omega_0 t\right)\right]^*\mathcal{F}^{-1}\left[\tilde{\chi}^{(3)}_{mnpq}\left(\Omega\right)\right.\\
&\left.\mathcal{F}\left[\exp\left(-i\omega_0 t\right)G_p\left(t,z\right)\exp\left(-i\omega_0 t\right)G_q\left(t,z\right)\right]\left(\Omega\right)\right]\\
&+\frac{2}{4}i\frac{\epsilon_0}{4}\sum_{n,p,q}\omega_0\left(1+\frac{i}{\omega_0}\frac{\partial}{\partial t}\right)\\
&\int\int\left[\widehat{\boldsymbol{\mathcal{E}}}_m^*\left(\Omega_0,x,y,z\right)\cdot\widehat{\boldsymbol{\mathcal{E}}}_n\left(\Omega_0,x,y,z\right)\widehat{\boldsymbol{\mathcal{E}}}_p^*\left(\Omega_0,x,y,z\right)\cdot\widehat{\boldsymbol{\mathcal{E}}}_q\left(\Omega_0,x,y,z\right)\right]\mathrm{d}x\mathrm{d}y\\
&G_n\left(t,z\right)\exp\left(-i\omega_0 t\right)\mathcal{F}^{-1}\left[\tilde{\chi}^{(3)}_{mnpq}\left(\Omega\right)\right.\\
&\left.\mathcal{F}\left[\left[G_p\left(t,z\right)\exp\left(-i\omega_0 t\right)\right]^*G_q\left(t,z\right)\exp\left(-i\omega_0 t\right)\right]\left(\Omega\right)\right]\quad .
\end{aligned}
\tag{4.8}
$$

Next we apply the convolution theorem to the inner Fourier transforms, perform the inverse Fourier transform on the dispersion term and move around the $\exp\left(i\omega_0 t\right)$ terms to conclude they all vanish,

$$
\begin{aligned}
&\frac{\partial}{\partial z}G_m\left(t,z\right)=\\
&i\left[\hat{\beta}_{m0}\left(z\right)-\hat{\beta}_{10}\left(z\right)+i\left[\hat{\beta}_{m1}\left(z\right)-\hat{\beta}_{11}\left(z\right)\right]\frac{\partial}{\partial t}+i\sum_{n=2}^{\infty}\frac{\hat{\beta}_{mn}\left(z\right)}{n!}\left(i\frac{\partial}{\partial t}\right)^n\right]G_m\left(t,z\right)\\
&+\frac{1}{4}i\omega_0\frac{\epsilon_0}{4}\sum_{n,p,q}\left(1+\frac{i}{\omega_0}\frac{\partial}{\partial t}\right)\\
&\int\int\left[\widehat{\boldsymbol{\mathcal{E}}}_m^*\left(\Omega_0,x,y,z\right)\cdot\widehat{\boldsymbol{\mathcal{E}}}_n^*\left(\Omega_0,x,y,z\right)\widehat{\boldsymbol{\mathcal{E}}}_p\left(\Omega_0,x,y,z\right)\cdot\widehat{\boldsymbol{\mathcal{E}}}_q\left(\Omega_0,x,y,z\right)\right]\mathrm{d}x\mathrm{d}y\\
&G_n^*\left(t,z\right)\int\chi^{(3)}_{mnpq}\left(t'\right)G_p\left(t-t',z\right)G_q\left(t-t',z\right)\exp\left(i2\omega_0 t'\right)\mathrm{d}t'\\
&+\frac{2}{4}i\frac{\epsilon_0}{4}\sum_{n,p,q}\omega_0\left(1+\frac{i}{\omega_0}\frac{\partial}{\partial t}\right)\\
&\int\int\left[\widehat{\boldsymbol{\mathcal{E}}}_m^*\left(\Omega_0,x,y,z\right)\cdot\widehat{\boldsymbol{\mathcal{E}}}_n\left(\Omega_0,x,y,z\right)\widehat{\boldsymbol{\mathcal{E}}}_p^*\left(\Omega_0,x,y,z\right)\cdot\widehat{\boldsymbol{\mathcal{E}}}_q\left(\Omega_0,x,y,z\right)\right]\mathrm{d}x\mathrm{d}y
\end{aligned}
$$

$$G_n(t,z)\int \chi^{(3)}_{mnpq}(t')\,G^*_p(t-t',z)\,G_q(t-t',z)\,\mathrm{d}t' \quad . \tag{4.9}$$

If we now compare to Eq. (4.4), we see that we are almost done. The final pieces are the frequency dependence of the shock term, $\chi^{(3)}_{mnpq}(t)$ and the prefactor.

As also mentioned in [62], the small frequency dependency introduced to the shock term cannot be justified mathematically, but is merely supported by empirical evidence. Thus no more time will be spent on that. As a side note to that, it should be immediatly obvious that the change does not conserve the photon number, which makes checks of the numerical implementation problematic.

The nonlinear response, $\chi^{(3)}_{mnpq}(t)$ generally depends on the spatial direction of the modes and fields involved, as evident by its tensor form. Ignoring this in Eq. (3.35), approximating $f_b = 0$ and inserting it so that only the time response is retained gives $\chi^{(3)}_{xxxx}(t)\left[(1-f_a)\,\delta(t) + f_a h_a(t)\right]$, corresponding to the expression in [62].

Lastly, there is the prefactor, which is then $\frac{3}{16}\omega_0\chi^{(3)}_{xxxx}\epsilon_0$. In experiments, it is the nonlinear refractive index change, n_2, and not $\chi^{(3)}_{xxxx}$ that is measured. The relationship between them is

$$n_2 = \frac{3\mathrm{Re}\left(\chi^{(3)}_{xxxx}\right)}{8n_0}\frac{2}{\epsilon_0 n_0 c} = \frac{3}{4}\frac{\mathrm{Re}\left(\chi^{(3)}_{xxxx}\right)}{n_0^2 c\epsilon_0} \tag{4.10}$$

according to [2]. Inserting this, the derived equation perfectly recovers the expression by Poletti in Eq. (4.4).

To avoid potential confusion, I will spend a few words on the fractions in the prefactors. The prefactors in the result of chapter 3 or Eq. (4.9) came about as follows. The first quarter came from the choice of normalisation which resulted from demanding that $|A(z,t)|^2$ should be the instantaneous power. The second quarter, came from going to the envelope equation. We saw that this gave four terms, of which three had the usual Kerr response, $A|A|^2$, and the fourth was third harmonic generation. This yielded the 3/4 factor that is almost always seen in litterature. However, we also saw that not all three of these terms had the same Raman response. One term had a Raman response at twice the carrier frequency. The Raman response is shifted in frequency so far from the exciting field that it is essentially zero. It is usually neglected completely, which is valid for narrow sources. Hence the relative Raman strength, f_a, is only 2/3 of what it should be. Of course both n_2 and f_a values are based on measurements. Usually done by fitting results to some theory and specific equation. These values then depend on the specific equations used, either including or excluding the double rotating Raman term leads to values that include or dont include the factor 2/3, corresponding to measurements with results at either $f_a = 0.3$ or $f_a = 0.18$.

4.2 The implemented version of the GNLSE

The GNLSE as written in Eq. (4.3) can be reduced by neglecting the double rotating Raman term, and assuming the transverse integral is independant of the position of the complex conjugate. This yields the equation implemented and solved in the remainder of the thesis.

$$\begin{aligned}
&\frac{\partial}{\partial z}\left[\left[\exp\left(i\phi_m\left(\Omega,z\right)+i\phi_0\left(z\right)\right)\right]^*\tilde{G}_m\left(\Omega,z\right)\right]=\\
&\frac{3}{4}i\Omega\frac{\epsilon_0}{4}\left[\exp\left(i\phi_m\left(\Omega,z\right)\right)+i\phi_0\left(z\right)\right]^*K_m\left(\Omega,z\right)\sum_{n,p,q}\\
&\int\int\left[\widehat{\boldsymbol{\mathcal{E}}}_m^*\left(\Omega_0,x,y,z\right)\cdot\widehat{\boldsymbol{\mathcal{E}}}_n\left(\Omega_0,x,y,z\right)\widehat{\boldsymbol{\mathcal{E}}}_p^*\left(\Omega_0,x,y,z\right)\cdot\widehat{\boldsymbol{\mathcal{E}}}_q\left(\Omega_0,x,y,z\right)\right]\mathrm{d}x\mathrm{d}y\\
&\mathcal{F}\Big[\mathcal{F}^{-1}\left[\tilde{G}_n\left(\Omega,z\right)K_n\left(\Omega,z\right)\right]\mathcal{F}^{-1}\Big[\tilde{\chi}^{(3)}_{mnpq}\left(\Omega\right)\\
&\mathcal{F}\left[\mathcal{F}^{-1}\left[\tilde{G}_p\left(\Omega,z\right)K_p\left(\Omega,z\right)\right]^*\mathcal{F}^{-1}\left[\tilde{G}_q\left(\Omega,z\right)K_q\left(\Omega,z\right)\right]\right]\left(\Omega\right)\Big]\Big]\left(\Omega\right).
\end{aligned}\tag{4.11}$$

Chapter 5

Numerical Implementation and Test

Solving Eq. (4.11) numerically in an efficient manner is no easy feat. In this chapter the core parts of the implementation will be discussed. The strategy for solving the GNLSE is to first evaluate the transverse parts of the fields at different frequencies to obtain dispersion and overlap integrals once, and then using those again and again when solving Eq. (4.11) in matlab. The chapter is sctructured with a section dedicated to each of the finite element calculations leading to the dispersion and overlap integrals, the implementation of Eq. (4.11) in matlab and testing the implementation.

5.1 Dispersion and Overlap Integrals

The first step in solving Eq. (3.62) or any of the versions based upon it, is to know the propagation constant, and the transverse overlap integrals. For step index fibers it is possible to obtain exact theoretical expressions and to evaluate and use those directly in the calculation. For PCF fibers it is a different matter, as there are no general theoretical solution available at every frequency for any choice of pitch and pitch to hole ratio. For this reason, it is necessary to calculate the propagation constant for all involved modes numerically at a set of frequencies. This process is quite involved and can take a long time per frequency. Given that it is not practical to do it for every frequency in the fine grid used when solving the GNLSE. The solution is to calculate the values at a more coarse grid of frequencies and then interpolate that to the grid used when solving the GNLSE. The same is true for the overlap integrals.

The way all calculations are done in COMSOL is to first set up the structure of interest. An example can be seen in Fig. 5.1 for 7 a PCF with 7 rings. The built in COMSOL module `Electromagnetic Waves, Frequency Domain (emw)` that solves the fully vec-

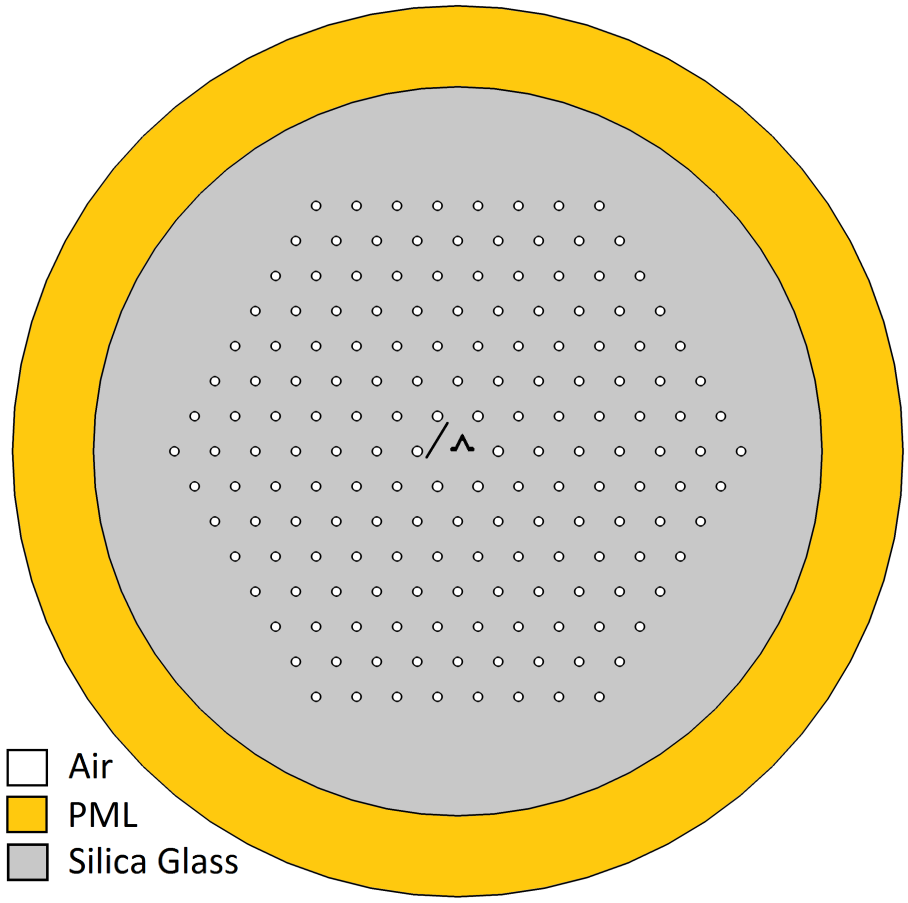

Figure 5.1: Image from the COMSOL of the structure. The pitch, Λ, is the distance between nearest neighbort air holes and is marked in the figure. The other important parameters are the number of hole rings and their diameter, d.

torial Helmholtz equation is used, with a modified Perfectly Matched Layer (PML). The expressions shown in [1] are used in the place of the standard ones used in the default PML in COMSOL. In practice, this is done through appropriate modifications to the relative permeability and permitivity. The values used for silica were $\alpha = 10$, $p = 2$ and a PML thickness of $10\,\mu$m. For materials guiding at longer wavelengths, such as chalgogenides, it is necessary to increase the PML thickness accordingly. Otherwise reflected light gives rise to interference, which in turn makes the overlap integrals oscillate with frequency.

In order to find the refractive index of the mode of interest, it is necessary to provide a good starting guess for the COMSOL solver for any frequency. One way of doing this is to start at either high or low frequencies and then go through them one at a time, using the guess based on the previous solution. In the calculation shown in this thesis a simple forward difference scheme was used. If one starts from large frequencies, the

modes will generally be almost entirely confined in the silica material, which means the refractive index is that of silica. This can be used as a good initial guess. The downside to this method is that it can be problematic to know if the mode of interest such as the fundamental mode, is among those provided by COMSOL based on the guess. Instead as was the case here, it was used that the fundamental mode always has a better power (Poynting vector) overlap with the core region than the previous solution when starting at low frequencies. This is used to either accept a given set of solutions or expand the search for modes dynamically while sweeping the list of frequencies. The Sellmeier equation used for silica glass is

$$n_{Si}^2 = 1 + \frac{0.6965325}{1 - 4.368309 \cdot 10^{-15} \frac{f^2}{c^2}} + \frac{0.4083099}{1 - 1.394999 \cdot 10^{-14} \frac{f^2}{c^2}} + \frac{0.8968766}{1 - 97.93399 \cdot 10^{-12} \frac{f^2}{c^2}} \quad (5.1)$$

with f being the frequency and c the speed of light in SI units, [42, 58].

At every step it is necessary to calculate the transverse overlap integrals. One could extract the full field solutions from COMSOL onto some grid and then perform the integral. The downside to this method is that the precision inherent to any finite element solution is lost when the basis functions used to find that solution are not used. On top of this, the precision will always go down when interpolating onto a different grid. A way to get around this is to perform the integrals directly in COMSOL using the basis functions internal to COMSOL, and thus retaining the full numerical precision. This is basically a matrix multiplication of the solution vector with itself through some weight matrix arising from the grid. Being simple matrix multiplication it should be rather fast. Unfortunately there is no good direct way of doing this in COMSOL. Instead a second solver step that solves the overlap integral was added to the solver. This step took about four times as long as the actual solution for just a few modes, due to the many overlap permutations in the transverse overlap integral. The overlap was not evaluated in the air holes as the nonlinear refractive index in air is much smaller than that of silica, and can safely be assumed to not contribute. In the same step the integral of the Poynting vector was used to find the normalization for the electric fields.

The overlap integrals were interpolated directly from the coarse mesh to the fine mesh. From the complex refractive index the corresponding complex propagation constant was calculated. The real part of the propagation constant on the fine mesh was constructed by interpolating the propagation constant on the coarse mesh and subtracting zero'th and the first order derivative at the pump. The first order derivative accurate to the fourth order was found by using the central finite difference scheme on the coarse grid. The imaginary part corresponding to confinement loss was then interpolated and added, in addition to the material loss. For silica glass the loss model provided in [56] was used. The model is

$$\beta_{Loss,Si}(\lambda) = -\frac{1}{20\log 10(e)} \frac{A_{Ray}}{\lambda^4} + A_{uv} \exp\left(\frac{\lambda_{uv}}{\lambda}\right) + A_{ir} \exp\left(-\frac{\lambda_{ir}}{\lambda}\right) \quad (5.2)$$

where scattering due to impurities and surface imperfections has been neglected. The coefficients are $A_{Ray} = 1.3\,\mathrm{dB\,km^{-1}}\,\mu\mathrm{m}^4$, $A_{uv} = 10^{-3}\,\mathrm{dB\,km^{-1}}$, $A_{ir} = 6\,10^{11}\,\mathrm{dB\,km^{-1}}$,

$\lambda_{uv} = 4.67\,\mu$m and $\lambda_{ir} = 47.8\,\mu$m. In order to prevent numerical noise due to poor resolution at the shortest timescales corresponding to the highest frequencies, a further extremely high loss was added to the highest frequencies on the fine grid.

5.2 Implementation in Matlab

Instead of going through the whole code, the core parts of the solver will be explained, with examples. This includes the custom Runge-Kutta-Fehlberg ordinary differential equation solver, the core function call where all the Fourier transforms are carried out and the local error method employed to adapt the step size. These, together with linear interpolation of the reduced propagation constant discussed in the previous section and the linear interpolation of the overlap integrals to the current position in a taper cover the most important parts of the solver. All these steps are carried out on a Graphical Processing Unit (GPU), to take advantage of the larger number of cores (processing power) and thus faster Fast Fourier Transform (FFT). The core code can run both on the CPU, and on the GPU. Matlab automatically picks one or the other based on the location of the memory, and gives an error if the function calls do not exist for the choice. Hence all variables must be transferred to the GPU memory before execution of the stepper that makes up the core of the solver, and they must be transferred back before saving afterwards.

Listing 5.1: The Runge-Kutta-Fehlberg solver used to solve the GNLSE.

```
function [PulseCoarse,PulseFine]=InteractionStepFifthOrder(...
    PulseFD,R,beta,gamma,dz,Nmodes,MPD)
TEMP=ifft(ifftshift(PulseFD.*MPD,1),[],1);
PulseTDn=permute(repmat(TEMP,[1,1,Nmodes,Nmodes,Nmodes]),[1,3,2,4,5]);
PulseTDpq=permute(repmat(bsxfun(@times,TEMP,permute(conj(TEMP),...
    [1,3,2])),[1,1,1,Nmodes,Nmodes]),[1,4,5,2,3]);
k1=dz.*sum(sum(sum(gamma.*NonlinOperatorMM(PulseTDn,PulseTDpq,R),5),4),3);

dzk=1/4*dz;
TEMP=ifft(ifftshift((PulseFD+1/4*k1).*MPD.*exp(1i*conj(beta)*dzk),1),[],1);
PulseTDn=permute(repmat(TEMP,[1,1,Nmodes,Nmodes,Nmodes]),[1,3,2,4,5]);
PulseTDpq=permute(repmat(bsxfun(@times,TEMP,permute(conj(TEMP),...
    [1,3,2])),[1,1,1,Nmodes,Nmodes]),[1,4,5,2,3]);
k2=dz.*exp(-1i*(beta)*dzk).*sum(sum(sum(gamma.*...
    NonlinOperatorMM(PulseTDn,PulseTDpq,R),5),4),3);

%...
%k3 to k6 defined in the same way, with different dzk and coefficients.
%...

PulseCoarse=exp(1i*conj(beta)*dz).*...
    (PulseFD+25/216*k1+1408/2565*k3+2197/4104*k4-0.2*k5);
PulseFine=exp(1i*conj(beta)*dz).*...
```

```
24      (PulseFD+16/135*k1+6656/12825*k3+28561/56430*k4-9/50*k5+2/55*k6);
25  end
```

Listing 5.2: The core function call including all the Fourier transforms.

```
1  function Aout=NonlinOperatorMM(PulseTDn,PulseTDpq,R)
2  Aout=fftshift(fft(PulseTDn.*...
3       ifft(ifftshift(R.*fftshift(fft(PulseTDpq,[],1),1),1),[],1),[],1),1);
4  end
```

Eq. (4.11) is the equation solved, which is the one implemented in Listing 5.1 and 5.2. In the RKF solver, Listing 5.1, line 3 contain the FFT that brings the pulse to the time domain. Line 4 and 5 contain the multidimensional expansion that brings the 2D pulse matrix to a 5D matrix containing all the possible combinations between the different modes. Line 5 furthermore contain the multiplication between the p and q modes. The FFT's in Listing 5.2 should be self explanatory. `R` contains the multidimensional Raman and Kerr responses as described in Eq. (3.35). `GammaOI` contains the whole prefactor and the `MPD` variable is the mode profile dispersion correction.

Listing 5.3: The loop that steps through the fiber finding the solution at every step.

```
1  while gpuLtot<Ltarget
2  %...
3  %Interpolate overlap integrals, beta and mode profile dispersion (MPD) to
4  %match current position in taper.
5  %...
6
7  %Perform the step
8  [PulseCoarse,PulseFine]=InteractionStepFifthOrderMM_IP_MPD(...
9      gpuPulse,gpuR,gpubeta,gammaOI,gpudz,gpuNmodes,MPD);
10
11 %Calculate the local error using the normalized L^2 Norm
12 PNErrorLocal=sum(sum(abs(PulseCoarse-PulseFine).^2))/(gpuNt*gpuNmodes)^2;
13
14 %Decide wether to accept or reject step based on error
15 if PNErrorLocal≥2*gpuMaxRelError
16     %Reject step -> Redo step (reset step number, half stepsize)
17     n1=n1-1;
18     gpudz=gpudz/2;
19 else
20     %Accept step -> Update current position, save stepping data.
21     gpuLtot=gpuLtot+gpudz;
22     zlist(gather(n1)+1)=gather(gpuLtot);
23     PNErrorL(gather(n1)+1,1)=gather(PNErrorLocal);
24     %...
25     % CODE FOR SAVING DATA at the points specified
26     %...
```

```
27      gpuPulse=PulseFine;
28      if PNErrorLocal≤gpuMaxRelError/2
29          %Accept step, but increase step size.
30          gpudz=gpudz*1.05;
31      elseif PNErrorLocal≥gpuMaxRelError
32          %Accept step, but decrease step size.
33          gpudz=gpudz/1.05;
34      else
35          %Accept step, unchanged step size.
36      end
37      %Impose a minimum step size
38      gpudz=min(gpudz,gpuStepSizeMaxLimit);
39  end
40  end
```

In Listing 5.3 the stepper that steps through a full fiber is shown, with emphasis on the local error method that is employed to adapt the step size dynamically. This follows the method suggested in [27,64] with a slight difference. Instead of performing multiple steps to estimate the local error, the fourth and fifth order accurate solutions provided by the RKF method is compared and used to estimate the local error. The local error estimation is based on

$$LE = \frac{\sum_k \left| \tilde{A}_{calc}\left[k\right] - \tilde{A}_{true}\left[k\right] \right|^2}{N_t^2 N_{modes}^2} \approx \frac{\sum_k \left| \tilde{A}_{Coarse}\left[k\right] - \tilde{A}_{Fine}\left[k\right] \right|^2}{N_t^2 N_{modes}^2} \tag{5.3}$$

where coarse and fine refer to the fourth and fifth order solutions in the RKF method. If the local error is more than twice the target, `gpuMaxRelError`, the step is rejected and the whole step is redone with half the step size. If it is less half of `gpuMaxRelError`, the step is increased by a factor. If it is between one and two times `gpuMaxRelError`, it is decreased by the same factor. A good choice for this factor was found by trial and error to be around 1.05. The method suggested in [23], to use the photon number as an indicator of error was also tried out, but was abandoned due to poor results.

It is important to point out the importance of imposing a maximum step size, as seen in the second last line in 5.3. In Fig. 5.2 the total error calculated as the difference to the true solution is shown as a function of propagation with different local error goals. The test is performed for a fiber in which soliton fission takes place at 10% propagation. The curves with the highest local error target follow each other the longest. This is because the initial step size is low, and is allowed to increase freely at a fixed exponential rate at the beginning, until the error goal is reached. When the error goal is reached, the step size is limited and the global error increases much slower. This happens earlier and earlier as LE is decreased, and even forces the step size to initially decrease for the lowest values of LE. In the last 90% of the fiber, the rate of error accumulation is almost constant. The last two simulations, denoted with `@10%` and `@20%` initially has the lowest local error goal, $LE = 10^{-18}$, but after either 10% or 20% propagation, the error goal is increased to $LE = 10^{-10}$. This shows how the initial stage of SPM can, for a relatively low 10%

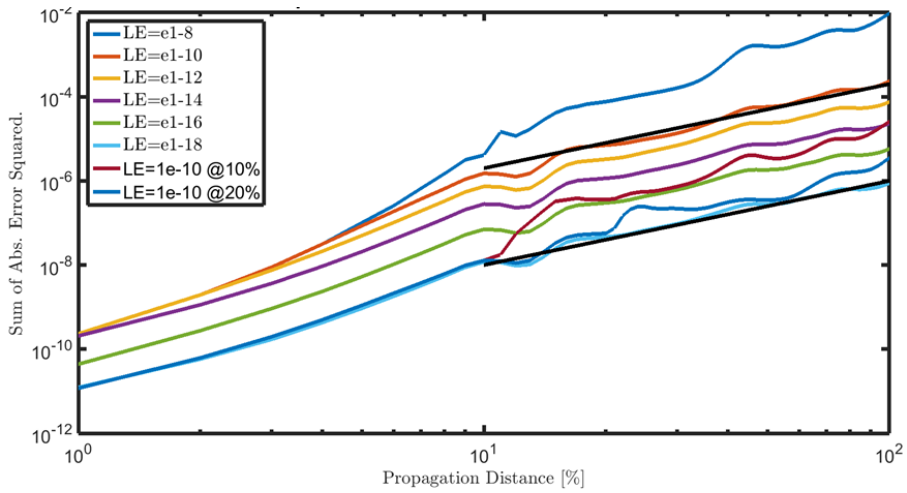

Figure 5.2: Figure showing the global error as a function of propagation distance with different local error goals. The final two line show what happen when the LE is changed in the middle of the simulation from $LE = 10^{-18}$ to $LE = 10^{-10}$, either right before soliton fission (10% propagation), or right after (20% propagation). The black lines are parallel visual aids.

increase in the number of total steps taken, be limited to significantly decrease the final global error. The limit is usually chosen to be around $100\,\mu$m.

The Raman response is usually measured in the frequency domain while the lorentz model is usually given in the time domain, care should be taken to use the right one of $\tilde{h}_a(\omega)$ and its complex conjugate. The difference here lies in the choice of definition of the Fourier transform. It is also important to use the right normalization for `R` and when plotting, as the Fourier transform in matlab is not normalized.

The initial one photon per mode noise is implemented as described in [8, 73]. On top of this, relative input pulse noise, RIN_{In}, is implemented as a Gaussian variation in the peak power. The exact expression including both types of noise is

$$A_{Noise}(\Omega, 0) = \mathcal{F}\left[A(z=0,t)\left(1+\frac{1}{2}RIN_{In}\right)\right](\Omega) + \exp(i\phi_{rand})\sqrt{\frac{\hbar\Omega}{\mathrm{d}\Omega}} \tag{5.4}$$

where ϕ_{rand} is a uniformly distributed random phase. The peak power variation is quite important for modelling low noise SCG, as in this case the noise dominates the RIN of the generated SC. This is shortly discussed in [17]. In most high power pump systems, such variations will inevitably lead to phase variations in the pump as well, but those are not included here.

5.3 A Few Tests

In this section a few examples of tests performed to validate the code will be given. The first can be seen in Fig. 5.3, and compares a pulse after it has undergone MI to that of the theoretical gain bands. The second test can be seen in Fig. 5.4 and is the case of power transfer between modes for a bifringent fiber as shown in Fig 2(a) in [86]. This comparison was chosen out of convenience, because all necessary values were provided in the paper. The result were also compared down to the last decimal to the results of the same model implemented in [17]. The numerical differences were on the scale of the numerical machine precision.

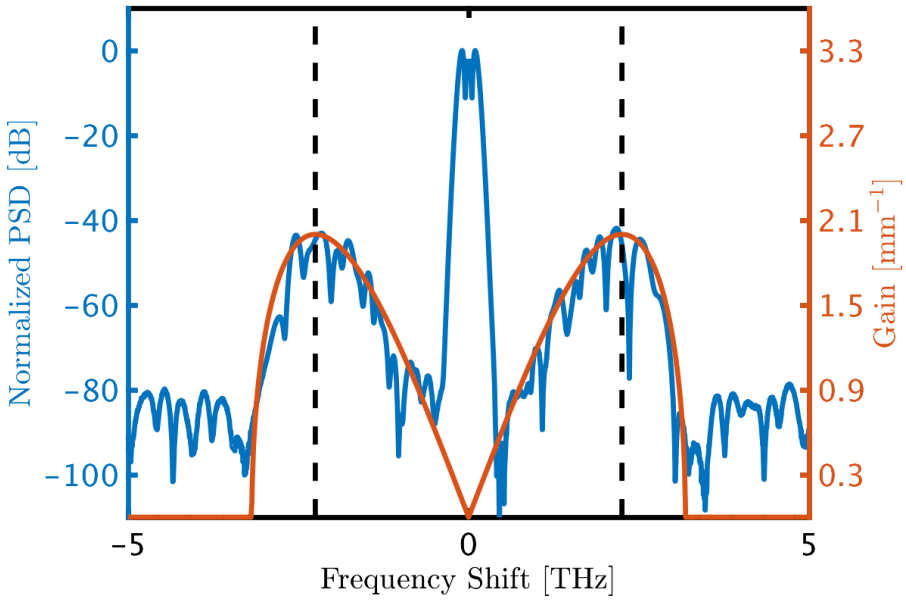

Figure 5.3: Comparison of the implementation described in this chapter (blue line) and the theoretical gain (red line) and maximum gain (dotted black line) given for scalar MI. Input parameters were a Gaussian pulse with a width of 10 ps and 10 kW peak power, in a fiber with $\gamma = 0.1\,\mathrm{W}^{-1}\,\mathrm{m}^{-1}$ and $\beta_2 = -10\,\mathrm{ps}^2\,\mathrm{m}^{-1}$ without Raman scattering.

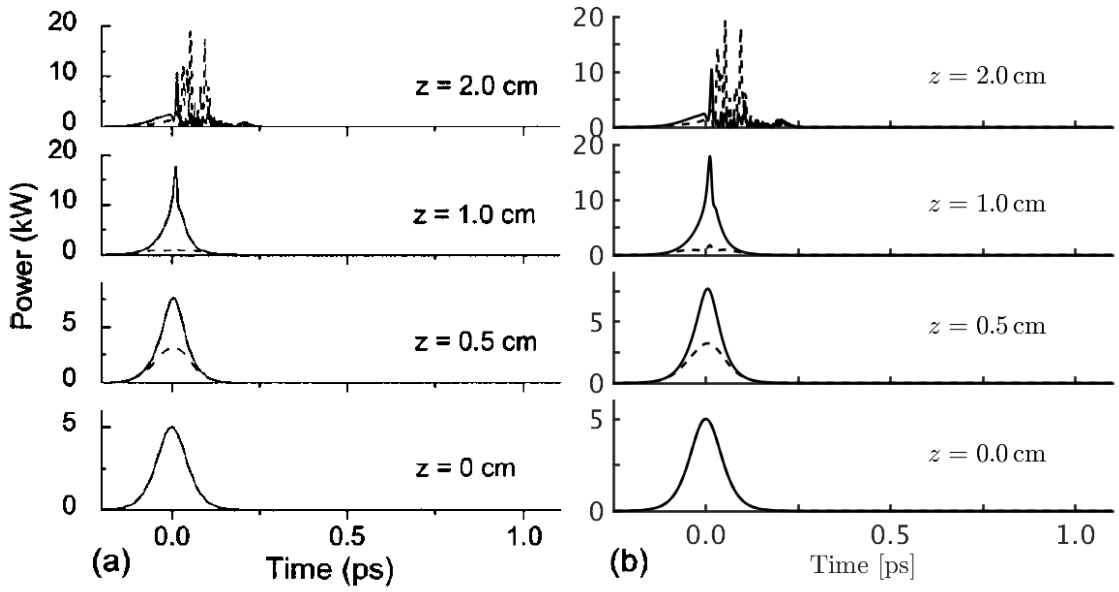

Figure 5.4: Validation of the code running with two polarizations. Direct comparison between the code shown in this chapter (Right Column) to Fig 2(a) in [86] (Left Column). All parameters as described in [86].

Chapter 6

Supercontinuum Relative Intensity Noise Measurements: Theory and Practice

This chapter is a summation on many investigations and consists largely of unpublished results. Some of the methods described have been used in the paper "Polarization noise places severe constraints on coherence of all normal dispersion femtosecond supercontinuum generation".

In this chapter I will go through the different ways of measuring the RIN, discuss their relation and some possible pitfalls in low noise supercontinuum generation. To counterbalance the theory of the previous chapters, I will start from a practical point of view.

As was discussed in chapter 2, we can directly relate the RIN in a supercontinuum source to the background noise in an OCT image. This background noise level is a limiting factor in how deep we can resolve any OCT signal, and plays a strong role in determining the sensitivity. Hence measuring the wavelength dependent RIN and reporting it should be best practice for any SC laser intended for OCT applications. In this chapter we will take an in depth look at the different options for measuring RIN, with special emphasis on some of the pitfalls.

Measuring the RIN can be done in several ways. In the past it has been done as seen in Fig. 6.1 (a), with a variable bandpass filter or in this case monochromator to pick out and scan wavelengths and then recording of the signal with a photodetector. The electrical signal will contain the energy of a single pulse, and can be recorded either through an oscilloscope, [41, 71], or an Electrical Spectrum Analyzer (ESA), [67]. This method has the advantage of being able to record the RIN, and if done with the ESA, can furthermore distinguish between different types of short to middle term stability noise. In section 6.2

the theoretical connection between these will be discussed in detail. As discussed in chapter 2, also the correlation between the different wavelengths in a source is important. A disadvantage of using a method with a spectral filter is that it cannot measure the spectral correlations. For most commercial modulation instability based supercontinuum sources the correlation is however so close to zero that it plays little role.

Another method to measure the RIN is by the use of a spectrometer, which is advantageous as one can use the spectrometer that you would use in the OCT setup to directly measure the noise in the spectral region of interest for that OCT setup. In theory this method can record single spectra and give both RIN and correlations. This is not the case in practice. Most OCT sources operate in at MHz repetition rates, while the best spectrometers work at a few hundred kHz. Thus the spectrometer inherently measure the sum of many pulses which will smear the underlying statistics and make it look normally distributed as predicted by the Central Limit Theorem (CLT). At the edges of a supercontinuum arising from chaotic interaction of redshifting solitons it has been shown that the distribution is non gaussian due to formation of rogue waves, [71], and hence it can be difficult to ascertain if the sum is over a large enough number of pulses to satisfy the condition in the CLT. In the case close to the pump we expect the CLT to be valid, and we can recover the pulse to pulse RIN, RIN_{P2P} from the RIN calculated on an ensemble of a sum of M pulses, RIN_M, by applying a square root factor on the number of pulses,

$$RIN_1(\lambda) = \sqrt{M} RIN_M(\lambda) \tag{6.1}$$

Other, more practical, limitations are related to working with very little signal as the wavelength resolution is usually sub nanometer and the detector has no amplification. If one wish to measure single pulses, trigger timing to get exactly one pulse per readout must be handled with care, and electronic detector and dark noise could be an issue.

A fourth way of measuring noise is by utilizing the relatively new dispersive Fourier transformation method, [15,16,83], which will not be discussed further here except to note that it has been used to successfully characterize SC noise, including spectral correlations, [16]. This method looks very promising, but the necessary very fast electronic equipment, is also expensive.

6.1 Measuring the Relative Intensity Noise

The measurement procedure is as follows: First the output fiber is connected to the Optical Spectrum Analyzer (OSA). Then the desired grating and slit width at the output is picked. The monochromator used here had two gratings. The first (Vendor name: `1-015-800`) is optimized for operation around 800 nm with 150 mm^{-1} while the second (Vendor name: `1-060-1.6`) is optimized for operation around 1600 nm and has 600 mm^{-1}. The calibration can be done by measuring the bandwidth at the desired wavelength as show in Fig. 6.2a. It is evident that the most narrow slit widths begin to truncate the signal. This is not

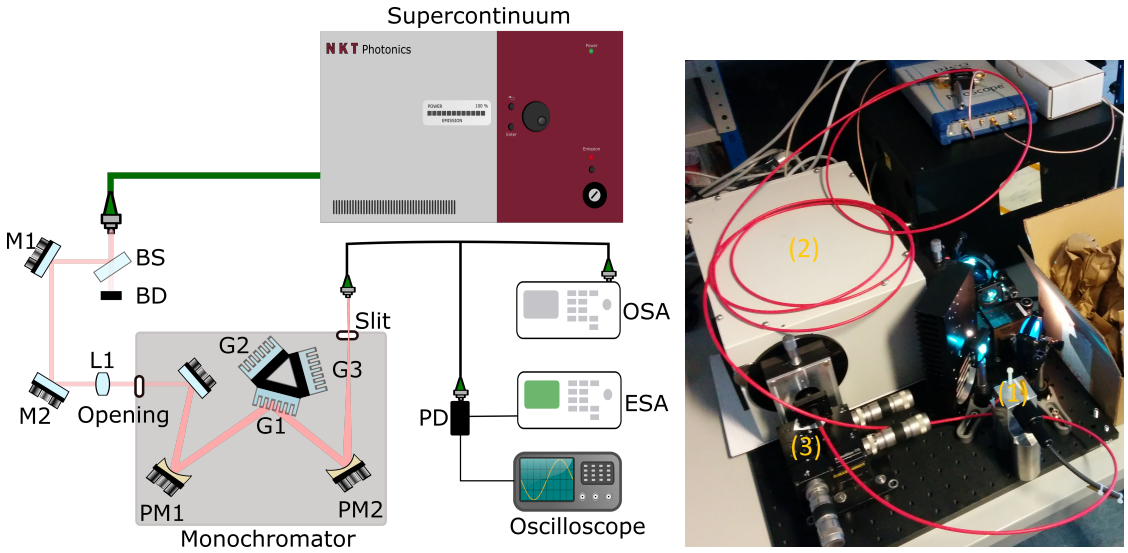

Figure 6.1: Left: Setup to measure noise. M are mirrors, L is a lens, BS is a 10 % beam splitter used to reduce power. Right: Image of the setup in the lab. In the image, (1) denote the input supercontinuum light coming from a NKT Photonics, SuperK Extreme source, (2) is Princeton Spectra Pro 2300i monochromator and (3) is a Ø500 μm core multimode collection fiber mounted on a stage. G1, G2 and G3 are the three gratings installed.

a problem as long as we are only interested in the RIN, with emphasis on the relative part. But working with less than 100 pJ per pulse at this setting means the signal can be hard to detect and is not much larger than the electronic noise. The patch cable is then transfered from the OSA to the photodiode and we can record a series of pulses using either the oscilloscope or ESA.

The electric signal is generated in the photodiode. When a photon is absorbed, a hole electron pair is generated, which is quickly accelerated away from each other due to the electric field. The position of absorption and the evacuation is a diffusion type process, which includes some circuitry. While operating in the linear regime, this process from optical signal to cable voltage can be conveniently described as a convolution between some inherent diode specific diffusion function, $PD\left(t\right)$ and the optical power, $P\left(t\right)$. In practice, most photodiodes are much slower than the supercontinuum pulse duration, which we can use to reduce the equation,

$$U\left(t\right)=\int_{-\infty}^{\infty}PD\left(t_1\right)P\left(t-t_1\right)\left(d\right)t_1\approx\int_{-\infty}^{\infty}PD\left(t-t_1\right)E_0\delta\left(t-t_1\right)\left(d\right)t_1\approx E_0PD\left(t\right) \tag{6.2}$$

In words, on the oscilloscope each pulse will have the same overall shape but will be multiplied with a different peak value. We are only interested in the peak signal of each

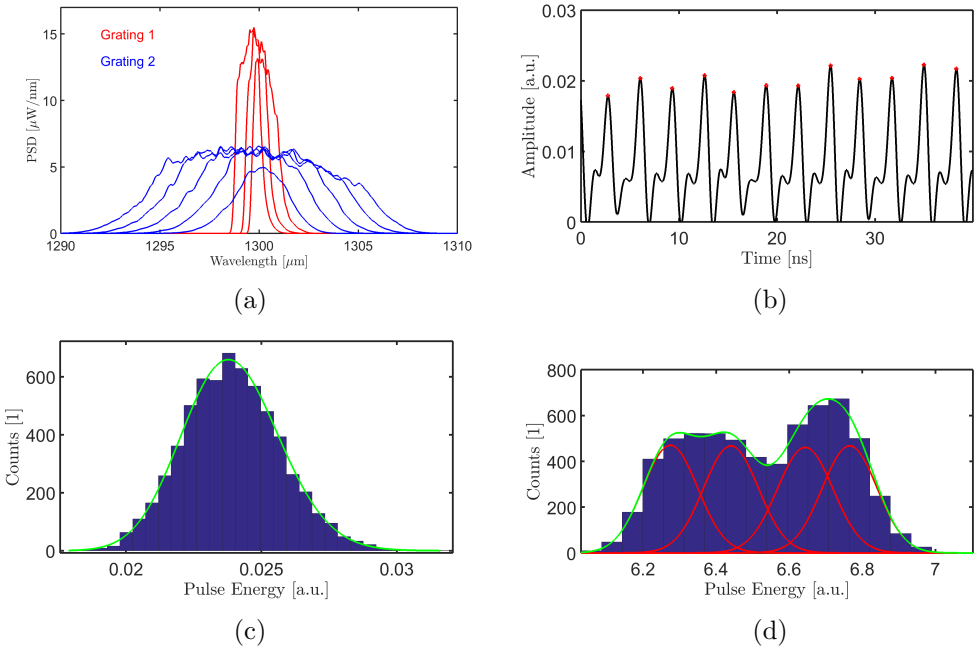

Figure 6.2: (a) Example of characterization of various slit settings of the monochromator. (b) Example of oscilloscope signal at 1450 nm using 12 nm spectral bandwidth with peaks marked with red dots. (c) The statistics of every fourth pulse from the same data set as (b). (d) The bars show the statistics of the full pulse train. The red lines show the Gaussian fits done as as in (c), while the green line show the sum of these.

pulse, as that is directly related to the optical energy in the pulse, E_0, in the filtered bandwidth.

For the case of the oscilloscope, the measurement will be a train of pulses as seen in Fig. 6.2b. In this example, a 320 MHz repetition rate laser source is used with a 500 MHz bandwidth oscilloscope and a D400FC Thorlabs 1 GHz InGaAs detector. It is clear that we cannot estimate the floor in between pulses, and that each pulse in principle could have decaying electronic oscillations that affect the next pulse. Hence caution is necessary, as even an oscilloscope which in theory should have a high enough bandwidth, is shown in practice to not be good enough. If we had used an ESA these problems would be impossible to spot. Not being able to floor the signal properly directly influence the RIN, as the floor is used to estimate the signal average. When attempting to fit skewed distributions where the zero point is important, it can mean the difference between a good and a bad fit, and in the extreme case, failure and success.

Once we have recorded a pulse train and found the peak of every pulse, we can take the mean and standard deviation on the set to obtain the RIN. We would also like to know the distribution to see if it is Gaussian or L-shaped (Rogue Wave dominated). This can

be done either by applying the methods of higher order moments, [74], or by binning the data and plotting it. An example of the latter case is seen in Fig. 6.2c. The green line is a Gaussian fit using the method of Maximum Likelihood Estimation (MLE). As evident they agree quite well, which is also what was expected in the vicinity of the pump.

As discussed previously, spectrometers used in OCT record for a fixed time, usually over many thousands of pulses. As we can see in Eq. (6.1), if we sum more pulses, the RIN is lowered. In some sources this knowledge is used in the following way to reduce the noise: Prior to the nonlinear fiber where the supercontinuum is generated, every pulse is split up into for instance four bream paths. These are then delayed differently, before being merged back together. With the right delay path, the source will seem as if it has four times higher repetition rate, and the noise would be expected to be two times lower. Unfortunately this is not guaranteed to be the case. If the splitting is off by even a small fraction from being perfectly even, the average energy for the four pulses will be different. By demultiplexing the four types of pulses in such a system one can obtain the statistics for each of the four as seen in Fig. 6.2d. A spectrometer would sum over several thousands of pulses, and would only see a normal distribution as dictated by the CLT. But with the pulse to pulse method we can see the underlying statistics of the four pulse types, and since these have different mean values, the method will not reach the full factor two improvement.

The pulse to pulse method described here is the basis for the RIN measurements reported in [17], with the difference that fixed filters were used instead of a monochromator. Let us now turn our attention to the case of the ESA.

6.2 Connection between Oscilloscope and ESA measurements

Using an ESA to measure and analyze long term stability of Continous Wave (CW) lasers has been done for years. Despite this, it might not be intuitively obvious how or why we can measure the pulse to pulse fluctuations of a pulse train with an electrical spectrum analyzer and directly convert it to a RIN value. But nonetheless, in some cases the theory behind is sound. The trick is to know when the method is applicable and when one should use caution, as the ESA method obfuscates the underlying physics and mathematics for most people. Here the theory of conversion will be explained with emphasis on its application within SCG. To the best of my knowledge and quite surprisingly considering that this method has been extensively used, [51], this has not been done for applications within the field of SCG before. The method is briefly discussed in [67], but without a rigorous mathematical proof.

Performing the proof discretely will be advantageous given this is how both a numerical pulse train and the ESA works. First we define the discrete variables in real and Fourier space as $X[n]$ and $Y[k]$. Then we define the Fourier transform, as well as the definitions of the mean, the variance and the kronicker delta of complex variables. The bracket

notation will be used to specify that we are dealing with discrete functions and N is the total number of points.

$$X[n] = \frac{1}{N}\sum_{k=1}^{N} Y[k] \exp\left(i\,2\,\pi\,\frac{n-1}{N}\,(k-1)\right) \tag{6.3}$$

$$Y[k] = \sum_{n=1}^{N} X[n] \exp\left(-i\,2\,\pi\,\frac{k-1}{N}\,(n-1)\right) \tag{6.4}$$

$$\text{Mean}\left(X[n]\right) = \langle X[n]\rangle_n = \frac{1}{N}\left|\sum_{n=1}^{N} X[n]\right| \tag{6.5}$$

$$\text{Var}\left(X[n]\right) = \left\langle \left|\langle X[n]\rangle_n - X[n]\right|^2 \right\rangle_n = B_N\left(\left\langle |X[n]|^2\right\rangle_n - \left|\langle X[n]\rangle_n\right|^2\right) \tag{6.6}$$

$$\delta_{pq} = \frac{1}{N}\sum_{n=1}^{N} \exp\left(i\,2\,\pi\frac{n-1}{N}\,(p-q)\right) \tag{6.7}$$

Note how B_N is the Bessel correction factor for an unbiased estimator.

Let us now see what we can do when we generalize to a full pulse train. To construct an arbitrary electrical pulse train, we assume our pulse train is a sum of some local time shifted function, $\theta\left(t - nT_0\right)$, with a varying amplitude, $g[k]$. The shifting is an integer of T_0 which is the inverse of the repetition frequency. The local function is arbitrary and could for instance be a Gaussian, an impulse response dampened sine or even a square or a triangle function. As previously discussed, the signal, $S[k]$, comes from the photodetector, so the first two choices seem like good candidates. The peak amplitude of each pulse in the train can vary, to simulate that each optical pulse can have a different total energy. There is also the possibility of timing jitter in the laser source and white noise from the electronics, but both are set to zero. A general equation for a signal is,

$$S[k] = \sum_{n=1}^{M} \theta\left[k - n\Delta\right] g[n]\,. \tag{6.8}$$

The Fourier transform is readily calculated through the use of the Fourier shift theorem. This yields,

$$\tilde{S}[m] = \tilde{\theta}[m] \sum_{n=1}^{M} g[n] \exp\left(-i2\pi n\Delta\frac{m-1}{M}\right). \tag{6.9}$$

The ESA measures the PSD, $PSD[m]$, which is defined as

$$PSD[m] = \frac{1}{NT_0}\left|\tilde{S}[m]\right|^2. \tag{6.10}$$

Now we can write up the following equation which links a discrete integration of the PSD to the variance in the peak values, $g[n]$,

$$\begin{aligned} df \sum_{m=1}^{M} \frac{PSD[m]}{\left|\tilde{\theta}[m]\right|^2} &= \frac{1}{N^2 T_0^2} \sum_{m=1}^{M} \sum_{n,p=1}^{N} g[n]\, g^{\star}[p] \exp\left(-i2\pi\Delta \frac{m-1}{M}(n-q)\right) \\ &= \frac{M}{N^2 T_0^2} \sum_{n,p=1}^{N} g[n]\, g^{\star}[p]\, \delta_{nq} \\ &= \frac{M}{N^2 T_0^2} \sum_{n=1}^{N} |g[n]|^2 \\ &= \frac{M}{N T_0^2} < |g[n]|^2 >_n \end{aligned} \tag{6.11}$$

Now we only need to know the mean of the peak values in order to have a mathematical link between the PSD measurement and the RIN. Let us look at the DC term,

$$\frac{PSD[1]}{\left|\tilde{\theta}[1]\right|^2} = \frac{1}{N T_0} \left| \sum_{n=1}^{N} g[n] \right|^2 = \frac{N}{T_0} |< g[n] >_n|^2 \tag{6.12}$$

Inserting the results of Eq. (6.11) and (6.12) into the definition of the pulse to pulse RIN, we obtain the final expression,

$$\begin{aligned} RIN &= \sqrt{\frac{\mathrm{Var}(g[n])}{\mathrm{Mean}(g[n])^2}} = \sqrt{B_N \frac{< |g[n]|^2 >_n - |< g[n] >_n|^2}{|< g[n] >_n|^2}} \\ &= \sqrt{B_N \left(\frac{N}{M} \sum_{m=1}^{M} \frac{PSD[m]}{PSD[1]} \frac{\left|\tilde{\theta}[1]\right|^2}{\left|\tilde{\theta}[m]\right|^2} - 1 \right)}. \end{aligned} \tag{6.13}$$

This result needs a few comments. Starting from the inside and going out, we can see there is a term involving the PSD, $PSD[m]$, normalised to its DC value, $PSD[1]$. Secondly, this term is corrected by the function describing the shape of the pulse, $\tilde{\theta}[m]$ normalised to its own DC value, $\tilde{\theta}[1]$. The product of these two is a corrected PSD, which has a DC value of one and which is periodic with the repetition frequency. In practice, it is difficult to perform the sum, as the highest frequency components would be reduced due to the bandwidth of any measuring apparatus. However, since the terms of the sum repeat, it would be possible to just measure for values of m up to the first harmonic, and then multiply with the total number of harmonics. This factor would be

$$\frac{f_{max}}{f_{rep}} = \frac{T_0}{dt} = \frac{M}{N} \tag{6.14}$$

since the total time window is $dtM = T_0 N$. This exactly cancels out the factor in front of the sum, and we conclude that the sum only has to run up to and excluding the first

harmonic. Since we normalised and corrected the PSD, the first term is guaranteed to be one, which is subtracted by the one in the equation. Since the sum essentially has a term that is now zero, The Bessel correction factor, B_N, can be understod as correcting for this missing entry into the sum by adding the average of all the other entries.

To show an example of how to calculate pulse to pulse noise from a Fourier analysis of the

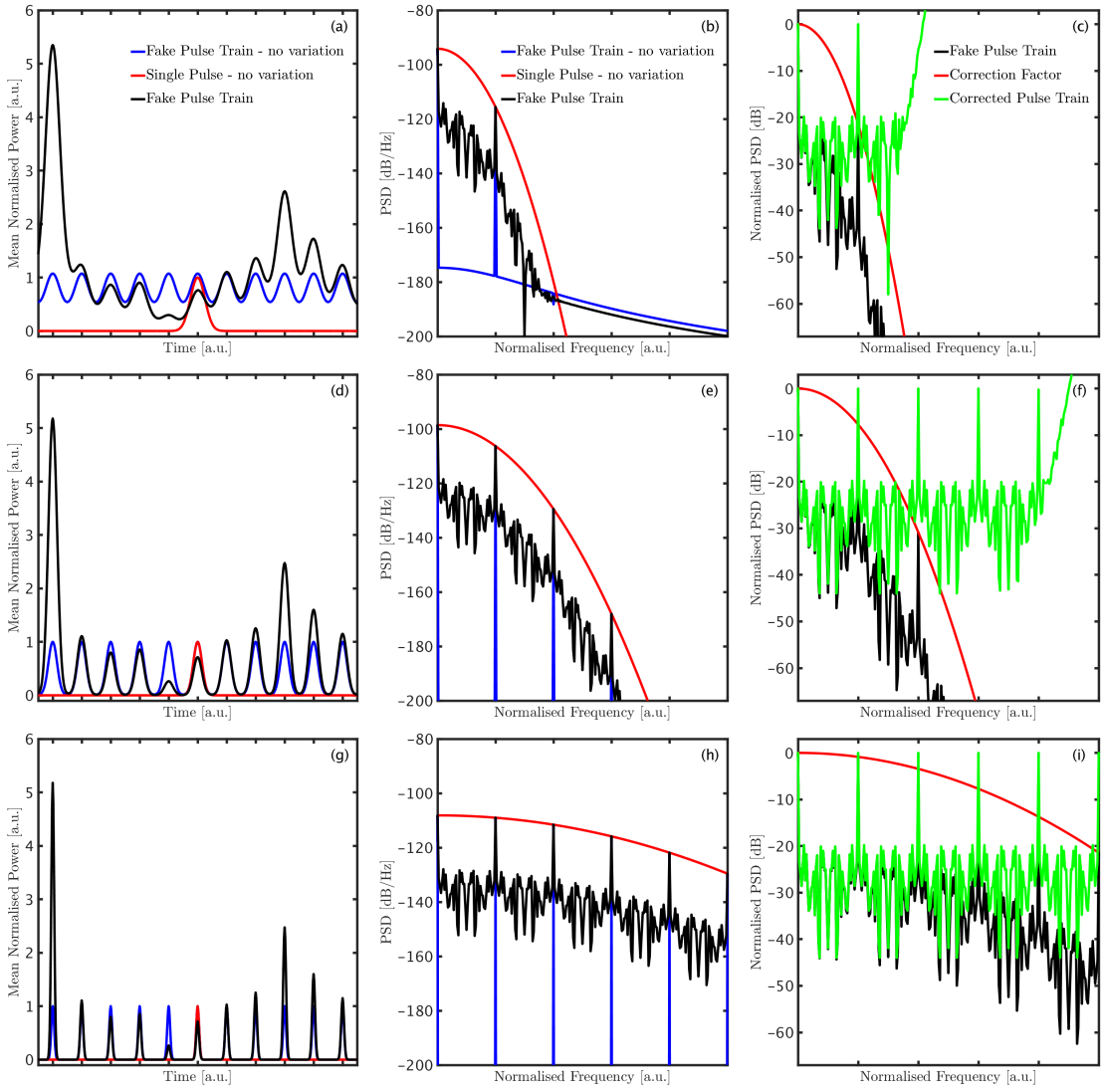

Figure 6.3: Noise examples from a constructed pulse train. The fake pulse train is based on the 50 simulations of the *Straight* fiber design described in chapter 8 and assumes a Gaussian pulse photodiode response function. The pulse train is based on the energy in a 10 nm band centered around 1295 nm. The repetition rate, time spacing and number of points are kept fixed at 100 MHz, 7.63 ps and 2^{16} respectively, while the Gaussian pulse duration is (a-c) 5 ns (d-f) 3 ns (g-i) 1 ns.

electrical signal, a fake pulse train is constructed based on the data from the *Straight* fiber described in chapter 8 for a 10 nm bin centered around 1295 nm. This can be seen in Fig. 6.3. The first column of figures show 11 out of 50 pulses from the fake pulse train with and without noise as well as the shape function, $\theta(t)$, which is equivalent to a single pulse. In the second column the corresponding PSD of the pulse train is shown. In the third column, the inverse correction factor, $\left|\tilde{\theta}[1]\right|^2 / \left|\tilde{\theta}[m]\right|^2$, and pulse train with and without the correction is shown in the frequency domain. From the theory we expect the corrected pulse train to be perfectly repeating, but we can see that is not the case. This is due to numerical errors in calculating the pulse train and correction factor. They both fall off so fast with increasing frequency that they hit the numerical noise floor, and after that the product is just numerical noise.

When the pulse becomes narrow compared to the repetition rate, and the pulse train well resolved, the rolloff with frequency is significantly slower. This is not surprising considering that the time bandwidth product of a Gaussian pulse is constant. Note how the middle row resembles the measurements shown in Fig. 6.2b. In the last case, where the rise time is 10 times better than the repetition rate, the corrected and uncorrected PSD graphs closely resemble each other. The correction factor can thus almost be neglected when summing up to calculate the pulse to pulse RIN. The RIN when doing this is in each of the three cases (from top to bottom) 25.1 %, 31.5 % and 38.5 % compared to the true value of 39.8 %. It should be clear that the pulse shape correction factor can only be safely neglected only if each pulse is clearly resolved, and that not taking it into account can lead to a significant underestimation of the RIN.

In conclusion, the RIN can be extracted from an ESA measurement by integrating the pulse shape corrected and normalized PSD up to the first harmonic, assuming the pulse duration was much shorter than the response time of the photodetector. In practice, we saw that the correction factor can be ignored when the time between pulses is much higher than the rise time of the photodetector. Mathematically this can be written as $\tau_{Pulse} << \tau_{PD} << T_0$, where "much larger than" should be understood as at least a factor 10. In practice, it is not so easy, as the first harmonic is often broad and it hides the underlying noise. It is overcome by finding the noise level of the flat part of the normalised ESA spectrum, RIN_{flat}, in units of Hz^{-1} and multiplying with the repetition frequency,

$$RIN \approx \sqrt{f_{rep} RIN_{flat}} \tag{6.15}$$

This approximates the sum described in Eq. (6.13). The upside to this method is that the noise at low frequency is used at all frequencies, which means that the error in neglecting the correction factor, which is predominant at high frequencies, is reduced. In most ESA measurements the integration time is over so many pulses that the Bessel correction factor is almost one, and can be safely neglected. Finding a flat part can be especially difficult when working with low repetition rate sources, as the first harmonic can stretch all the way to zero and thus hide the noise level.

Using the approximation in Eq. (6.15), we can see that a high repetition rate laser gives a lower RIN_{flat} value compared to a low repetition rate laser, if they otherwise have the same pulse to pulse RIN. Care should be taken that the minimum noise floor of the ESA is higher than the expected signal. Eq. (6.15) can be used as a guideline when designing a noise setup.

6.3 Time Jitter

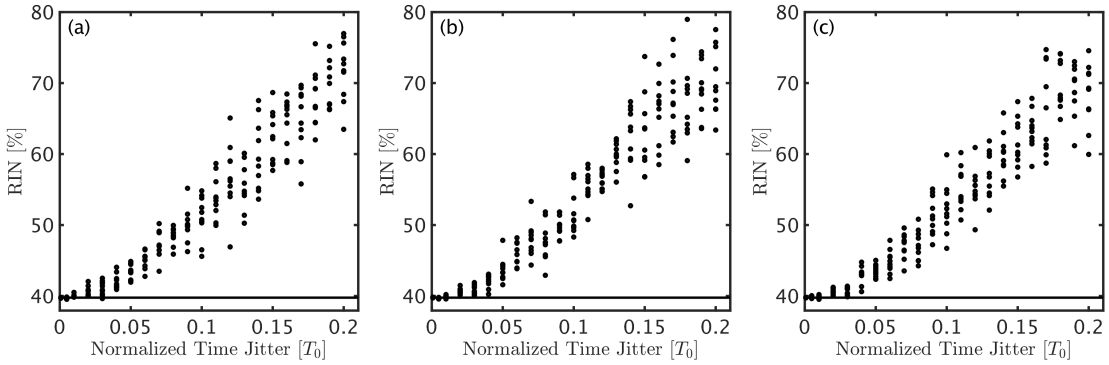

Figure 6.4: Noise examples from a constructed pulse train, including a normally distributed variation in the arrival time of each pulse (time jitter). The dots represent the RIN of a pulse train including time jitter with a standard deviation given as a fraction of the pule spacing, T_0. The line is the reference when there is no time jitter. All numerical values used match those in Fig. 6.3. A Gaussian pulse duration of (a) 5 ns (b) 3 ns (c) 1 ns was used.

As previously mentioned, time jitter should also be considered in ESA measurements. In the theory, it is not straightforward to include it. Instead, in Fig. 6.4, the results of simulations using a fake pulse train like those seen in Fig. 6.3 can be seen. The time jitter for each pulse in the pulse train was randomly chosen from a Gaussian distribution with mean as in Fig. 6.3 and a variable standard deviation in units of the time between pulses, T_0. All other parameters match those of Fig. 6.3. For increasing time jitter, 10 pulse trains were generated randomly and was analyzed using Eq. 6.13. These can be seen in Fig. 6.4, for three different photodiode response times. A few trends can be observed. First of all, when the RIN is correctly extracted from an ESA measurement the RIN falsely increases approximately linearly with increasing time jitter. This happens once the jitter is higher than a few percent of the time between pulses. Secondly, this behavior is largely independant of the pulse width. As a rule of thumb, a few percent of the pulse to pulse time is huge, and time jitter will therefore rarely influence RIN measurements using an ESA. One exception is the case described in Fig. 6.2(d), where a few percent difference in delay lines could translate into a few percent timing jitter and hence extra RIN when measuring using an ESA. Note that the analysis here is not exhaustive, only indicative.

None of the results in this section should come as a surprise, but they do quantify through examples the importance of chosing the right equipment for the job in cases when the RIN is analyzed through a Fourier transform or an ESA.

Chapter 7

Normal Dispersion Supercontinuum Generation for Optical Coherence Tomography at 1300nm

This chapter includes results presented orally at IONS Scandinavia 2018 and at Advanced Photonics Congress 2018, as well as results from the paper "Polarization noise places severe constraints on coherence of all-normal dispersion femtosecond supercontinuum generation".

In chapter 2 the reason we need low noise supercontinuum sources was discussed. It was shown how the RIN of a SC source directly determines the upper limit of the background noise in an OCT image. In chapter 6 the different ways of measuring the RIN of a supercontinuum source was discussed. Finally, in this chapter and in chapter 8, two methods to reduce the RIN will be investigated and discussed. This investigation is based on the version of the Generalized Non Linear Schrödinger Equation derived and implemented numerically in chapters 3, 4 and 5

One of the principal goals of the PhD was to figure out a design for a low noise SC source working around 1300 nm for use within OCT for skin and skin cancer detection. Existing MI based commercial sources already cover the region spectrally, but they have large enough RIN that the OCT images are not shot noise limited. Instead, this chapter will focus on normal dispersion SCG, based on SPM and OWB as described in chapter 2. In the following subsections, first we will see how Raman gain and polarization effects can ruin the coherent spectral broadening associated with SPM [17]. Then we will go through the design process for a flat and close to zero dispersion fiber that is potentially much more efficient for SPM spectral broadening as it can keep the pulse duration short. The

distance over which there is nonlinear interaction can thus be increased. This has the advantage of enabling normal dispersion supercontinuum generation at peak powers much below those that would lead to noise from Raman and PMI, as well as enabling SCG from fs lasers with lower peak power. Lastly, the lack of suitable, cheap fs pump sources for normal dispersion SCG at 1300 nm is adressed by investigating a way to both shift energy from a 1064 nm pump and at the same time enhance broadening by combining the spectrum from multiple redshifted solitons. This method, while generating a nice stable low power supercontinuum suited for OCT with an extremely stable pump laser, turns out to be extremely noisy when just a little pump noise is included.

7.1 Raman and Polarization Modulation Instability Noise in Normal Dispersion Fibers

It is well known that spontaneous Raman scattering and subsequent amplification through stimulated Raman scattering is a source of noise for most high power lasers. Recently it was shown how Raman scattering limits the coherence of normal dispersion supercontinuum generation across the whole spectrum [25]. The process is a combination of the regular Raman process, where light is generated at lower energy compared to the pump, and a second step in which it then spreads to other wavelengths by spectrally mixing through four wave mixing. In the same paper it is argued how this noise process can be suppressed when the dispersion is close to zero, or if short pulses are used. As shown in [17] both experimentally and numerically, it is not only the Raman effect that can lead to spectral degredation and noise. Also the inherent low bifringence present in any fabricated fiber, even those that have been rotated rapidly during drawing to average out any inherent assymmetries, is enough to cause PMI between orthorgonal polarization states. The results of those papers can be summed up as shown in Fig. 7.1. A few conclusions can be drawn based on this sketch and the equations that govern the processes. First of all, any fiber should be longer than the OWB length, to ensure a smooth spectrum. Secondly, it should for a given pulse duration be short enough that neither Raman or PMI noise has enough fiber length to build up. This means we have to operate in the area marked with green in the figure if we want a smooth spectra with low noise.

As shown with commercial fibers in [17, 25], the Raman gain can be suppressed if the dispersion is close to zero. In this case we only need to worry about PMI. The following discussion of PMI is based on the theoretical analysis presented in [2] for CW fields. This analysis determines the dependencies in the limit of $T_0 \to \infty$. In the case of high birefringent fibers, such as PM fibers, PMI is completely suppressed when pumping along a principal axis [2]. In the case of low bifringent fibers (which is essentially all non PM fibers), the cases of slow and fast pumping differ. For fast axis pumping, PMI is only present when the power is $P_{crit} > 3\left|\beta_{0x} - \beta_{0y}\right|/2/\gamma$. This can be increased by making the fiber more bifringent. The other option is pumping in the slow axis. In this case there is not a critical power, but instead the gain bands are located far from the pump, with the

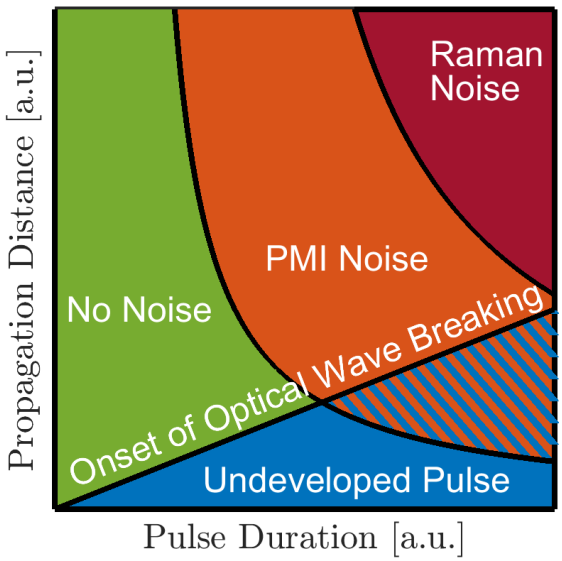

Figure 7.1: Sketch of the onset of different noise as well as development of the pulse as a function of pulse duration (fs regime) and propagation distance for a given peak power. Constructed from [17, 25].

minimum frequency shift from the pump given by $\sqrt{2\left(\beta_{0x}-\beta_{0y}\right)/\beta_2}$. This opens up for the possibility to push the gain bands outside the supercontinuum range by pumping in the slow axis. This also requires us to minimize β_2 or to increase the constant difference in the propagation constant $\left(\beta_{0x}-\beta_{0y}\right)$. A third option is to pump with less power. This is however not feasible as the critical power is typically orders of magnitude smaller than what we would need to pump with to obtain a broad supercontinuum.

In conclusion, the optimal fiber for low noise normal supercontinuum generation is a fiber with a dispersion as close to zero as possible over as large a spectral region as possible, preferably with a high bifringence. The flat dispersion will be the topic of the next section. In the remaining chapters the scalar GNLSE is used for all simulations, as PMI can be overcome by making a polarization maintaining version of the fiber [45].

7.2 Flat Dispersion Fiber Design

A flat, close to zero and normal dispersion fiber with a high nonlinearity is optimal for SPM SCG, as this slows down the rate at which the pulse broadens in time. This in turn keeps the peak power high, and ensures a sharp slope of the pulse envelope in time. The slope and the strength of the nonlinearity determines the rate of spectral broadening. At the same time, a low dispersion decreases both Raman and PMI noise. As seen in [21], it is possible to design a PCF which has a close to zero dispersion over a wide range

of wavelengths, and which has a tunable Minimum Dispersive Wavelength (MDW). This section is the continuation of the work, but here the focus will be to reach a fiber design with a flat dispersion as close to zero as possible in as wide a range as possible around 1300 nm. And most importantly it should be possible to draw the fiber with current technology. Through discussion with experts in fiber drawing employed at our supplier NKT Photonics, the specification limits for a fiber would be a minimum hole size of 500 nm (but a little bit bigger would be better) and a maximum number of rings of holes to be 10. Furthermore, the holes in the fiber should be as uniform as possible, as varying the hole size make the fiber difficult to draw.

In Fig. 7.2 (a+b) we see the measured dispersion and loss for an NKT photonics ANDi fiber. This fiber was used to test the COMSOL results and calibrate numerical parameters. The red loss edge is shifted significantly towards higher frequencies compared to the first simulation seen in panel (c). This is due to a known issue with that particular fiber. There is a slight decrease in hole diameter for holes the further they are from the center. This was included in the modelling by leaving the innermost 3 rings intact, and then letting the hole size of the next 7 rings decrease linearly with a percentage of the pitch. This percentage is 0.5%, 0.75% and 1% respectively for Fig. 7.2 (d-f). The loss edge was a good match for panel (e).

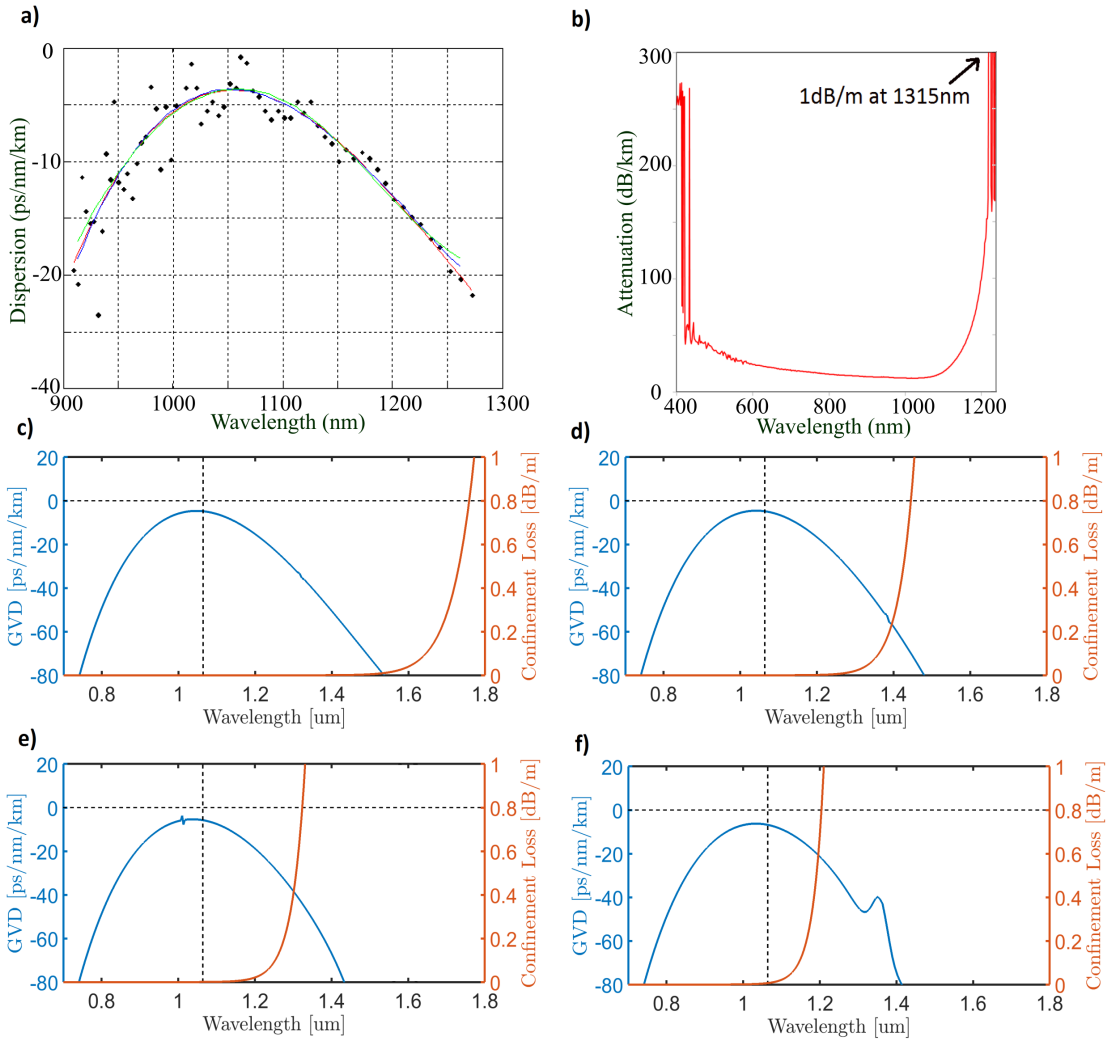

Figure 7.2: Comparison between measurements of a fiber drawn at NKT Photonics (courtesy of NKT Photonics) and the numerical model. (a) and (b) are measurements, (c) is dispersion and confinement loss with a uniform fiber with 10 rings, $\Lambda = 1.49\,\mu$m and hole size $d = 605\,$nm. In (d-f) the hole size of the outer rings is decreased by ring number, beyond the first ring, multiplied with pitch and a slope percentage. This percentage is 0.5%, 0.75% and 1% for the three last figures. The first ring sets the dispersion curve, while the subsequent rings determine the losses.

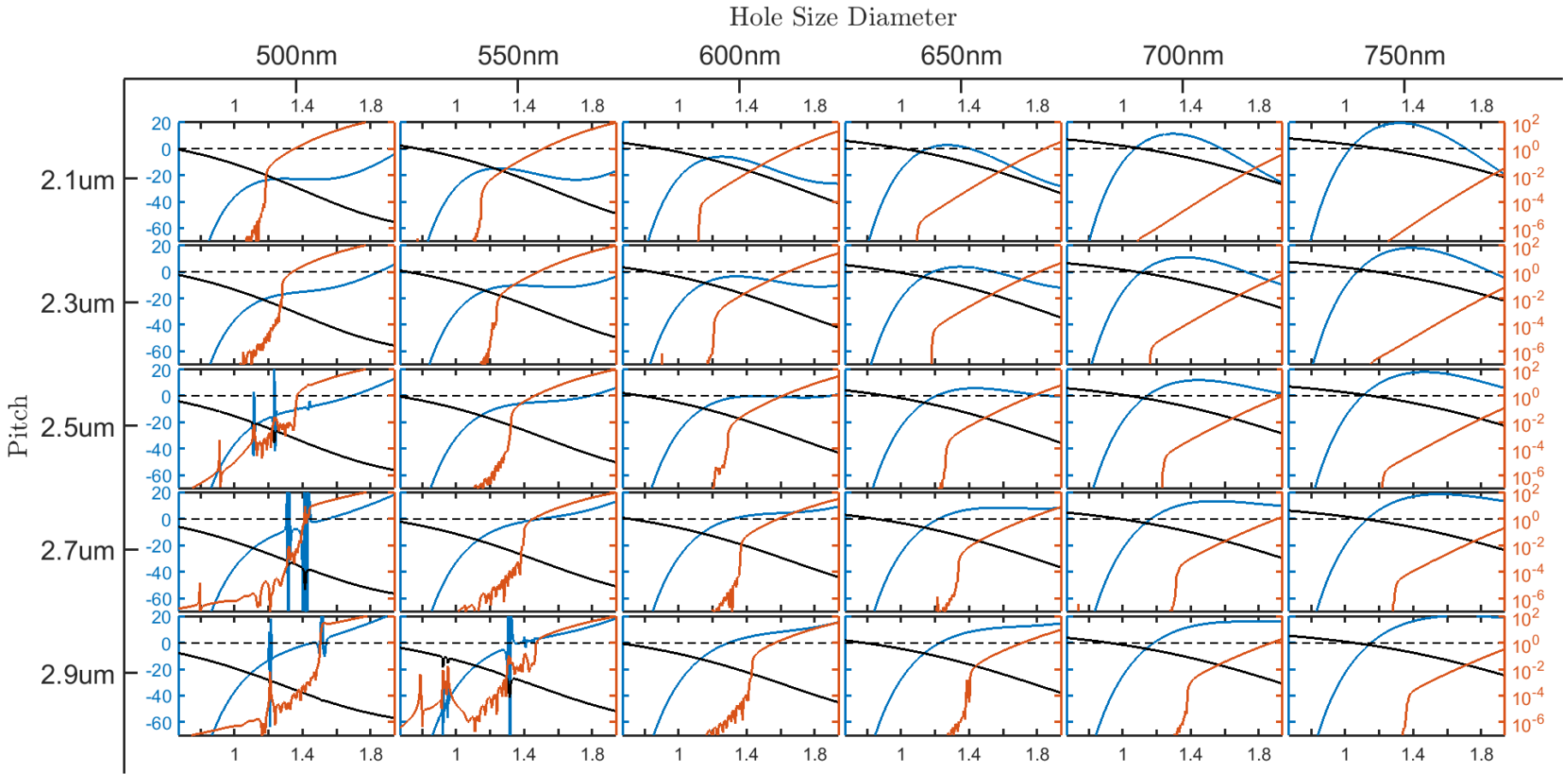

Figure 7.3: Graphical presentation of the different fiber designs considered. Shown are the dispersion (blue) in $\mathrm{ps\,nm^{-1}\,km^{-1}}$, confinement loss (red) in $\mathrm{dB\,m^{-1}}$ and finally overlap with the core (black) in percentage, with 0% at the bottom of each graph and 100% at the top of each. The dashed black line is the zero dispersion line and also the $1\,\mathrm{dB\,m^{-1}}$ loss, which corresponds to the loss edge. The rapid oscillations in the bottom left part are due to small variances in the refractive index that are magnified when the five point method is used to find the derivative.

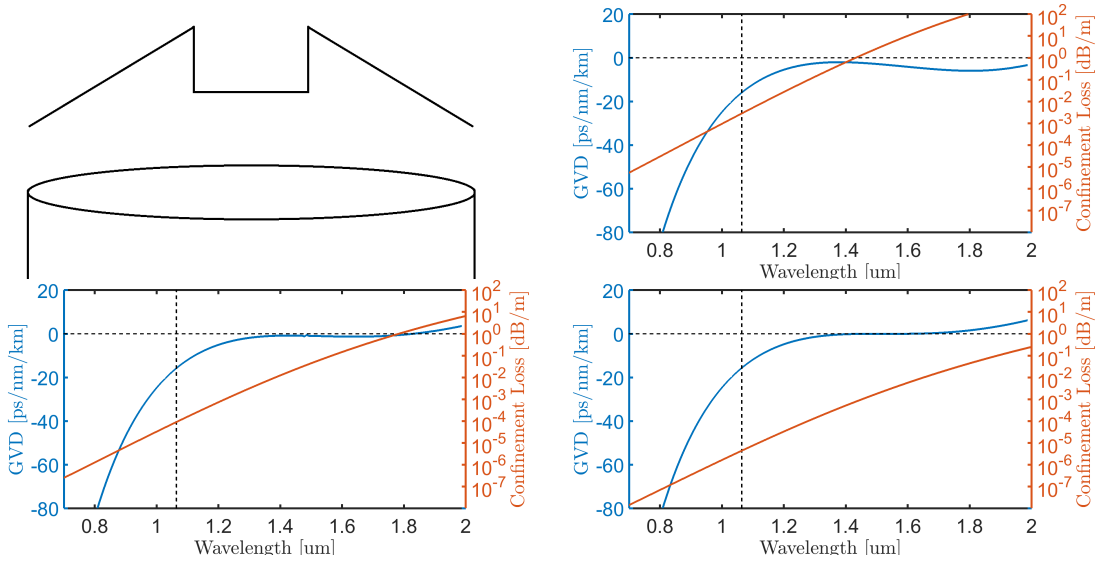

Figure 7.4: (a) Graphical representation of the design of a fiber with two sets of hole sizes. The innermost three rings have one size, $d_{1-3} = 600\,\text{nm}$, while the outer rings have a different size, determined by the jump in hole size between the third and fourth ring of holes. The decreasing hole size from the fourth ring of holes and outwards is the one determined in Fig. 7.2. it is 1% of the pitch per ring corresponding to 23 nm per ring. The hole size of the fourth ring is (b) $d_4 = 650\,\text{nm}$ (c) $d_4 = 700\,\text{nm}$ (d) $d_4 = 750\,\text{nm}$.

Starting from the most promising values reported in [21], $\Lambda = 2300\,\text{nm}$ and $d = 600\,\text{nm}$, a sweep over different value of hole and pitch can be seen in Fig. 7.3. This sweep excludes the decrease in hole size. In the lower left corner the solver has had some trouble with the exact value of the refractive index, which gives the disjoints. The results with these errors were discarded for this reason, as well as not possessing the right shape of the dispersion curve for the application. Starting with the dispersion, the right hole and pitch would for optimal flatness be $\Lambda = 2500\,\text{nm}$ and $d = 600\,\text{nm}$. This gives a normal dispersion close to zero in the spectral interval from 1200 nm to 1800 nm. The problem with this is that the loss edge would be at 1600 nm, which limits the application. A quick review of the other options show us that there is no good option with a flat dispersion and a low loss. Furthermore, the confinement loss shown is the best case scenario, as there is a slight decrease in hole diameter for holes the further they are from the center, which enables more light to leak out.

After the initial investigation, a more in depth investigation is conducted. The focus is on the design with parameters $\Lambda = 2300\,\text{nm}$ and $d = 600\,\text{nm}$, including the decreasing hole diameter after ring 3 of 0.75% corresponding to decrease of 17 nm per ring. The perceptive reader will note that this is not the optimal design from Fig. 7.3. This is due to two things. First of all we would like to make sure the fabricated fiber has normal dispersion everywhere, and secondly, we would like to move the red loss edge further

out. This last part is accomodated by making a small step in hole diameter between the third and fourth rings. A sketch of the hole diameter design can be seen in Fig. 7.4 (a). This hole diameter step has a small impact on the dispersion, as the dispersion is mostly determined by the innermost rings at low wavelengths, but will be increasingly more important as wavelength is increased, and the electric field mode expands and more of it reaches out to "see" the outer rings. It will move the dispersion curve upwards. In Fig. 7.4 (b-d) different sizes of the step can be seen, from 50 nm to 100 nm and 150 nm. The impact of the small step of 50 nm is to move the loss edge more than 300 nm, and we can see that without this step, the losses would prevent light in the region of interest. We are not interested in generating solitons above the zero dispersion wavelength that could potentially transfer noisy light back below the zero dispersion wavelength. This means we prefer the loss edge to be just below the zero dispersion wavelength as seen in (c).

The final choice for which fiber to fabricate is the one seen in (c), with $\Lambda = 2300$ nm, $d = 600$ nm and a step of 100 nm between the third and fourth ring. This will be the fiber referred to as the *Flat* fiber in the remainder of this chapter. In the next section, a way of pumping the fiber with existing commercial pumps sources at 1064 nm is investigated. The goal is to obtain a low noise normal dispersion based supercontinuum covering from 1100 nm to 1500 nm using cheap commercial products, as well as investigating the effects of such a flat and close to zero dispersion.

7.3 Low Power Supercontinuum based on Redshifting Solitons

Creating a normal dispersion based supercontinuum that covers the spectral range 1100 nm to 1500 nm would be relatively easy using a fs source with a center wavelength of 1300 nm. Unfortunately this source is not commonly available commercially, although the 10 GHz VCSEL from Alight Technologies seem promising. Due to the close to zero dispersion offered by the *Flat* fiber, the peak power would not even have to be that high. In fact, it could even be low enough, that a single fundamental soliton at this wavelength sent into the fiber could potentially broaden enough to cover the whole range. Furthermore, it would be possible to redshift the soliton to the right wavelength range using the soliton self frequency shift. This lead to the idea of a two stage approach. The first stage would generate the soliton and redshift it to the right wavelength, and the second stage would broaden it in the *Flat* fiber. This is also an extension of the two stage approach that was suggested in [57]. The idea can even be extended to include several solitons generated through the deterministic low noise process of soliton fission, redshifted and then broadened in a normal dispersion fiber to close the spectral gaps between them. The idea can be seen outlined in Fig. 7.5 (a+b).

To generate suitable solitons through soliton fission from a pump at 1064 nm, a suitable fiber is necessary. In order for the fission to be noise free, the soliton number, defined

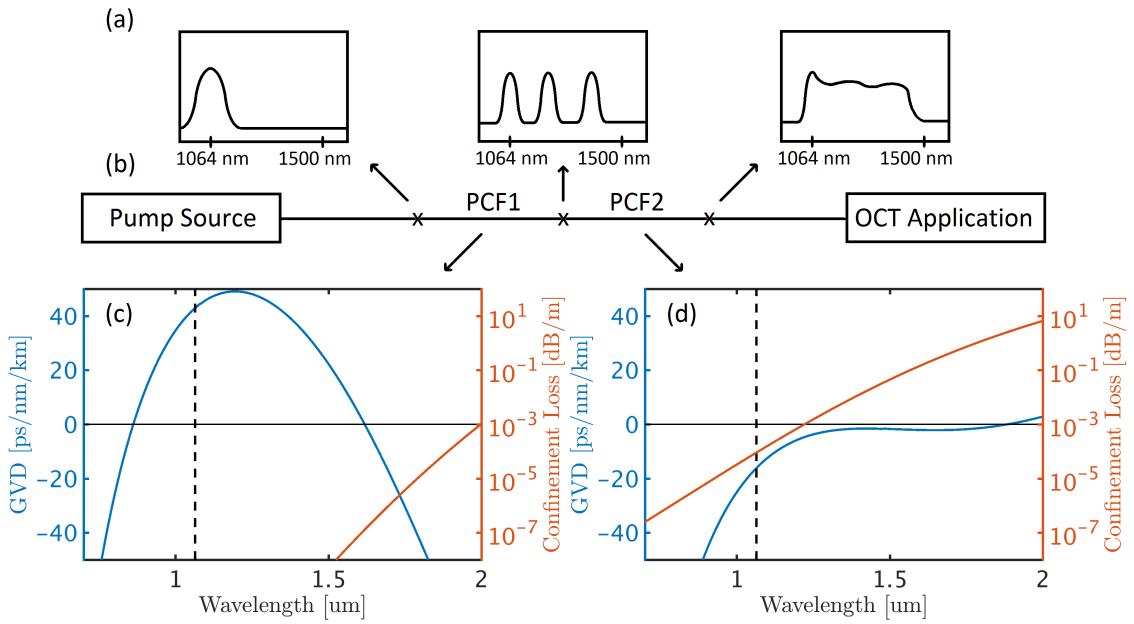

Figure 7.5: (a+b) Illustration of the idea behind the simulation. (c+d) Simulated dispersion and confinement loss properties of the first and second fiber, respectively.

as

$$N_{sol}^2 = \frac{\gamma P_0 T_0^2}{|\beta_2|} \tag{7.1}$$

has to be less than 16, [2,8,14]. Here γ is the nonlinear parameter, P_0 is the peak power, T_0 is the width of the sech shaped pulse, and β_2 is the second order derivative of the propagation constant. Since we want to pump as much energy as possible into the generated fundamental solitons to ensure that they have the best conditions for broadening and there is an upper limit on N_{sol} due to noise, $|\beta_2|$ should be as large as possible. A fundamental soliton with a fixed pulse energy proportional to $P_0 T_0$, that is undergoing Raman self frequency shifting will see a changing β_2 as it changes its central wavelength. From the same equation, we can see that if N_{sol} is kept constant equal to one as is the case for a fundamental soliton, and there is no energy loss, a decreasing β_2 for increasing wavelength must result in a lower T_0. This means the important ratio P_0/T_0 that maximizes SPM is increasing. A fiber with a second zero dispersion wavelength above the pump is therefore optimal. The most redshifted soliton should only reach around 1400 nm. To obtain space to operate in and to prevent any light from being transfered across the second zero dispersion, it should be at around 1600 nm.

These requirements lead us to look for fibers which have two ZDWs, one on each side of the pump, with anomalous dispersion in between. Preferably the ZDW on the red side of the pump should be around 1600 nm to get β_2 to be as close to zero as possible for the most redshifted soliton. At the same time the ZDW on the blue side of the pump should

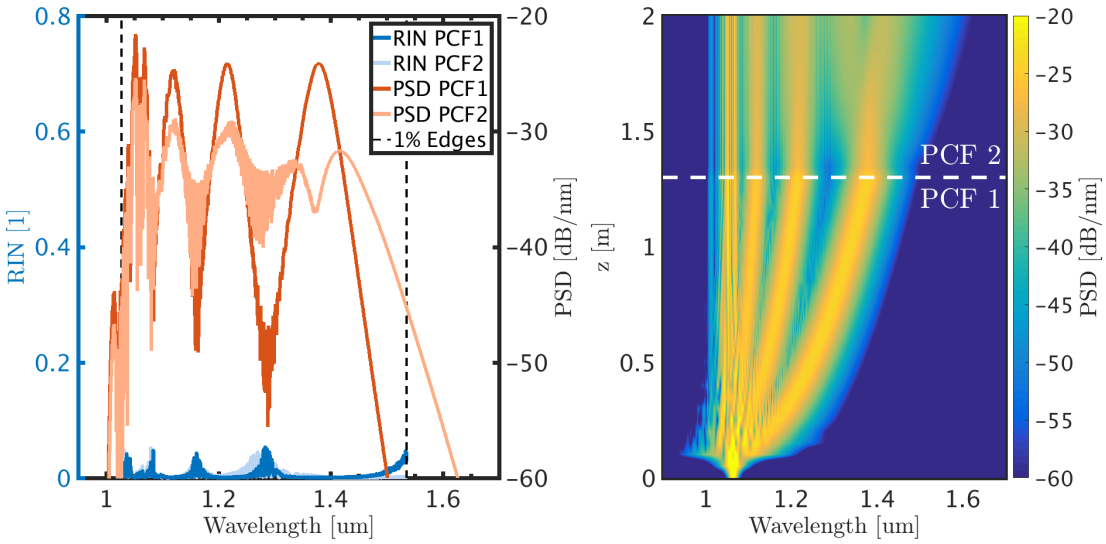

Figure 7.6: The figure shows the spectral evolution and output for an ensemble of 30 simulations rebinned to a spectral width of 400 pm corresponding to common spectrometers used in OCT.

T_{FWHM}	Peak Power	Rep. Rate	Central Wavelength	Shape	Chirp	Avr. Power
250 fs	2 kW	1000 MHz	1064 nm	sech $(\,)^2$	None	568 mW

Table 7.1: Pump specifications for the simulations in Fig. 7.6 and 7.7. The specifications are for the pulse power envelope, $P(t)$.

be minimized to maximize the dispersion slope from the pump to the red ZDW. These requirements are not directly compatible with the material dispersion of silica, and thus are equivalent to a strong contribution to dispersion from the waveguide, which is in turn equivalent to a tightly confined field. The downside of such a field is that the mode is usually very small. Much smaller than the already small mode of the *Flat* fiber, which could potentially make the splice lossy. Hence the exact choice of PCF pitch and hole size is a trade off. In Fig. 7.5 (c), the dispersion of a fiber that satisfy all demands can be seen. The parameters for the fiber, which will now be denoted *Fission* are $\Lambda = 1620$ nm, $d = 832$ nm. The only downside is that the mode field diameter is 2.32 μm compared to 5.1 μm for the *Flat* fiber at a wavelength of 1300 nm. The emphasis on mode field diameter match between the fibers was down prioritized because the coupling goes from the small fiber to the large fiber. With the right splicing technique the splicing transmission can be better than the immediate mode mismatch would suggest. In the following a splice loss of 50% is assumed. According to the results presented in [54], the fiber is single mode in the wavelength range of interest, despite that $\frac{d}{\Lambda} > 0.44$.

With the initial *Fission* fiber, the pump parameters seen in table 7.1 give three nice

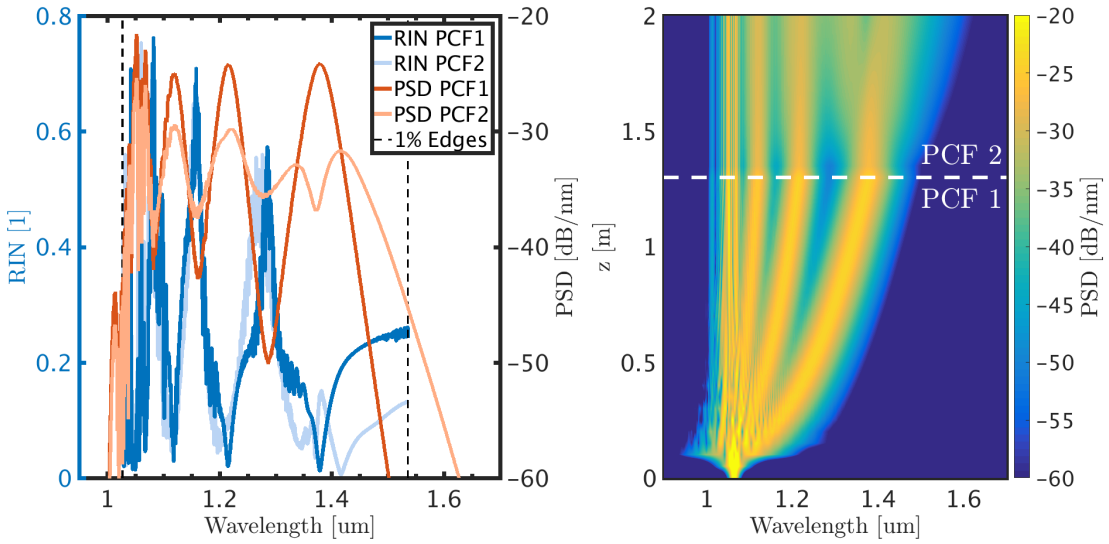

Figure 7.7: The figure is the same as in Fig. 7.6, with a single difference. In the ensemble simulation, a random but normally distributed relative peak power noise of 1% was used. This correspond well to the noise measured in the lab, reported in [17].

solitons after 1.3 m of propagation. The evolution and RIN including the splice and propagation in the *Flat* fiber can be seen in Fig. 7.6. As expected after propagation in the *Fission* fiber, the three solitons span the whole spectral region of interest from 1100 nm to 1500 nm, but with large gaps without power in between. The RIN at this stage is almost non existant as the fission process is deterministic. After propagation in the *Flat* fiber, the solitons have broadened as expected, and filled the spectral gaps between them. Unfortunately we can see that they also interfere in these regions. The interference oscillations are extremely rapid with a period of about 0.8 nm. For OCT applications, this is not good, as fringes is what gives depth information, and fringes in the supercontinuum source could lead to ghost signals in images. Furthermore, spectral variations should be kept to a minimum, preferably less than 3 dB, to increase signal strength. We can see that the variations in this case are almost 10 dB in the most extreme case. As a positive result the light cover the whole spectral range, from 1100 nm to 1500 nm interest with an average effect of ≈ 193 mW assuming a 1 GHz repetition rate. This is more than enough for medical OCT applications, where too much light burns the sample.

In Fig. 7.7 almost the exact same simulation is performed again. The only difference is the addition of 1% random Gaussian variation in the pump peak power, as explained in Eq. (5.4). This correspond to the expected level in most source systems. This is enough to change the relative phase between the solitons, and cause the interference fringes that were before steady between simulations to now fluctuate. The result is that the fringes average at the cost of a huge increase in the RIN at the wavelengths in between the solitons. The ghost signals that would occur in an OCT signal due to these fringes is no

more. On the other hand, the RIN is locally much higher. As the noise floor in an OCT image is a Fourier transform (and hence a mix) of all the noise in the spectrum, the source proposed here should give a lower mean noise floor. It is lowered further due to the possibility of operating this source at an extremely high repetition rate of 1 GHz. This is only possible because the supercontinuum spectral width is not reliant on pumping with high peak power pulses to obtain significant broadening. In fact, in this design increasing the peak power will only increase the RIN across the spectrum due to more solitons fissioning out, and it will also decrease the average energy in the wavelength range of interest as more light will spread beyond the wavelength range of interest. Other noise sources such as Raman noise and PMI noise discussed earlier in this chapter will have no influence as the pulse durations and peak powers are orders of magnitude smaller than those reported in [17], for comparable fiber lengths and nonlinear coefficients. The biggest advantage of this design over those discussed earlier is the low peak power and relatively long duration fs pulse cheap sources available at 1064 nm. Recent advances in high repetition rate short pulse VCSEL technology [22, 31, 65] show one possible path for even cheaper tailored, low noise and low power supercontinuum sources.

To sum up this chapter, different ways of obtaining a low noise supercontinuum centered at 1300 nm based on normal dispersion fibers were investigated. The focus was on an extremely flat, close to zero dispersion PCF. While the investigation into a GHz repetition rate low peak power source showed promising results, the RIN reductions were an improvement, but not as good as expected due to soliton interference. The immediate future will most likely belong to polarization maintaining ANDi fibers pumped with short pulses and high peak power for applications around 1064 nm, due to the avaibility of fs pumps at this wavelength. For all other wavelengths, the commercial sources already available will continue to dominate for the reasons we shall see in chapter 8.

Chapter 8

Supercontinuum Noise Reduction by Fiber Undertapering

This chapter is based on the results to be published in the paper "Supercontinuum Noise Reduction by Fiber Undertapering".

Supercontinuum generation by way of modulation instability is the basis for most commercial supercontinuum sources. As described in chapter 2, it works by pumping in the anomalous dispersion regime close to the zero dispersion wavelength. A picosecond or nanosecond pulse breaks up into a number of fundamental solitons, due to MI. These then interact chaotically in what is commonly referred to as a sea of solitons, where collision and energy transfer take place. At the same time these solitons spectrally transfer energy to dispersive waves across the ZDW. After some time of collision and energy exchange, the sea of solitons stochastically produces a high energy fundamental soliton. This high energy soliton will rapidly redshift due to intrapulse Raman transfer of power. As the soliton redshifts, it spectrally leaves the sea behind. At the same time it will also move away in time as there is a change in the group velocity due to the redshifting frequency. As the soliton redshifts, it in turn forces the trapped DW to blueshift. This is the basis for the spectral broadening to red wavelengths and how this also results in a broader spectrum on the blue side. Since the light far from the pump is based on the presence of a few fundamental solitons created through chaotic interaction, it is very noisy. A way of reducing this relative intensity noise is the focus of this chapter.

The idea of undertapering stems from previous investigations into the supercontinuum processes and noise in a tapered PCF starting from a pitch of $\Lambda = 3.3\,\mu$m and a hole to pitch ratio of $d/\Lambda = 0.52$ [51, 53, 72]. In this work, they find that the degree of tapering necessary to obtain the supercontinuum extending to the highest frequencies, is when the pitch reaches the value of $\Lambda = 2.5\,\mu$m. This optimum is calculated as follows: The maximal wavelength of a soliton determines the minimum blue wavelength through GV matching. The maximum red is limited by either the loss of the fiber, at 2300 nm or the

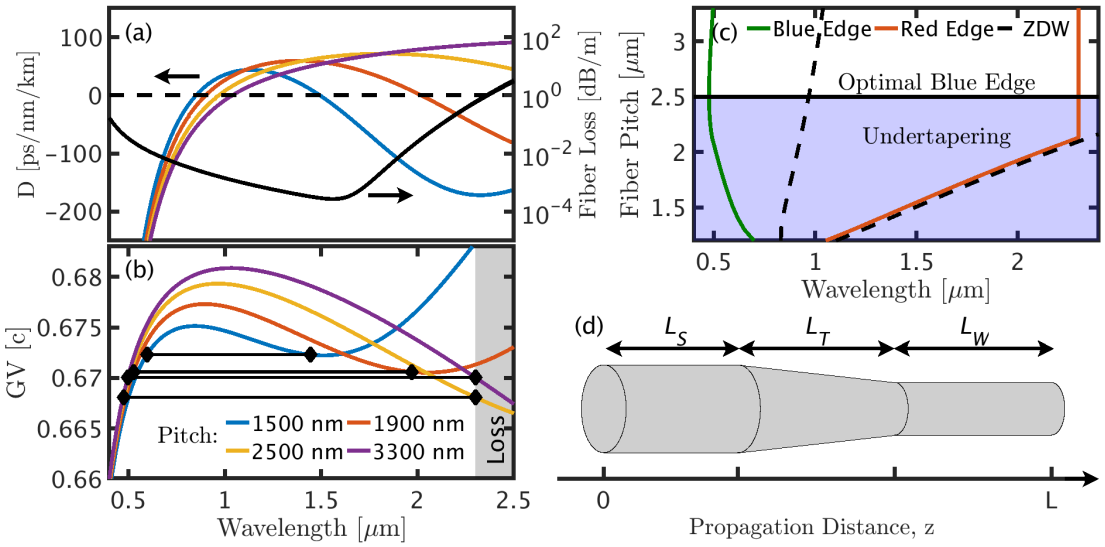

Figure 8.1: (a+b) Fiber dispersion (D), total loss and Group Velocity (GV) normalized to the speed of light for hexagonal photonic crystal fibers with 10 rings of varying pitch. The pitch to hole ratio is constant $d/\Lambda = 0.52$ for all fibers investigated. (c) The predicted edges of the supercontinuum based on GV, matching the blue edge to the red edge (marked with diamonds and black lines in (b)), while the red edge is the minimum of either 50 nm before the second ZDW or the loss edge (2300 nm, [72]). The colored area marks the area of undertapering. (d) Schematic representation of the taper under investigation with the three lengths marked.

maximum soliton wavelength, whichever is lowest. The maximum soliton wavelength is the maximum wavelength of anomalous dispersion minus 50 nm. The dispersion, group velocity, and group velocity matching of this fiber and its tapers assuming a constant hole to pitch ratio can be seen in Fig. 8.1. The tapering pitch that gives the optimal blue edge is clearly visible in Fig. 8.1. Undertapering is when the fiber is tapered below this pitch. A US patent, [30], show that this region has substantially lower noise. But no explanation is given. The aim of this chapter is to investigate and explain this noise reduction through numerical simulations.

The simulations have all be conducted based on a single mode propagation of the GNLSE as derived in chapter 3 and described in chapter 5. To solve this equation we need the initial electric field as well as the propagation constant and transverse mode field distribution. The first step in the simulation is therefore finding the fiber attributes such as the complex propagation constant and the mode overlaps at various points in the taper. This was done in advance by solving the full transverse fields using COMSOL. Sweeping the frequencies for a single PCF design takes many hours if a high resolution and 10 rings of air holes are used. Solving it at every step in the taper would take forever, so instead it is solved for every 100 nm of the pitch, and the results are interpolated linearly to the

T_{FWHM}	Peak Power	Rep. Rate	Central Wavelength	Shape	Chirp	Avr. Power
7 ps	7 kW	80 MHz	1064 nm	sech ( )^2	None	4.71 W

Table 8.1: Pump specifications for all simulations involving undertapering. The specifications are for the pulse power envelope, $P(t)$.

value at every step in the GNLSE.

8.1 Taper Profiles

The initial parameters used were as seen in table 8.1. These correspond roughly to the values used in experiments [51, 53, 72]. Furthermore a 1% Gaussian fluctuation in input power was also used to include the pump noise. We saw in chapter 7 and [17] how this was a large influence in the output noise for low RIN normal dispersion SCG. The numerical parameters were a time and frequency discretization of $N = 2^{19}$ points with an equidistant time spacing of $\Delta t = 0.92$ fs. Each ensemble had an ensemble size of $N_E = 50$. All presented spectral data, with the exception of the spectrograms was rebinned to 10 nm intervals. For the RIN analysis, this corresponds to measuring the pulse to pulse noise of light with perfect 10 nm bandpass filters.

Before discussing results, it should be noted that as with most investigations in this thesis, the focus were on applications within SD-OCT. In particular the visible (VIS) spectral band from 500 nm to 800 nm and the spectral band from 1150 nm to 1450 nm that is promising for skin imaging. Both have attracted attention recently [20, 29, 47, 68, 85]. To obtain a single figure of merit, the weighted RIN in each of the two important ranges of interest to the field of SD-OCT can be calculated. The advantage of this is a single overall fixed figure of merit for these applications that can be used as a guideline when assessing a source. This figure of merit, the Power Spectral Density (PSD) weighted RIN is calculated as

$$\langle RIN(\lambda)\rangle_{\lambda_1}^{\lambda_2} \equiv \frac{\int_{\lambda_1}^{\lambda_2} PSD(\lambda)\, RIN(\lambda)\, \mathrm{d}\lambda}{\int_{\lambda_1}^{\lambda_2} PSD(\lambda)\, \mathrm{d}\lambda}. \tag{8.1}$$

The PSD follows the usual definition, while the RIN is defined as,

$$RIN(\lambda) = \sqrt{\frac{\langle E_n^2(\lambda)\rangle - \langle E_n(\lambda)\rangle^2}{\langle E_n(\lambda)\rangle^2}} \tag{8.2}$$

where $E_n(\lambda)$ is the energy of a single pulse in the wavelength interval from $\lambda - \Delta\lambda/2$ to $\lambda + \Delta\lambda/2$. Throughout this chapter, $\Delta\lambda = 10$ nm, corresponding to commercially available standard filters used in several earlier noise investigations, [38, 51, 52].

In Fig. 8.2 the average PSD and noise evolution of four different designs can be seen. Each

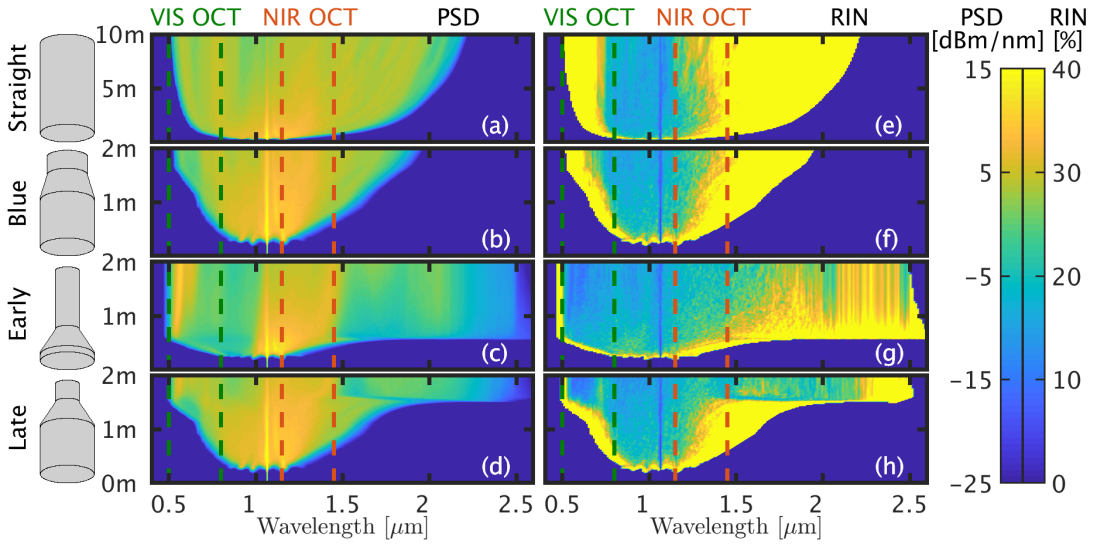

Figure 8.2: Simulated average PSD and RIN evolution with propagation distance of various fiber designs. The designs are shown on the left side. *Straight*: Untapered 3.3 μm pitch for $L_s = 10\,\text{m}$ *Blue*: Fiber tapered from 3.3 μm to 2.5 μm pitch, with $L_s = 1.1\,\text{m}$, $L_T = 0.5\,\text{m}$ and $L_W = 0.4\,\text{m}$. *Early*: Fiber tapered from 3.3 μm to 1.5 μm pitch, with $L_s = 0.1\,\text{m}$, $L_T = 0.5\,\text{m}$ and $L_W = 1.4\,\text{m}$ *Late*: Fiber tapered from 3.3 μm to 1.5 μm pitch, with $L_s = 1.1\,\text{m}$, $L_T = 0.5\,\text{m}$ and $L_W = 0.4\,\text{m}$. Note that for all cases the RIN is only shown when the PSD is higher than $-20\,\text{dBm/nm}$. The RIN scaling has been chosen to best show the noise in the NIR OCT band. Near the spectral edge the RIN can reach values in excess of 100 %.

row in the figure represents one of the four designs. The first two, the *Straight* and *Blue* fiber designs, have been studied before both experimentally and theoretically [51, 53, 72]. While the spectrum continues to broaden with propagation, we can see that the noise does not change much as soon as we are sufficently far away from the spectral edges. This is in agreement with previous work, [51, 53, 72].

In the last two rows of Fig. 8.2, we investigate two cases of undertapering the fiber down to a pitch of $\Lambda = 1.5\,\mu$m, to reduce the RIN by clamping the solitons at the second ZDW. In the figure the two OCT bands of interest are marked. In the *Early* design, Fig. 8.2 (c+g), the fiber is tapered so that the second ZDW reaches its final wavelength at 1500 nm just before any significant power transfers past this wavelength. In the *Late* case, Fig. 8.2 (d+h), the tapering is initiated 1 m later to investigate the noise in the case where the second ZDW spectrally moves through the redshifting solitons.

In both the *Early* and *Late* cases we see a large buildup at the blue edge, starting at 535 nm and then shifting to around 565 nm in the taper waist. A 10 kW peak power soliton at

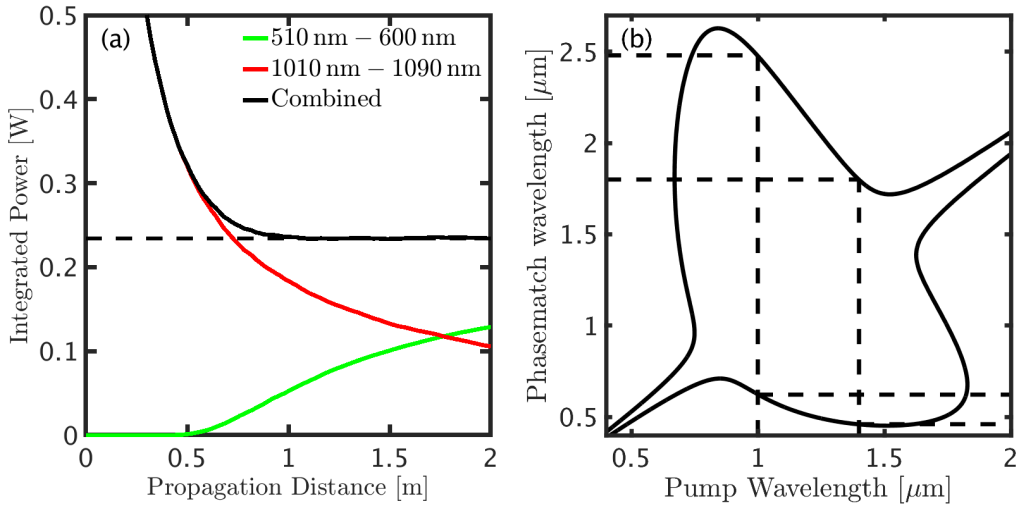

Figure 8.3: (a) Integrated power in wavelength ranges around the pump, the blue peak and the sum of those two as a function of propagation distance. (b) Dispersive wave phasematching wavelength diagram for a variable soliton wavelength given a peak power of 10 kW in the tapered section of the *Early* and *Late* fibers. The pitch is $\Lambda = 1.5\,\mu$m. It is based on theory, equation 12.1.5 in Agrawal [2]. The dotted lines indicate the approximate spectral range of dispersive waves based on the spectral range of the sea of solitons.

1080 nm has phasematching to 565 nm but cannot directly generate a dispersive wave at this position, as there is no spectral overlap. The solitons from the sea of solitons can however trap light close to the pump wavelength and spectrally push it into this region when they themselves redshift to the second ZDW. The phasematching diagram can be seen in Fig. 8.3 (b). The nonlinearity is enchanced in the taper, which enhances MI from the remainder of the pump and speeds up the process. The rate of depletion of the pump after 1 m of propagation closely match the increase in power around 565 nm. This can be seen in Fig. 8.3 (a).

In the *Early* design, after the initial broadening beyond 2 μm at the start of the fiber waist, the power transfer to the red side of the second zero dispersion wavelength slows down. While the power is steady, the noise in this region is gradually improved. The spectrum is clearly still noisy at the edges, but at the same time there are clear improvements compared to the *Blue* and *Straight* designs. In the *Late* case we see the same spectral buildup as in the *Early* case. But the noise properties look excellent right away, without the need for the light to propagate some distance to settle. There is a clear drop in power visible around the second ZDW as it moves in from the red edge. Established theory would tell us that solitons are recoiled and prevented from existing right at the second ZDW, [10, 69]. In both cases we can observe how the losses start to eat away at the red edge. This is especially clear from the −25 dBm/nm edge cutoff on the RIN plots.

For a more detailed view, the output spectrum and relative intensity noise of the four cases can be seen in Fig. 8.4. The straight fiber and the *Blue* design have similar noise properties, with the long wavelength noise almost coinciding, while at the blue edge the noise edge is moved slightly (75 nm) out for the taper. From earlier work [51, 53, 72], we would expect an extended blue blue edge compared to the straight fiber, which is not the case in the figure. This is simply because the *Blue* design has not yet reached its full spectral extension after 2 m of propagation. For the *Early* and *Late* fibers, the PSD variations within the VIS band of interest is 11 dBm/nm and 4.6 dBm/nm respectively, which is a bit large for OCT, but with the right filter, it is not insurmountable.

For all four cases there is a gap on the blue side of the pump. It is least pronounced for the *Blue* design, and most for the *Early* and *Late* designs. For all cases it is centered around the zero dispersion wavelength in the taper waist, which shifts to lower wavelengths the more the fiber is tapered. The values are 1040 nm for the *Straight* design, 970 nm for the *Blue* design and 860 nm for both *Early* and *Late* designs. Unsurprisingly the 10 m *Straight* fiber has the most depleted pump with only 3.6 dBm/nm remaining due to its length. Of the remaining 2 m long fibers, the *Blue* design has the least depleted pump with 9.9 dBm/nm remaining, the *Late* 7.9 dBm/nm, *Early* 5.6 dBm/nm. The pump depletion matches well with increased power in the dispersive wave. On the red side of the pump, in the spectral region of interest (marked with red), we can see that all cases give a flat spectrum (maximally 3 dB variations), which is acceptable for OCT. As expected, we see there is a huge dip in the power spectral density for the *Early* and *Late* fibers, at the second ZDW at 1500 nm. The dip is larger for the *Late* design (8.1 dBm/nm) than for

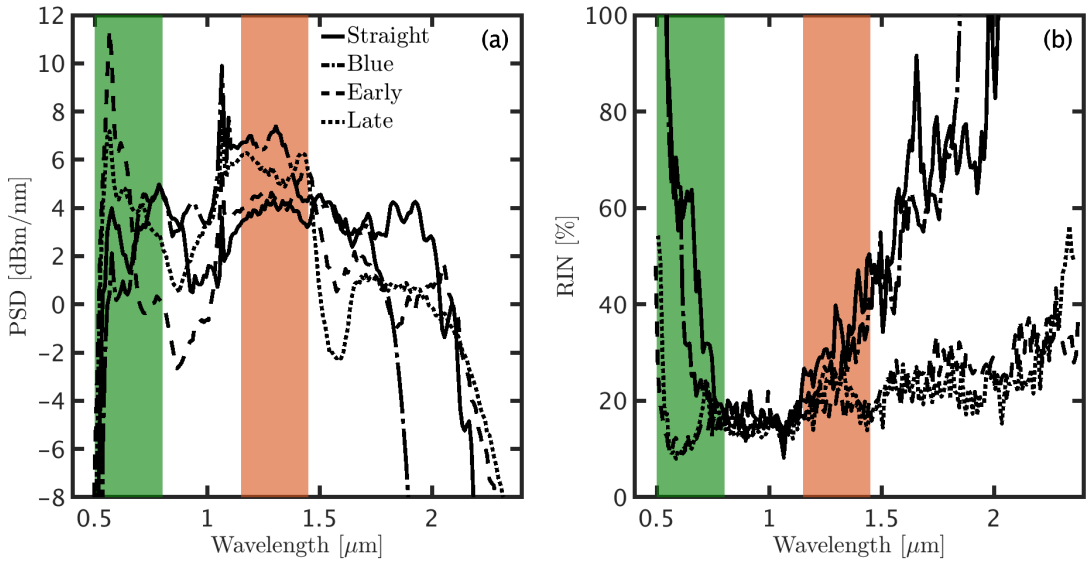

Figure 8.4: Power spectral density and relative intensity noise at the output for the four cases shown in Fig. 8.2. The green and red areas mark the spectral ranges that are of interest for visible and near infrared OCT.

the *Early* design (5.1 dBm/nm). In terms of noise, we now clearly see that both the *Early* and *Late* tapers are approximately the same in the whole region of interest. A recent US patent, [30], has experimentally shown the same trends as shown here by simulation.

In Fig. 8.5 (a+b) the integrated power and weigthed RIN in the bands of interest is shown as a function of propagation distance for the four cases described in Fig. 8.2 and 8.4. Since the *Straight*, *Blue* and *Late* cases have the exact same parameters in the first 1.1 m of fiber, the curves look the same in this region. Even with an average over $N_A = 50$ simulations we can see small variations. Looking at the noise, we observe the clear trend that propagation further is better, but the improvement becomes incremental after a short while in the taper waist. At the same time we observe that for the *Early* fiber there is a clear tradeoff between power and noise. For specific applications this would have to be taken into account. Interestingly, the RIN right at the start of the taper waist is the same within a few percent for the *Early* (dashed line, 0.6 m) and *Late* (dotted line, 1.6 m) designs. This will be revisited with the corresponding spectrograms.

We continue the investigation by looking into the influence of the degree of downtapering

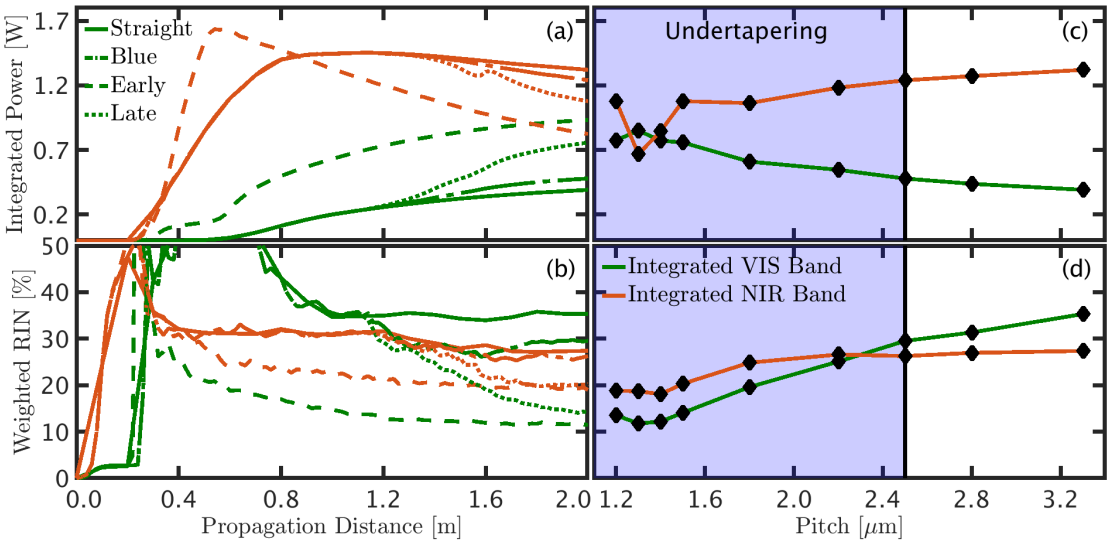

Figure 8.5: Power and weighted RIN for the two OCT bands shown in Fig. 8.4. The colors of the band match the colors of the graph, such that red is the NIR band, while green is the VIS band. (a+b) Shows the evolution as a function of propagation distance for the four cases in Fig. 8.2. (c+d) show how the average power and weighted RIN in the OCT bands change with different degree of tapering in the *Late* design. The initial pitch is 3.3 μm tapered to the pitch on the graph, with $L_s = 1.1$ m, $L_T = 0.5$ m and $L_W = 0.4$ m. Thus the diamond markers at 1.5 μm and 2.5 μm correspond to *Late* and *Blue* shown in the previous figures. The colored area marks the region of undertapering.

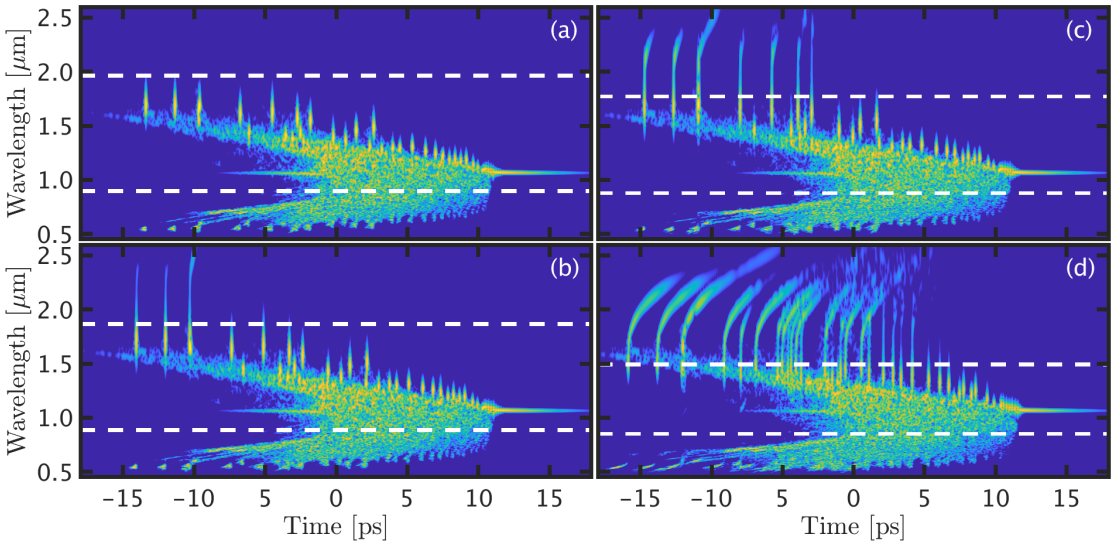

Figure 8.6: Spectrograms for a single shot at different propagation distances in the *Late* fiber design: (a) $z = 1.50\,\mathrm{m}$, (b) $z = 1.52\,\mathrm{m}$, (c) $z = 1.54\,\mathrm{m}$ and (d) $z = 1.6\,\mathrm{m}$. The spectrogram function used a 60 fs standard deviation, unnormalized gaussian envelope with an even 60 fs spacing in time. The white dashed lines denote zero dispersion wavelengths.

in the late taper design. This can be seen in Fig. 8.5 (c+d). The *Late* taper design was chosen as it seems to give the best results in terms of 1) low noise, 2) average power in the red and 3) most flat spectrum in both NIR and VIS ranges. For the VIS band, the noise improves almost linearly with tapering. For the NIR band, the noise improvements pick up as the second ZDW approaches the band. The power decreases only slightly in the NIR band, while it increases significantly in the VIS band. The sudden decrease at $1.3\,\mu$m corresponds to when the second ZDW enters the NIR band. This can be explained by the clear depletion of spectral power around the second ZDW, that was earlier discussed. Interestingly the RIN, which includes the spectral power, is largely unaffected by this depletion of spectral power. Taking both into account, there is a clear optimum at around $1.5\,\mu$m.

8.2 Spectogram Analysis

Let us now take a deeper look at why the noise is lowered in the tapers. In Fig. 8.6 we see spectrograms for a single shot simulation of the *Late* fiber design at different propagation distances, around the distance where the first solitons start to feel the second zero dispersion wavelength due to tapering. In (a), before the effects of the second ZDW start to show up we see the usual patterns expected from MI induced pulse breakup: First sidebands are created near the center of the pulse. Then fundamental solitons are formed, and

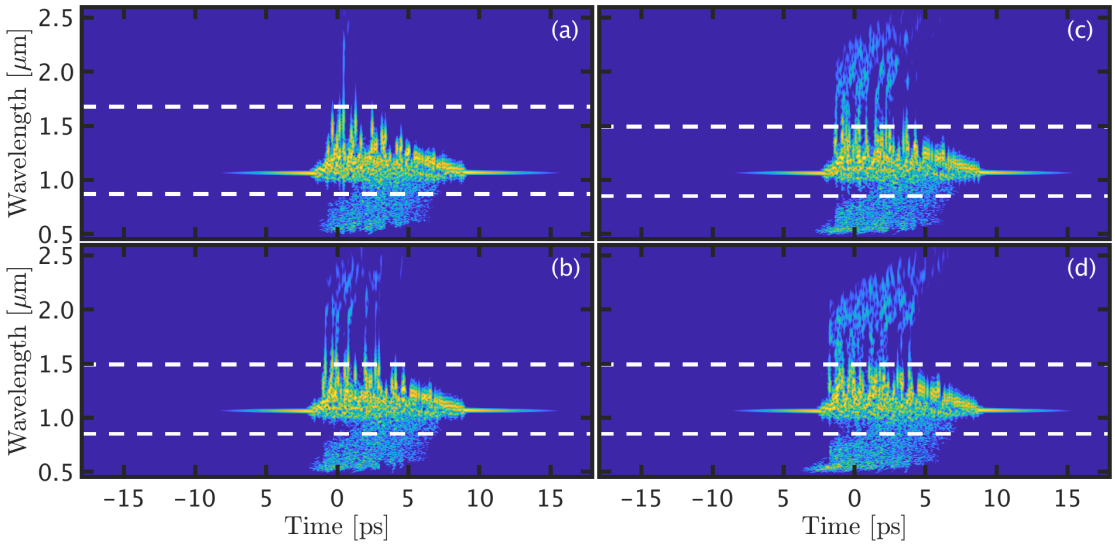

Figure 8.7: The figure showns spectrograms for a single shot at different propagation distances in the *Early* fiber design: (a) $z = 0.56\,\mathrm{m}$, (b) $z = 0.58\,\mathrm{m}$, (c) $z = 0.60\,\mathrm{m}$ and (d) $z = 0.62\,\mathrm{m}$. Spectrogram parameters are the same as those reported in Fig. 8.6.

eventually through collisions and energy transfer we are left with a few large redshifting solitons located at the red edge with matching dispersive waves at the blue edge [8]. In Fig. 8.6 (b+c), we see the effects of the second ZDW moving through the solitons spectrally. In established theory, when a soliton reaches the second ZDW through redshifting, it is recoiled and then spectrally broadens through phasematched energy transfer across the zero dispersion, [10, 12, 69]. It is the same we can see happening here. But due to the moving second ZDW, the soliton is moving ever closer to the second ZDW, which in turn moves the matching point in the normal dispersion on the other side. Normally the GV mismatch and non solitonic nature of the light generated would result in walk off and smearing, but since the second ZDW moves faster than the normal redshifting would, the soliton is extruded by the second ZDW before the generated light can either walk off or smear out. In the end, the extruded solitons have each increased their spectral content as seen in Fig. 8.6, and are now bending due to differences in group velocity at the different frequencies. The sum of light at any frequency is the sum of almost all the solitons. This is a major difference to the normal MI induced supercontinuum, where the light at the edge would come from a few solitons at most, [8, 13, 71]. We attribute the reduction in noise to this inherent averaging effect, as the exact spectral position of the individual solitons no longer matter.

In Fig. 8.7 we again look closer at what happens just as the solitons reach the second ZDW. This time for the *Early* fiber design. Clearly we are generating dispersive waves from individual solitons reaching the second ZDW, but it does not look as ordered as in the *Late* fiber. This is because we are much earlier in the fiber, and the soliton chaos has

yet to expulse a few large fundamental solitons. The dispersive waves are lost as fast as they are generated when the generating solitons collide and change their properties. So what we are seeing is the chaos inside the original pulse now mirrored across the second ZDW. Interestingly enough, this would have the same kind of averaging effect as the *Late* design, but with a larger number of soliton like pulses.

At the blue side of both *Early* and *Late* designs the same chaotic mirroring of dispersive waves across the ZDW as was discussed in the *Early* case is observed for both the *Early* and *Late* designs. This is in clear contrast to the *Blue* and *Straight* designs, where the blue edge from pulse to pulse is determined by the presence or absence of redshifted rogue wave solitons.

From Fig. 8.6 and 8.7 we can see that the position of the taper is extremely important for the physics, and even though the resulting output noise and spectral content might be almost the same, the fine structure is very different. Further improvements in noise might be observed if the initial straight fiber propagation length, L_S, is increased to enable more solitons to pass the final second ZDW before they are extruded during downtapering. The RIN at any wavelength is however never expected to be better than what is already observed at the pump for a straight fiber where the noise is determined by a sea of solitons. The best we can engineer with this method is a flat RIN with this value from edge to edge of the supercontinuum.

Reductions in the length of the downtaper section, L_T, has been superficially investigated without any notable changes. Thus the same good noise properties could ostensibly be obtained by forgoing the taper completely and splicing the initial straight fiber to the straight fiber at the waist. The losses due to mode mismatch would limit the applicability of this approach with respect to power.

The results presented here rely only on dispersion engineering and are independent of material, structure and wavelength. The results could thus be direcly applied to supercontinuum generation in other fibers where low noise is of interest, such as chalcogenide fibers in the mid infrared region [37,61]. With the advent of dispersion engineered specialty fibers [48], low noise supercontinuum generation covering the whole molecular fingerprint region should be possible.

8.3 Conclusion

It was found that the noise of a MI based supercontinuum can be significantly improved due to a larger degree of inherent averaging. This can come about as either soliton spectral extrusion when a second zero dispersion wavelength moves through several solitons during downtapering. Or as a sea of untrapped dispersive waves if the second zero dispersion wavelength is instead moved spectrally close to an active sea of solitons. The predicted

weighted RIN improvements are significant, from 35.3 % and 27.4 % to 14.0 % and 20.3 %, in the VIS and NIR spectral bands of interest for optical coherence tomography going from a straight fiber to the proposed *Late* taper design. The improvements are even more significant near the red spectral edge. Undertapering can be used to improve the quality of optical coherence tomography images, especially those in the visible spectrum or those close to the long edge of the transmission window of silica.

Chapter 9

Conclusion and Outlook

The work carried in this thesis was motivated by a desire for lower noise supercontinuum sources within the field of spectral domain optical coherence tomography. Some of the most promising approaches in the litterature are based on dispersion engineered photonic crystal fibers, fiber tapers and long pulses. To be able to model these, a rigorous derivating of the generalized nonlinear schrödinger equation starting from Maxwell's equations was carried out. During the derivation there was a focus on the approximations. The resulting equation included both multiple modes as well as adiabatic tapering and the results both confirmed, and were affirmed by, recent work done by others.

The generalized nonlinear schrödinger equation was implemented and solved numerically using GPU architecture. The implementation involve large number of FFT's on large data sets. It is therefore extremely well suited for the GPU architecture, as it takes advantage of both the faster shared memory and the increased parallel processing power. The increase in computation capability for current hardware make it feasible to do calculations that would before take prohibitively long, such as nanosecond pulses with fs resolution, multi pulse simulations or large ensemble calculations. Utilizing next generation tensor hardware and linked GPU clusters might provide even faster simulation capabilities in the future.

The relative intensity noise is the most important type of noise for spectral domain optical coherence tomography. Many methods exist to measure and quantify noise with varying bandwidth. Part of the work carried out was the foundation to unify three different methods which has been used a lot in literature. These are the oscilloscope pulse to pulse measurement, the electrical spectrum analyser measurement and the fast spectrometer measurement. As shown in this thesis, theoretically the methods are equivalent given the right equipment and use hereof. Examples were also given to illustrate the cases where wrong results are hidden. While not discussed in depth, a recent fourth method, the dispersive Fourier transform method, seems promising, especially considering that it can be used to obtain correlation diagrams. These can, as shown in the paper "Noise of supercontinuum sources in spectral domain optical coherence tomography", in turn be

used to accurately predict depth variation of the noise floor in spectral domain optical coherence tomography.

By using the methods developed, it was shown that the method of undertapering could be used to significantly reduce the noise at the edges of a supercontinuum generated by modulation instability. There were two ways this could come about. One was through soliton extrusion, where a second zero dispersion wavelength spectrally moved through solions and extruded them to become extremely wide spectrally. The other was by using the same second zero dispersion wavelength to prevent solitons from redshifting out of the initial sea of solitons. The noise improvement in both methods rely not on making the solitons more predictable from pulse to pulse, but instead rely on making sure that the light at any wavelength is the sum total of a great many solitons. The rogue waves are thus tamed through a higher degree of averaging.

Instead of improving existing commercial sources, such as the modulation instability driven supercontinuum sources, another method was investigated. This method involved the design of a flat, close to zero, normal dispersion fiber. The fiber is exceptionally efficient for self phase modulation, as the low absolute dispersion prevents the short pulses from broadening in time. The fiber was not directly suitable for pumping at 1064 nm. Instead a scheme based on initial soliton fission followed by soliton self frequency shift and soliton self compression was investigated. The method was proven to be viable and even an improvement on existing methods. However the noise improvement were not as good as expected, due to interference fringes between the generated solitons. Pump noise was found to play a large role in low noise supercontinuum. This is something that has been overlooked in the past when investigating the more noisy modulation instability based supercontinuum generation for which it does not matter.

Appendix A

Publication List

The PhD studies have resulted in the publications listed in this appendix.

A.1 Journal Publications

1. I. B. Gonzalo, R. D. Engelsholm, M. P. Sorensen and Ole Bang, "Polarization noise places severe constraints on coherence of all-normal supercontinuum generation", Sci. Rep. **8**, 6579 (2018).

2. C. R. Petersen, R. D. Engelsholm, C. Markos, L. Brilland, C. Caillaud, J. Trolès and Ole Bang, "Increased mid-infrared supercontinuum bandwidth and average power by tapering large-mode-area chalcogenide photonic crystal fibers", Optics Express **25**, 15336-15348 (2017).

A.2 Journal Publications in Review

1. R. D. Engelsholm and Ole Bang, "Supercontinuum Noise Reduction by Fiber Undertapering", Optics Express **x**, x (xxxx).

2. S. D. Rao, R. D. Engelsholm, I. B. Gonzalo, B. Zhou, P. Bowen, P. M. Moselund, O. Bang and M. Bache, "Ultra-low Noise Supercontinuum Generation with Flat Near-zero Normal Dispersion Fiber", Optics Letters **x**, x (xxxx).

3. M. Jensen, I. B. Gonzalo, R. D. Engelsholm, M. Maria, N. M. Israelsen, A. Podoleanu and O. Bang, "Noise of supercontinuum sources in spectral domain optical coherence tomography", J. Opt. Soc. Am. B **x**, x (xxxx).

A.3 Conference Contributions

1. M. Maria, I. B. Gonzalo, M. Bondu, R. D. Engelsholm, T. Feuchter, P. M. Moselund, L. Leick, O. Bang and A. Podoleanu, "A comparative study of nosie in supercontinuum light sources for ultra-high resolution optical coherence tomography", Design and Quality for Biomedical Technologies X (2017).

2. S. D. Rao, R. D. Engelsholm, I. B. Gonzalo, B. Zhou, P. Bowen, P. M. Moselund, M. Bache and O. Bang, "Ultra-low Noise Supercontinuum Generation with Flat Near-zero All Normal Dipsersion Pure Silica Fiber at GHz Repetition Rate", Nonlinear Photonics (2018).

3. I. B. Gonzalo, R. D. Engelsholm and O. Bang, "Noise study of all-normal dispersion supercontinuum sources for potential application in optical coherence tomography", 2nd Canterbury Conference on OCT (2018).

4. I. B. Gonzalo, M. Maria, R. D. Engelsholm, T. Feuchter, L. Leick, P. M. Moselund, A. Podoleanu and O. Bang, "Ultra-low noise supercontinuum source for ultra-high resolution optical coherence tomography at 1300 nm", Design and Quality for Biomedical Technologies XI (2018).

5. C. R. Petersen, R. D. Engelsholm, C. Markos, L. Brilland, J. Troles and O. Bang, "Efficient mid-infrared supercontinuum generation in tapered large mode area chalcogenide photonic crystal fibers", CLEO: Science and Innovations (2017).

6. C. Chin, R. D. Engelsholm, P. M. Moselund,T. Feuchter, L. Leick, A. Podoleanu and O. Bang, "Polarization extinction ratio and polarization dependent intensity noise in long-pulse supercontinuum generation", Real-time Measurements, Rogue Phenomena, and Single-Shot Applications II. Vol. 10089. International Society for Optics and Photonics, 2017.

Appendix B

List of approximations used in deriving the GNLSE

The following approximations and assumptions were made in deriving and implementing the tapered multimode version of the GNLSE:

- It is assumed that the nonlinear polarization can be accurately described by a power expansion, where the higher order terms have been truncated.
- It is assumed that each individual mode satisfies Maxwell's equations when the nonlinear term is neglected. This is equivalent to assuming the induced nonlinear polarization is a small perturbation to the electric field, that does not change the modes.
- It is assumed that the calculated overlap integrals are correct, even when they are truncated due to a finite transverse grid used in the finite element method (or other methods).
- It is assumed that the cross terms due to tapering can be neglected due to rapidly changing phasematching conditions that will never allow the fields the time they need to build up.
- It is assumed that the second order induced polarization is zero, by limiting the derivation to isotropic (silica glass) fibers, which due to their inherent random crystal and molecular orientation are spatially symmetric. This only works if the fibers are not treated to break the symmetry by for instance electric fields. Furthermore, by working with isotropic materials, the remaining third order tensor will be reduced enormously in complexity due to symmetry considerations.
- It is assumed that the transverse functions can be evaluated at ω_0 irrespective of the actual frequencies involved when mode profile dispersion is disregarded. This approximation should hold as long as the involved frequencies at any time are not

too far apart, which for practical purposes translates to supercontinua where the generated bandwidth at any point is much smaller than the carrier frequency.

- It is assumed in the implementation that third harmonic generation and double rotating Raman scattering can both be neglected.
- It is assumed in the implementation that the overlap integrals are independant of the position of the complex conjugate. This is valid for weakly confined light, where the transverse modes are approximately real.

Bibliography

[1] Y. Ould Agha, F. Zolla, A. Nicolet, and S. Guenneau. On the use of PML for the computation of leaky modes: an application to microstructured optical fibres. *COMPEL*, 27(1):95–109, 2008.

[2] Govind Agrawal. *Nonlinear Fiber Optics*. Elsevier, fifth edition, 2013.

[3] T. A. Birks, W. J. Wadsworth, and P. St. J. Russell. Supercontinuum generation in tapered fibers. *Optics Letters*, 25(19):1415, 2000.

[4] Keith J. Blow and David Wood. Theoretical Description of Transient Stimulated Raman Scattering in Optical Fibers. *Journal of Quantum Electronics*, 25(12):2665–2672, 1989.

[5] William J Brown, Sanghoon Kim, and Adam Wax. Noise characterization of supercontinuum sources for low-coherence interferometry applications. *JOSA A*, 31(12):2703–2710, 2014.

[6] Wolfgang Drexler and James G Fujimoto. *Optical coherence tomography: technology and applications*. Springer Science & Business Media, 2008.

[7] J. M. Dudley, G. Genty, F. Dias, B. Kibler, and N. Akhmediev. Modulation instability, Akhmediev Breathers and continuous wave supercontinuum generation. *Optics Express*, 17(24):21497, 2009.

[8] John M. Dudley, Goëry Genty, and Stéphane Coen. Supercontinuum generation in photonic crystal fiber. *Reviews of Modern Physics*, 78(4):1135–1184, 2006.

[9] Miro Erkintalo, Kamal Hammani, Bertrand Kibler, Christophe Finot, Nail Akhmediev, John M Dudley, and Goëry Genty. Higher-order modulation instability in nonlinear fiber optics. *Physical review letters*, 107(25):253901, 2011.

[10] Peter Falk, Michael H. Frosz, and Ole Bang. Supercontinuum generation in a photonic crystal fiber with two zero-dispersion wavelengths tapered to normal dispersion at all wavelengths. *Optics Express*, 13(19):7535, 2005.

[11] Christophe Finot, Bertrand Kibler, Lionel Provost, and Stefan Wabnitz. Beneficial impact of wave-breaking for coherent continuum formation in normally dispersive nonlinear fibers. *J. Opt. Soc. Am. B*, 25(11):1938–1948, 2008.

[12] Michael H. Frosz, Peter Falk, and Ole Bang. The role of the second zero-dispersion wavelength in generation of supercontinua and bright-bright soliton-pairs across the zero-dispersion wavelength. *Optics Express*, 13(16):6181, 2005.

[13] G. Genty, C. M. de Sterke, O. Bang, F. Dias, N. Akhmediev, and J. M. Dudley. Collisions and turbulence in optical rogue wave formation. *Physics Letters A*, 374:989–996, 2010.

[14] Goëry Genty, Stéphane Coen, and John M Dudley. Fiber supercontinuum sources. *J. Opt. soc. Am. B*, 24(8):1771–1785, 2007.

[15] K Goda and B Jalali. Dispersive fourier transformation for fast continuous single-shot measurements. *Nature Photonics*, 7(2):102, 2013.

[16] T. Godin, B. Wetzel, T. Sylvestre, L. Larger, A. Kudlinski, A. Mussot, A. Ben Salem, M. Zghal, G. Genty, F. Dias, and J. M. Dudley. Real time noise and wavelength correlations in octave-spanning supercontinuum generation. *Optics Express*, 21(15):18452, 2013.

[17] Ivan Bravo Gonzalo, Rasmus Dybbro Engelsholm, Mads Peter Sorensen, and Ole Bang. Polarization noise places severe constraints on coherence of all- normal dispersion femtosecond supercontinuum generation. *Scientific Reports*, 8(6579), 2018.

[18] A. V. Gorbach and D. V. Skryabin. Light trapping in gravity-like potentials and expansion of supercontinuum spectra in photonic crystal fibres. *Nature Photonics*, 1:653–657, 2007.

[19] Kamal Hammani, Benjamin Wetzel, Bertrand Kibler, Julien Fatome, Christophe Finot, Guy Millot, Nail Akhmediev, and John M Dudley. Spectral dynamics of modulation instability described using akhmediev breather theory. *Optics letters*, 36(11):2140–2142, 2011.

[20] Danielle J. Harper, Marco Augustin, Antonia Lichtenegger, Pablo Eugui, Carlos Reyes, Martin Glosmann, Christoph K. Hitzenberger, and Bernhard Baumann. White light polarization sensitive optical coherence tomography for sub-micron axial resolution and spectroscopic contrast in the murine retina. *Biomedical Optics Express*, 9(5):2115–2129, 2018.

[21] Alexander Hartung, Alexander M. Heidt, and Hartmut Bartelt. Design of all-normal dispersion microstructured optical fibers for pulse-preserving supercontinuum generation. *Optics Express*, 19(8):7742–7749, 2011.

[22] Christopher Robin Head, Ho-Yin Chan, James S. Feehan, David P. Shepherd, Shaif-ul Alam, Anne C. Tropper, Jonathan H. V. Price, and Keith G. Wilcox. Supercontinuum Generation with GHz Repetition Rate Femtosecond-Pulse Fiber-Amplified VECSELs. *IEEE Photonics Technology Letters*, 25(5):464–467, 2013.

[23] Alexander M Heidt. Efficient adaptive step size method for the simulation of supercontinuum generation in optical fibers. *Journal of Lightwave Technology*, 27(18):3984–3991, 2009.

[24] Alexander M. Heidt. Pulse preserving flat-top supercontinuum generation in all-normal dispersion photonic crystal fibers. *J. Opt. soc. Am. B*, 27(3):550–559, 2010.

[25] Alexander M. Heidt, James S. Feehan, Jonathan H. V. Price, and Thomas Feurer. Limits of coherent supercontinuum generation in normal dispersion fibers. *Journal of the Optical Society of America B*, 34(4):764–775, 2017.

[26] RW Hellwarth. Third-order optical susceptibilities of liquids and solids. *Progress in Quantum Electronics*, 5:1–68, 1977.

[27] Johan Hult. A Fourth-Order Runge-Kutta in the Interaction Picture Method for Simulating Supercontinuum Generation in Optical Fibers. *Journal of Lightwave Technology*, 25(12):3770–3775, 2007.

[28] Niels M Israelsen, Michael Maria, Thomas Feuchter, Adrian Podoleanu, and Ole Bang. Non-destructive testing of layer-to-layer fusion of a 3d print using ultrahigh resolution optical coherence tomography. In *Optical Measurement Systems for Industrial Inspection X*, volume 10329, page 103290I. International Society for Optics and Photonics, 2017.

[29] Niels Moeller Israelsen, Michael Maria, Mette Mogensen, Sophie Bojesen, Mikkel Jensen, Merete Hædersdal, Adrian Podoleanu, and Ole Bang. The value of ultrahigh resolution OCT in dermatology - delineating the dermo-epidermal junction, capillaries in the dermal papillae and vellus hairs. *Biomedical Optics Express*, 9(5):2240–2265, 2018.

[30] Jeppe Johansen, Ole Bang, Casper Larsen, Thomas Feuchter, Thomas Vestergaard Andersen, and Carsten L. Thomsen. Microstructured optical fiber, supercontinuum light source comprising microstructured optical fiber and use of such light source, 2013. US Patent 9841557B2.

[31] Nayara Jornod, Kutan Gürel, Valentin J Wittwer, Pierre Brochard, Sargis Hakobyan, Stéphane Schilt, Dominik Waldburger, Ursula Keller, and Thomas Südmeyer. Carrier-envelope offset frequency stabilization of an ultrafast semiconductor laser. In *Vertical External Cavity Surface Emitting Lasers (VECSELs) VIII*, volume 10515, page 105150K. International Society for Optics and Photonics, 2018.

[32] Bertrand Kibler, Julien Fatome, Christophe Finot, Guy Millot, Frédéric Dias, Goëry Genty, Nail Akhmediev, and John M Dudley. The peregrine soliton in nonlinear fibre optics. *Nature Physics*, 6(10):790, 2010.

[33] M Kolesik and J.V. Moloney. Nonlinear optical pulse propagation simulation: From maxwells to unidirectional equations. *Physical Review E*, 70(3):036604, 2004.

[34] M Kolesik, E. M. Wright, and J. V. Moloney. Simulation of femtosecond pulse propagation in sub-micron diamter tapered fibers. *Applied Physics B*, 79(3):293–300, 2004.

[35] Moloney Kolesik, JV Moloney, and M Mlejnek. Unidirectional optical pulse propagation equation. *Physical review letters*, 89(28):283902, 2002.

[36] Daniel M Koller, Günther Hannesschläger, Michael Leitner, and JG Khinast. Non-destructive analysis of tablet coatings with optical coherence tomography. *European journal of pharmaceutical sciences*, 44(1-2):142–148, 2011.

[37] Irnis Kubat, Christian S Agger, Uffe Møller, Angela B Seddon, Zhuoqi Tang, Slawomir Sujecki, Trevor M. Benson, David Furniss, Samir Lamrini, Karsten Scholle, Peter Fuhrberg, Bruce Napier, Mark Farries, Jon Ward, Peter M Moselund, and Ole Bang. Mid infrared supercontinuum generation to 12.5 μm in large NA chalcogenide step-index fibres pumped at 4.5 μm. *Optics express*, 22(16):19169–19182, 2014.

[38] A. Kudlinski, B. Barviau, A. Leray, C. Spriet, and A. Mussot. Control of pulse-to-pulse fluctuations in visible supercontinuum. *Optics Express*, 18(26):27445–27454, 2010.

[39] Jesper Laegsgaard. Mode profile dispersion in the generalised nonlinear Schrödinger equation. *Optics Express*, 15(24):16110–16123, 2007.

[40] Jesper Laegsgaard. Modeling of nonlinear propagation in fiber tapers. *Journal of the Optical Society of America B*, 29(11):3183–3191, 2012.

[41] C. Lafargue, J. Bolger, G. Genty, F. Dias, J. M. Dudley, and B. J. Eggleton. Direct detection of optical rogue wave energy statistics in supercontinuum generation. *Electronics Letters*, 45(4):217–219, 2009.

[42] Casper Larsen. *Gain-switched All-fiber Lasers and Quasi-continuous Wave Supercontinuum Generation*. PhD thesis, 2013.

[43] Andrei V Lavrinenko, Jesper Lægsgaard, Niels Gregersen, Frank Schmidt, and Thomas Søndergaard. *Numerical methods in photonics*. CRC Press, 2014.

[44] Q Lin and Govind P Agrawal. Raman response function for silica fibers. *Optics letters*, 31(21):3086–3088, 2006.

[45] Yuan Liu, Youbo Zhao, Jens Lyngsø, Sixian You, William L. Wilson, Haohua Tu, and Stephen A. Boppart. Suppressing Short-Term Polarization Noise and Related Spectral Decoherence in All-Normal Dispersion Fiber Supercontinuum Generation. *Journal of Lightwave Technology*, 33(9):1814–1820, 2015.

[46] P. V. Mamyshev and S. V. Chernikov. Ultrashort-pulse propagation in optical fibers. *Optics Letters*, 15(19):1076–1078, 1990.

[47] Michael Maria, Ivan Bravo Gonzalo, Thomas Feuchter, Mark Denninger, Peter M. Moselund, Lasse Leick, Ole Bang, and Adrian Podoleanu. Q-switch-pumped super-

continuum for ultra-high resolution optical coherence tomography. *Optics Letters*, 42(22):4744–4747, 2017.

[48] Christos Markos, John C. Travers, Amir Abdolvand, Benjamin J. Eggleton, and Ole Bang. Hybrid photonic-crystal fiber. *Reviews of Modern Physics*, 89(4), 2017.

[49] David Milam. Review and assessment of measured values of the nonlinear refractive-index coeffcient of fused silica. *Applied Optics*, 37(3):546–550, 1998.

[50] L. F. Mollenauer, R. H. Stolen, and J. P. Gordon. Experimental Observation of Picosecond Pulse Narrowing and Solitons in Optical Fibers. *Phys. Rev. Lett.*, 45(13):1095–1098, 1980.

[51] U. Møller, S. T. Sørensen, C. Jakobsen, J. Johansen, P. M. Moselund, C. L. Thomsen, and O. Bang. Power dependence of supercontinuum noise in uniform and tapered PCFs. *Optics Express*, 20(3):2851–2857, 2012.

[52] Uffe Moller and Ole Bang. Intensity noise in normal-pumped picosecond supercontinuum generation, where higher-order Raman lines cross into anomalous dispersion regime. *Electronics Letters*, 49(1), 2013.

[53] Uffe Møller, Simon T. Sørensen, Casper Larsen, Peter M. Moselund, Christian Jakobsen, Jeppe Johansen, Carsten L. Thomsen, and Ole Bang. Optimum PCF tapers for blue-enhanced supercontinuum sources. *Optical Fiber Technology*, 18(5):304–314, 2012.

[54] Niels Asger Mortensen. Effective area of photonic crystal fibers. *Optics Express*, 10(7):341–348, 2002.

[55] Niels Asger Mortensen, Jacob Riis Folkenberg, Peter M. W. Skovgaard, and Jes Broeng. Numerical aperture of single-mode photonic crystal fibers. *IEEE Photonics Technology Letters*, 14(8):1094–1096, 2002.

[56] Peter M. Moselund. *Long-pulse Supercontinuum Light Sources*. PhD thesis, Technical University of Denmark, 2009.

[57] Norihiko Nishizawa and Jun Takayanagi. Octave spanning high-quality supercontinuum generation in all-fiber system. *J. Opt. Soc. Am. B*, 24(8):1786–1792, 2007.

[58] Katsunari Okamoto. *Fundamentals of optical waveguides*. Academic press, 2006.

[59] Christian Rosenberg Pedersen, Uffe Møller, Irnis Kubat, Binbin Zhou, Sune Dupont, Jacob Ramsay, Trevor Benson, Slawomir Sujecki, Nabil Abdel-Moneim, zhuoqi Tang, David Furniss, Angela Seddon, and Ole Bang. Mid-infrared supercontinuum covering the $1.4-13.3\,\mu$m molecular fingerprint region using ultra-high NA chalcogenide step-index fibre. *Nature Photonics Letters*, 8(11):830–835, 2014.

[60] Frank L Pedrotti, Leno M Pedrotti, and Leno S Pedrotti. *Introduction to optics*. Cambridge University Press, 2017.

[61] Christian Rosenberg Petersen, Rasmus Dybbro Engelsholm, Christos Markos, Laurent Brilland, Celine Caillaud, Johan Troles, and Ole Bang. Increased mid-infrared supercontinuum bandwidth and average power by tapering large-mode-area chalcogenide photonic crystal fibers. *Optics Express*, 25(13), 2017.

[62] Francesco Poletti and Peter Horak. Description of ultrashort pulse propagation in multimode optical fibers. *Journal of the Optical Society of America B*, 25(10):1645–1654, 2008.

[63] Benjamin Potsaid, Iwona Gorczynska, Vivek J Srinivasan, Yueli Chen, James Jiang, Alex Cable, and James G Fujimoto. Ultrahigh speed spectral/fourier domain oct ophthalmic imaging at 70,000 to 312,500 axial scans per second. *Optics express*, 16(19):15149–15169, 2008.

[64] A. A. Rieznik, A. M. Heidt, P. G. König, V. A. Bettachini, and D. F. Grosz. Optimum Integration Procedures for Supercontinuum Simulation. *IEEE Photonics Journal*, 4(2):552–560, 2012.

[65] Robert Rockmore, Caleb W Baker, Alexandre Laurain, Tsung-Han Wu, R Jason Jones, and Jerome V Moloney. Supercontinuum generation and beatnote detection using ultrafast vecsel seed oscillators. In *Vertical External Cavity Surface Emitting Lasers (VECSELs) VIII*, volume 10515, page 105150M. International Society for Optics and Photonics, 2018.

[66] Bahaa E.A. Saleh and Malvin Carl Teich. *Fundamentals of photonics*, volume 22. Wiley New York, 1991.

[67] Ryan P Scott, Carsten Langrock, and Brian H Kolner. High-dynamic-range laser amplitude and phase noise measurement techniques. *IEEE Journal of selected topics in quantum electronics*, 7(4):641–655, 2001.

[68] Xiao Shu, Lisa Beckmann, and Hao F. Zhang. Visible-light optical coherence tomography: a review. *Journal of Biomedical Optics*, 22(12), 2017.

[69] D. V. Skryabin, F. Luan, J. C. Knight, and P. St J. Russell. Soliton self-frequency shift cancellation in photonic crystal fibers. *Science*, 301(5640):1705–1708, 2003.

[70] D. R. Solli, C. Ropers, and B. Jalali. Active control of rogue waves for stimulated supercontinuum generation. *Physical Review Letters*, 101(23):18–21, 2008.

[71] D. R. Solli, C. Ropers, P. Koonath, and B. Jalali. Optical rogue waves. *Nature*, 450:1054–1057, 2007.

[72] S. T. Sørensen, U. Møller, C. Larsen, P. M. Moselund, C. Jakobsen, J. Johansen, T. V. Andersen, C. L. Thomsen, and O. Bang. Deep-blue supercontinnum sources with optimum taper profiles - verification of GAM. *Optics Express*, 20(10):10635–10645, 2012.

[73] Simon Toft Sørensen and Ole Bang. Deep-blue supercontinuum light sources based on tapered photonic crystal bres. 2013.

[74] Simon Toft Sorensen, Ole Bang, Benjamin Wetzel, and John M. Dudley. Describing supercontinuum noise and rogue wave statistics using higher-order moments. *Optics Communications*, 285:2451–2455, 2012.

[75] Roger H Stolen, James P Gordon, WJ Tomlinson, and Hermann A Haus. Raman response function of silica-core fibers. *JOSA B*, 6(6):1159–1166, 1989.

[76] Igor A Sukhoivanov, Sergii O Iakushev, Oleksiy V Shulika, Jose Amparao Andrade-Lucio, Antonio Díez, and Miguel Andrés. Supercontinuum generation at 800 nm in all-normal dispersion photonic crystal fiber. *Optics express*, 22(24):30234–30250, 2014.

[77] Ou Tan, Vikas Chopra, Ake Tzu-Hui Lu, Joel S Schuman, Hiroshi Ishikawa, Gadi Wollstein, Rohit Varma, and David Huang. Detection of macular ganglion cell loss in glaucoma by fourier-domain optical coherence tomography. *Ophthalmology*, 116(12):2305–2314, 2009.

[78] J. C. Travers and J. R. Taylor. Soliton trapping of dispersive waves in tapered optical fibers. *Optics Letters*, 34(2):115–117, 2009.

[79] Haohua Tu, Yuan Liu, Jesper Lægsgaard, Utkarsh Sharma, Martin Siegel, Daniel Kopf, and Stephen A Boppart. Scalar generalized nonlinear schrödinger equation-quantified continuum generation in an all-normal dispersion photonic crystal fiber for broadband coherent optical sources. *Optics express*, 18(26):27872–27884, 2010.

[80] O. Vanvincq, J. C. Travers, and A. Kudlinski. Conservation of the photon number in the generalized nonlinear Schrödinger equation in axially varying optical fibers. *Physical Review A*, 84, 2011.

[81] Zhao Wang, Benjamin Potsaid, Long Chen, Chris Doerr, Hsiang-Chieh Lee, Torben Nielson, Vijaysekhar Jayaraman, Alex E Cable, Eric Swanson, and James G Fujimoto. Cubic meter volume optical coherence tomography. *Optica*, 3(12):1496–1503, 2016.

[82] Julia Welzel. Optical coherence tomography in dermatology: a review. *Skin Research and Technology: Review article*, 7(1):1–9, 2001.

[83] B. Wetzel, A. Stefani, L. Larger, P. A. Lacourt, J. M. Merolla, T. Sylvestre, A. Kudlinski, A. Mussot, G. Genty, F. Dias, and J. M. Dudley. Real-time full bandwidth measurement of spectral noise in supercontinuum generation. *Scientific Reports*, 2(882), 2012.

[84] Karin Wiesauer, Michael Pircher, Erich Götzinger, Siegfried Bauer, Rainer Engelke, Gisela Ahrens, Gabi Grützner, Christoph K Hitzenberger, and David Stifter. En-face scanning optical coherence tomography with ultra-high resolution for material investigation. *Optics Express*, 13(3):1015–1024, 2005.

[85] Ji Yi, Wenzhong Liu, Siyu Chen, Vadim Backman, Nader Sheibani, Christine M. Sorenson, Amani A. Fawzi, Robert A. Linsenmeier, and Hao F. Zhang. Visible light

optical coherence tomography measures retinal oxygen metabolic response to systemic oxygenation. *Light: Science & Applications*, 4(9):e334, 2015.

[86] Zhaoming Zhu and Thomas G. Brown. Polarization properties of supercontinuum spectra generated in bifringent photonic crystal fibers. *J. Opt. Soc. Am. B*, 21(2):249–257, 2004.

[87] Yi Zou, Swapnajit Chakravarty, Chi-Jui Chung, Xiaochuan Xu, and Ray T. Chen. Mid-infrared silicon photonic waveguides and devices. *Photonics Research*, 6(4):254–276, 2018.